



**HAL**  
open science

## Emergence et phénomènes collectifs dans des suspensions chirales de micronageurs

Sotiris Samatas

► **To cite this version:**

Sotiris Samatas. Emergence et phénomènes collectifs dans des suspensions chirales de micronageurs. Physics [physics]. Université de Bordeaux, 2023. English. NNT : 2023BORD0453 . tel-04633224

**HAL Id: tel-04633224**

**<https://theses.hal.science/tel-04633224>**

Submitted on 3 Jul 2024

**HAL** is a multi-disciplinary open access archive for the deposit and dissemination of scientific research documents, whether they are published or not. The documents may come from teaching and research institutions in France or abroad, or from public or private research centers.

L'archive ouverte pluridisciplinaire **HAL**, est destinée au dépôt et à la diffusion de documents scientifiques de niveau recherche, publiés ou non, émanant des établissements d'enseignement et de recherche français ou étrangers, des laboratoires publics ou privés.

THÈSE PRÉSENTÉE  
POUR OBTENIR LE GRADE DE

**DOCTEUR DE  
L' UNIVERSITÉ DE BORDEAUX**

ÉCOLE DOCTORALE DES SCIENCES PHYSIQUES ET DE L' INGÉNIEUR  
SPÉCIALITÉ : LASERS, MATIÈRE ET NANOSCIENCES

par Sotiris Samatas

**Emergence and Collective Phenomena in  
Chiral Microswimmer Suspensions**

Sous la direction de : Juho Lintuvuori  
Co-directeur : Alois Würger

Soutenue le 15/12/2023

Membres du jury :

M. Hamid Kellay  
Mme Valeriani Chantal  
M. Rik Wensik  
M. Simon Villain-Gillot

LOMA, Université de Bordeaux.  
Universidad Complutense de Madrid  
CNRS, LPS, Université Paris-Saclay  
LOMA, Université de Bordeaux.

Président  
Rapporteuse  
Rapporteur  
Examineur

Membres invités :

M. Juho Lintuvuori  
M. Alois Würger

CNRS, LOMA  
LOMA, Université de Bordeaux

Superviseur  
Co-superviseur









# Résumé

Nous étudions les phénomènes collectifs dans les suspensions en bulk de micronageurs sphériques à trajectoires chirales en utilisant des simulations numériques à grande échelle. Le modèle est générique. Il correspond à la solution d'ordre le plus bas d'un modèle général d'autopropulsion à nombres de Reynolds faibles, constitué d'un dipôle source rotatif non axisymétrique. Nous montrons que les nageurs purement circulaires et hélicoïdaux peuvent spontanément synchroniser leur rotation. L'état synchronisé correspond à un alignement des vitesses avec un ordre d'orientation élevé dans les directions polaire et azimutale. Pour illustrer la robustesse de l'état synchronisé, nous considérons un mélange racémique de nageurs hélicoïdaux où la synchronisation intra-espèce est observée tandis que le système reste comme un fluide spatialement uniforme. Nos résultats démontrent la synchronisation hydrodynamique en tant que phénomène collectif naturel pour les micronageurs à trajectoires chirales. Une fois la synchronisation atteinte, nous montrons que le système peut manifester des comportements collectifs post-synchronisation complexes impliquant séparation de phase et propagation d'ondes d'ordre polaire local. Nos observations fournissent une base convaincante pour les recherches futures sur les flux collectifs émergents et la diffusivité augmentée induite à cause de l'activité dans les suspensions de micronageurs chiraux.

**Mots-clès :** Micronageurs, Synchronisation, Chiral, Flux à faible nombre de Reynolds, Emergence, Phénomènes collectifs





# Abstract

We study collective phenomena in bulk suspensions of spherical microswimmers with chiral trajectories using large scale numerics. The model is generic. It corresponds to the lowest order solution of a general model for self-propulsion at low Reynolds numbers, consisting of a nonaxisymmetric rotating source dipole. We show that both purely circular and helical swimmers can spontaneously synchronize their rotation. The synchronized state corresponds to velocity alignment with high orientational order in both the polar and azimuthal directions. To exemplify the robustness of the synchronised state, we consider a racemic mixture of helical swimmers where intraspecies synchronization is observed while the system remains as a spatially uniform fluid. Our results demonstrate hydrodynamic synchronization as a natural collective phenomenon for microswimmers with chiral trajectories. Once synchronisation is attained, we show that the system can manifest complex post-synchronisation collective behaviour involving phase separation and the propagation of waves with local polar order. Our observations provide a compelling basis for future research on emerging collective flows and activity-driven enhanced diffusivity in chiral microswimmer suspensions.

**Key words:** Microswimmers, Synchronisation, Chiral, Low-Reynolds-number flows, Emergence, Collective phenomena



# Contents

<b>Résumé</b> . . . . .	<b>i</b>
<b>Abstract</b> . . . . .	<b>iii</b>
<b>List of Figures</b> . . . . .	<b>vii</b>
<b>Introduction</b> . . . . .	<b>1</b>
<b>1 Model for rotational squirmers</b> . . . . .	<b>5</b>
1.1 The Stokes equations . . . . .	5
1.2 The standard squirmer model . . . . .	6
1.3 Reciprocal theorem for the standard squirmer model . . . . .	7
1.4 Squirmer model for circular and helical swimming . . . . .	9
1.5 Choosing the parameters for chiral swimmers . . . . .	11
1.6 Simulation details . . . . .	13
<b>2 Circular swimmers</b> . . . . .	<b>15</b>
2.1 Synchronisation of circular microswimmers . . . . .	15
2.2 Circular microswimmer diffusive dynamics . . . . .	20
2.3 Random close packing argument for the onset of synchronisation in circular swimmer suspensions . . . . .	23
2.4 De-synchronisation of circular microswimmers . . . . .	24
<b>3 Helical swimmers</b> . . . . .	<b>27</b>
3.1 Synchronisation of helical microswimmers . . . . .	27
3.2 Racemic mixture of helical microswimmers . . . . .	33
3.3 Comparison to racemic mixture of circular microswimmers . . . . .	38
<b>4 Post-synchronisation collective phenomena</b> . . . . .	<b>41</b>

4.1	Post-synchronisation phase separation in circular microswimmer suspensions . . . . .	41
4.2	Finite Re analysis and size effects . . . . .	42
4.3	Large-scale simulations of circular microswimmers . . . . .	47
4.4	Case study of post-synchronisation phase separation . . . . .	50
4.4.A	Structure analysis of the clustered phase . . . . .	50
4.4.B	Particle velocity analysis and enhanced diffusivity . . . . .	52
4.4.C	Microswimmer dynamics . . . . .	54
4.5	Formation of travelling bands with local polarisation . . . . .	61
4.6	Summary of the observations . . . . .	63
<b>Conclusion . . . . .</b>		<b>65</b>
<b>APPENDIX . . . . .</b>		<b>67</b>
<b>A. Slip velocity profiles of neutral squirmers, shakers, pushers and pullers . . . . .</b>		<b>69</b>
A.1	$n = 1$ . . . . .	70
A.2	$n = 2$ . . . . .	71
A.3	Forming Pullers and Pushers: . . . . .	74
<b>B. Translational and Angular Velocity of Self-Propelling Particles . . . . .</b>		<b>79</b>
B.1	Classic squirmer model: $\mathbf{u}' = \sin\theta(b_1 + b_2 \cos\theta) \hat{\mathbf{e}}_\theta$ . . . . .	80
B.2	$\mathbf{u}' = b_2 \cos\phi \hat{\mathbf{e}}_\phi$ . . . . .	81
B.3	$\mathbf{u}' = \sin\theta b_2 \cos\phi \hat{\mathbf{e}}_\phi$ . . . . .	81
B.4	Our “general” rotor model: $\mathbf{u}' = \sin\theta(b_1 + b_2 \cos(n\phi)) \hat{\mathbf{e}}_\phi$ . . . . .	82
<b>C. Publication . . . . .</b>		<b>85</b>
	Hydrodynamic synchronisation of chiral microswimmers . . . . .	85
<b>Bibliography . . . . .</b>		<b>93</b>

# List of Figures

I.1	Examples of biological and artificial microswimmers . . . . .	1
1.1	The standard squirmer model . . . . .	6
1.2	Self-propulsion of the neutral squirmer . . . . .	8
1.3	Building circular swimmers . . . . .	11
1.4	Building helical swimmers . . . . .	12
1.5	Rotational swimmer flow field . . . . .	13
2.1	Synchronisation diagram for circular swimmers . . . . .	16
2.2	Circular microswimmer ordering dynamics . . . . .	17
2.3	Circular swimmer synchronisation example . . . . .	18
2.4	Circular swimmer order parameter dynamics . . . . .	19
2.5	Hysteresis in circular swimmer synchronisation . . . . .	19
2.6	Dynamic phase diagram and diffusive dynamics of a 2D dry system of chiral active particles with circular trajectories . . . . .	20
2.7	Mean square displacement for circular swimmers in the active and synchronising states . . . . .	21
2.8	Circular microswimmer diffusive dynamics . . . . .	22
2.9	Random close packing for circular swimmers . . . . .	24
2.10	De-synchronisation of circular microswimmers . . . . .	25
3.1	Synchronisation diagram for helical swimmers . . . . .	28
3.2	Helical microswimmer ordering dynamics . . . . .	29
3.3	Frequency and phase locking for helical microswimmers . . . . .	30
3.4	Circular-helical microswimmer synchronisation state diagram com- parison . . . . .	31
3.5	Helical swimmer order parameter dynamics . . . . .	32
3.6	Helical swimmer racemic mixture ordering dynamics . . . . .	34
3.7	Helical swimmer racemic mixture order parameter analysis . . . . .	35
3.8	Helical swimmer racemic mixture snapshot . . . . .	36
3.9	Racemic mixture cross-population phase-lag analysis . . . . .	37
3.10	Circular swimmer racemic mixture order parameter analysis . . . . .	38
3.11	Polar rotational autocorrelation function for a racemic mixture of circular microswimmers . . . . .	39
4.1	Phase separation for circular swimmers . . . . .	42
4.2	Reynolds number and size effect in circular microswimmer suspen- sions . . . . .	43

4.3	Size effect in circular microswimmer suspensions . . . . .	44
4.4	Small circular microswimmers . . . . .	46
4.5	Large-scale simulations of circular microswimmers . . . . .	47
4.6	Examples of phase separated circular microswimmer suspensions . . . . .	49
4.7	Radial distribution function for phase separation dynamics of circle swimmers . . . . .	51
4.8	Post-synchronisation velocity analysis for circular swimmers . . . . .	53
4.9	Enhanced diffusivity for circle swimmers . . . . .	54
4.10	Post-synchronisation circular microswimmer dynamics . . . . .	56
4.11	Advection in phase-separated circular microswimmer suspensions . . . . .	58
4.12	Tracking circular microswimmer trajectories before and after phase separation . . . . .	60
4.13	Traveling bands with local polarisation in circle microswimmer suspensions . . . . .	62
4.14	Squirmer velocity analysis for travelling band with local polar order . . . . .	63
A.1	Classic neutral squirmer . . . . .	70
A.2	Neutral squirmers in x and y directions . . . . .	71
A.3	Classic shaker . . . . .	72
A.4	The $B_{21}$ and $\widetilde{B}_{21}$ modes . . . . .	72
A.5	The $B_{22}$ mode . . . . .	73
A.6	Shakers in the x and y directions . . . . .	74
A.7	Building a shaker (stresslet) in the x direction . . . . .	75
A.8	Building a shaker (stresslet) in the x direction . . . . .	75
A.9	Building a classic puller and pusher . . . . .	76
A.10	Building a puller and pusher in the x direction . . . . .	77
A.11	Building a puller and pusher in the x direction . . . . .	77
B.1	Local spherical coordinate system for a squirmer of radius $R$ . . . . .	79
B.2	Self-propulsion of squirmer with azimuthal slip-flow . . . . .	82

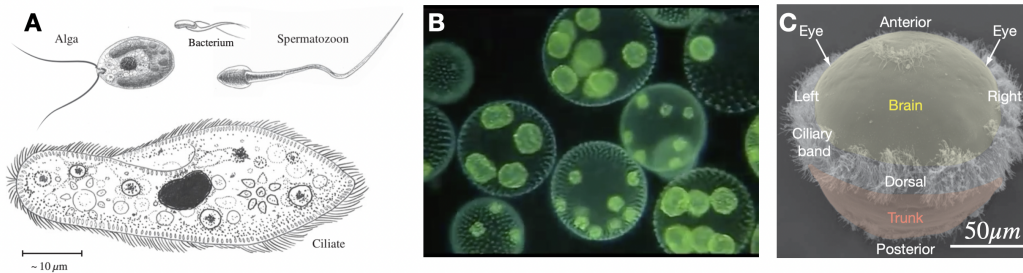


.....

# Introduction

Microswimmers comprise a subset of active matter systems where microscopic entities are capable of self-propelling themselves within a fluid environment. Natural microswimmers consisting of biological microorganisms such as bacteria, protists, ciliates and sperm cells are abundant in nature; representing most of the world’s biomass. Their collective dynamics has gained a considerable amount of interest of late [1–9] and has inspired the current surge in synthetic microswimmer research, typically based on phoretic Janus particles [10–12]. The interest for developing artificial swimmers has been fuelled by the various promising possibilities for applications such as micro-cargo transportation [13–16], targeted drug delivery [16–19], artificial insemination [16, 20], microsurgery [16, 17, 21–23] and water purification [24, 25] to name a few.

## Biological swimmers



## Artificial swimmers



**Figure I.1. Examples of biological and artificial microswimmers.** Examples of biological and artificial microswimmers taken from the literature. A: Schematic representation of alga, bacteria, spermatozoon and ciliate drawn to relative scale [26]; B: the spherical colony of the flagellated green alga volvox [27]; C: Scanning electron micrograph of a 48-h marine zooplankton larva [28]; D: An image of a Janus particle [29]; E: schematic representation of Janus particles and bacteria drawn to scale [25]; F: Images of artificial microswimmers with different shapes [30].

Most theoretical studies of microswimmer suspensions have concentrated on particles that swim in straight lines, with simulations predicting the spontaneous formation of collective swimming along a common direction — uniform polar order [31–37]. However, most microorganisms generally tend to swim along helical paths [28, 38–46]. Similarly, any asymmetry due to imperfections in the

shape of the colloids or in their catalytic coating would also lead to chiral motion for artificial swimmers [10, 47–49]. The fact of the matter being that when dealing with microswimmers, rectilinear motion is more the exception rather than the norm.

Continuum descriptions based on the long-range hydrodynamics produced by flow singularities [50–53] have been extensively used in the past, with some works including chiral flows [54–56]. However, these models fail to capture near-field hydrodynamic effects, which are believed to be crucial for the formation of polar order [33, 34]. Nevertheless, these models are presented with difficulties in capturing the specificities associated with non-dilute suspensions of interacting finite-volume swimmers.

Most of the current theoretical work of active particles moving along chiral paths relies on dry microscopic descriptions such as active Brownian particle (ABP) models [57–66]. These effectively account for excluded volume effects, but neglect hydrodynamic interactions. Simulations of rotational dry models have predicted large-scale synchronisation, when a Kuramoto-type alignment term is included [58, 67]. Very recently, work on the hydrodynamics of chiral swimmers in 3D has started to emerge, but has so far been limited to single and two particle systems [68–73].

Explicitly incorporating chirality in hydrodynamic models used to study microswimmer suspensions could have an important effect regarding the emergence of collective states, such as large-scale collective oscillations [74, 75], polar order [31–37] or hydrodynamic synchronisation [76–82]. While synchronisation arising from active flows has been predicted for linear trimers [76] and for rotors on a 2-dimensional lattice [80], the ability of microswimmers to spontaneously synchronise (or not) in freely moving bulk suspensions, remains an open question.

In this work, we consider three-dimensional, wet, many-body systems of active finite-sized spherical particles with intrinsic chiral trajectories. We perform low-Reynolds-number numerical simulations of the microswimmer suspensions at various biologically relevant packing fractions and study the collective behaviour of the system. We employ neutrally buoyant particles with no net force or torque acting on them that undergo circular or helical trajectories in isolation and interact between them solely through hydrodynamic and steric interactions.

We show that swimmers with chiral trajectories can synchronise their rotation in a fully three-dimensional suspension. We consider finite sized swimmers, with a surface slip-flow arising from the general solution for self-propulsion at low Reynolds numbers [83], corresponding to a rotating source dipole flow inclined at an angle  $\psi$  with respect to the particle polar direction. A synchronised state, corresponds to the alignment of these dipoles. We study three distinct cases: circular swimmers, helical swimmers, and a racemic mixture of left-handed and right-handed helical swimmers. In all cases, the spontaneous formation of synchronised states is observed. For some cases, we observe post-synchronisation collective phenomena such as phase separation or travelling bands with local polarisation; showing that despite the simplicity of its

constituents, the system boasts a richness of complex phenomena.

We begin with a presentation of the model and simulation method in the next chapter (chapter 1), before moving on to study synchronisation in suspensions of circular swimmers in chapter 2 and helical swimmers in chapter 3. We study the global degree of alignment in the system, which is directly linked to the emergence of synchronisation, and construct phase diagrams for both circular and helical swimmers, pointing out the key features and main differences between each case. In chapter 3, we present a racemic mixture, which displays a fascinating behaviour where alignment and synchronisation are attained at the subpopulation level while the suspension remains homogeneously mixed. Finally, in chapter 4, we touch upon our most recent, preliminary findings. These involve observations of spontaneous, post-synchronisation phase separation and the emergence of propagating waves with local polarisation throughout the system. We then conclude the work with a brief discussion regarding the significance our results.





# 1 Model for rotational squirmers

This chapter introduces the so called squirmer model. The model was originally introduced by Lighthill in 1952 [84] and then extended by Blake in 1971 [85]. It describes the surface flow, or slip velocity,  $\mathbf{u}$  of the active particle which is used as the boundary condition for the velocity field enabling the self-propelled motion of a spherical body at low Reynolds numbers ( $\text{Re} \ll 1$ ). This is also known as the pumping problem. Until the present day, its use is widespread, being one of the standard models for the study of self-propelling particles in Stokes flow.

## 1.1 The Stokes equations

Before introducing the model used in this work, we give a brief overview of the fundamental physical concepts required to build the model in the first place. Namely, the Stokes equations. These equations describe the fluid flow at the low Reynolds number regime ( $\text{Re} \ll 1$ ). In this regime, the viscous forces dominate the advective forces allowing us to approximate the Navier-Stokes equations for an incompressible fluid to:

$$\nabla p = \mu \nabla^2 \mathbf{u} \tag{1.1}$$

$$\nabla \cdot \mathbf{u} = 0 \tag{1.2}$$

where  $p$  is the fluid pressure,  $\mu$  the fluid viscosity and  $\mathbf{u}$  the fluid velocity.

Evidently, equations (1.1) and (1.2) are significantly more simple than the full Navier-Stokes equations. More importantly, the linearity of the equations leads to important properties that can present interesting ramifications for low Reynolds number locomotion. For example, the property of superposition, or the property of rate independence which leads to the scallop theorem [86–88]. The absence of time ( $t$ ) in the equations, leads to the property of instantaneity. Meaning that all frames of reference are inertial frames and allowing us to study the problem in any frame that we find convenient.

## 1.2 The standard squirmer model

In its most commonly used form (what we refer to as the standard squirmer model) the squirmer model corresponds to the axisymmetric slip velocity at the surface of a particle of radius  $a$  given by:

$$u_\theta|_{r=a} = B_1 \sin\theta + \frac{1}{2}B_2 \sin 2\theta \quad (1.3)$$

where  $\theta$  is the polar angle with respect to the particle's axis of symmetry.  $B_1$  and  $B_2$  are coefficients that are used to obtain different slip velocity profiles for the squirmer that can lead to significant qualitative differences in their collective dynamics.

Equation 1.3 is often reformulated as:

$$u_\theta|_{r=a} = \frac{3}{2}u_0 \sin\theta(1 + \beta \cos\theta) \quad (1.4)$$

where  $\beta = B_2/|B_1|$  is defined as the squirming parameter and  $u_0 = 2B_1/3$  is the bulk swimming speed of a freely-moving, non-interacting squirmer. In the next section, we explain how the bulk swimming speed  $u_0$  is obtained through the reciprocal theorem for Stokes flows [89].

The squirming parameter  $\beta$  allows the classification of microswimmers into 4 different types: neutral squirmers ( $\beta = 0$ ), pushers ( $\beta < 0$ ), pullers ( $\beta > 0$ ) and shakers ( $\beta \pm \infty$ ).

In appendix A, we give schematic representations of each type of squirmer that were created using the Wolfram Mathematica software [90]. We explain in detail how to build each type of squirmer by combining different modes appearing in Lamb's general solution for Stokes flows [91].

Pusher,  $\beta = -5$       Neutral,  $\beta = 0$       Puller,  $\beta = 5$

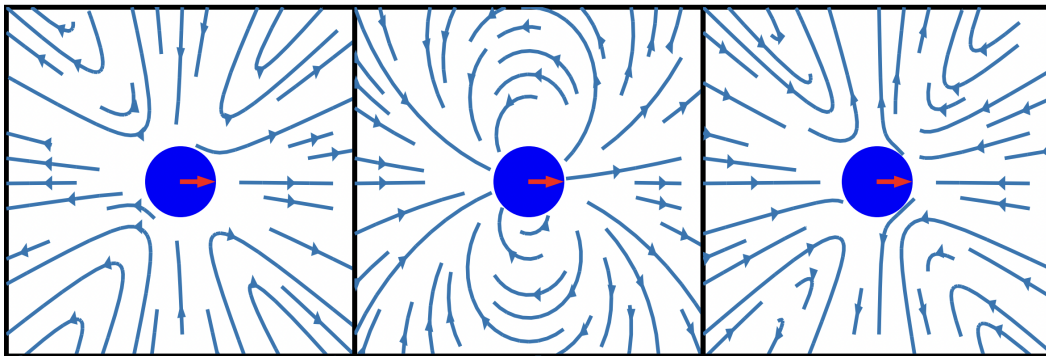


**Figure 1.1. The standard squirmer model.** Analytical flow field of a pusher (left) with  $\beta = 5$ , a neutral squirmer (middle) and a puller (right) with  $\beta = -5$ . Image taken from [92]

### 1.3 Reciprocal theorem for the standard squirmer model

Stone and Samuel derived an integral theorem using the principle of virtual work [89] which can be used to calculate the resulting bulk swimming velocity  $\mathbf{U}$  and angular velocity  $\mathbf{\Omega}$  of a particle due to a slip flow (disturbance motion)  $\mathbf{u}$  at its surface. For a standard squirmer with radius  $a$  we have:

$$\mathbf{U}(\mathbf{t}) = -\frac{1}{4\pi a^2} \int_S \mathbf{u} dS \quad (1.5)$$

$$\mathbf{\Omega}(\mathbf{t}) = -\frac{3}{8\pi a^3} \int_S \mathbf{n} \times \mathbf{u} dS \quad (1.6)$$

with,  $\mathbf{n} = \hat{\mathbf{e}}_r$  normal to the surface  $S$ ,  $dS = R^2 \sin\theta d\theta d\phi$ , and  $\mathbf{u}$  given by equation 1.3 (or 1.4).

Using generalised coefficients, with  $b_1 = B_1$  and  $b_2 = B_2$  for the standard squirmer model, and writing the slip flow as  $\mathbf{u} = \sin\theta(b_1 + b_2 \cos\theta) \hat{\mathbf{e}}_\theta$ , equations 1.5 and 1.6 in cartesian coordinates become:

$$\mathbf{U} = -\frac{a^2}{4\pi a^2} \int_0^\pi \int_0^{2\pi} (b_1 \sin\theta + b_2 \sin\theta \cos\theta) (\cos\theta \cos\phi, \cos\theta \sin\phi, -\sin\theta) \sin\theta d\theta d\phi \quad (1.7)$$

$$\mathbf{\Omega} = -\frac{3}{8\pi a} \int_0^\pi \int_0^{2\pi} \sin^2\theta (b_1 + b_2 \cos\theta) (-\sin\phi, \cos\phi, 0) d\theta d\phi \quad (1.8)$$

Breaking equation 1.7 into components:

$$U_x = -\frac{1}{4\pi} \int_0^\pi \int_0^{2\pi} (b_1 \sin^2\theta \cos\theta \cos\phi + b_2 \sin^2\theta \cos^2\theta \cos\phi) d\theta d\phi \quad (1.9)$$

$$U_y = -\frac{1}{4\pi} \int_0^\pi \int_0^{2\pi} (b_1 \sin^2\theta \cos\theta \sin\phi + b_2 \sin^2\theta \cos^2\theta \sin\phi) d\theta d\phi \quad (1.10)$$

$$U_z = -\frac{1}{4\pi} \int_0^\pi \int_0^{2\pi} (-b_1 \sin^3\theta - b_2 \sin^3\theta \cos\theta) d\theta d\phi \quad (1.11)$$

When integrating with respect to  $\phi$  from 0 to  $2\pi$ , equations (1.9) and (1.10) will give 0 since they are comprised of the functions  $\sin\phi$  and  $\cos\phi$ . Therefore:  $\mathbf{U} = U_z \hat{\mathbf{z}}$ .

Similarly for equation (1.8), since the dependence on  $\phi$  in the two non-zero components is of the type  $\sin\phi$  or  $\cos\phi$ , the angular velocity in these directions will be zero ( $\Omega_x = \Omega_y = 0$ ). Therefore, for the classic standard squirmer model we find:  $\mathbf{\Omega} = 0$ , leaving us with just equation (1.11) to solve.

In order to make this work more pleasant to read, we skip the steps required to reach the solution of (1.11) and refer the reader to appendix B.1 for the step by step solution.

Finally, the resulting translational and rotational motion of a standard squirmer is given by:

$$\mathbf{U} = \frac{2b_1}{3}\hat{\mathbf{z}} = \frac{2B_1}{3}\hat{\mathbf{z}} \equiv u_0\hat{\mathbf{z}} \quad (1.12)$$

$$\boldsymbol{\Omega} = 0 \quad (1.13)$$

The reciprocal theorem for the standard squirmer model therefore proves that only the  $B_1$  coefficient, coming from the source dipole (neutral squirmer) contribution plays a role in the *net* movement of the squirmer. The  $B_2$  mode corresponding to the stresslet (see appendix A) only mixes the fluid and does not contribute to the net total movement of the particle. Hence the name “shaker” for the case where  $B_1 = 0$  ( $\beta \pm \infty$ ). Pushers and pullers therefore both swim and mix the surrounding fluid whereas neutral squirmers swim and do not mix the fluid.

A schematic representation of the source dipole or neutral squirmer with its characteristic axisymmetric surface flow is shown in Fig. 1.2. In Fig. 1.2, the squirmer has its axis of symmetry aligned with the  $z$ -direction along which it moves with speed  $u_0$ , and its slip flow is given by equation 1.3 (or 1.4). More specifically:

$$u_\theta|_{r=a} = B_1 \sin\theta = \frac{3}{2}u_0 \sin\theta \quad (1.14)$$

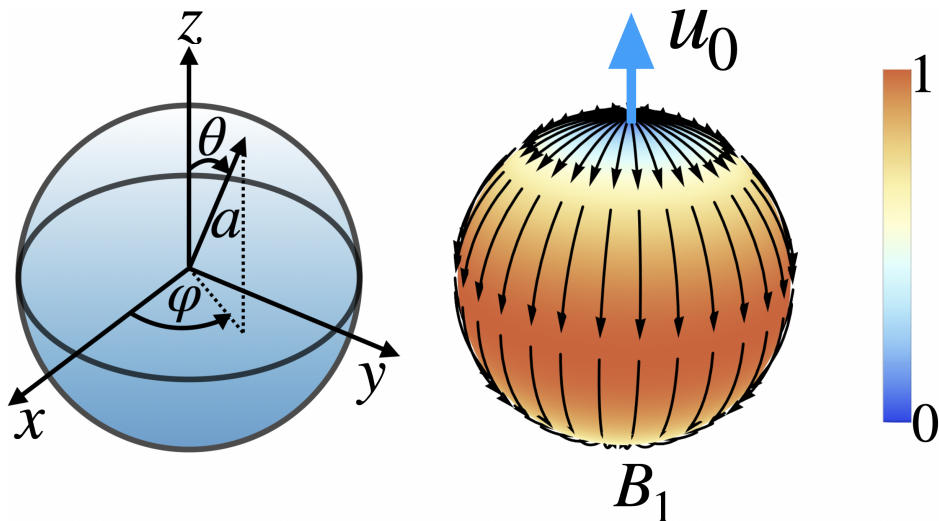


**Figure 1.2. Self-propulsion of the neutral squirmer.** Local spherical coordinate system for a squirmer of radius  $a$  (left) and surface slip flow of the  $B_1$  mode of the squirmer model leading to self-propulsion speed  $u_0$  in the positive  $z$ -direction (middle). The magnitude of the normalised surface flow is represented by the colour scheme (right) from blue to orange and black streamlines indicate the direction of the slip flow.

With the standard squirmer model, the particles are limited to just swimming in straight lines. As discussed in the introduction, in many cases this is

not ideal for obtaining an accurate description of real microswimmers. In the next section, we go beyond the standard squirmering model, to include azimuthal flows via the rotlet term of the general squirmer model which will enable us to construct squirmers that swim along circular and helical paths.

## 1.4 Squirmer model for circular and helical swimming

Following the work done by Pak and Lauga [83] on using Lamb's general solution in Stokes flow [89] to analytically derive the exact solution of the flow field and swimming kinematics of a nonaxisymmetric squirmer, we create squirmers with circular and helical trajectories.

The *purely tangential* slip velocity profile on the surface of a squirmer of radius  $a$ , found in an incompressible fluid at low Reynolds numbers  $\text{Re} \sim 0$ , is given in spherical coordinates by an infinite series of modes for the polar and azimuthal components  $\mathbf{e}_\theta$  and  $\mathbf{e}_\phi$ :

$$u_r|_{r=a} = 0 \quad (1.15)$$

$$\begin{aligned} u_\theta|_{r=a} = & \\ & \sum_{n=1}^{\infty} \sum_{m=0}^n \left[ \frac{-2 \sin\theta P_n^{m'}}{na^{n+2}} (B_{mn} \cos m\phi + \tilde{B}_{mn} \sin m\phi) \right. \\ & \left. + \frac{m P_n^m}{a^{n+1} \sin\theta} (\tilde{C}_{mn} \cos m\phi - C_{mn} \sin m\phi) \right] \end{aligned} \quad (1.16)$$

$$\begin{aligned} u_\phi|_{r=a} = & \\ & \sum_{n=1}^{\infty} \sum_{m=0}^n \left[ \frac{\sin\theta P_n^{m'}}{a^{n+1}} (C_{mn} \cos m\phi + \tilde{C}_{mn} \sin m\phi) \right. \\ & \left. + \frac{2m P_n^m}{na^{n+2} \sin\theta} (\tilde{B}_{mn} \cos m\phi - B_{mn} \sin m\phi) \right] \end{aligned} \quad (1.17)$$

where  $P_n^m = P_n^m(x)$  with  $x = \cos\theta$  are the associated Legendre polynomials (with  $n \geq 1$  and  $0 \leq m \leq n$ ) and each mode can be identified by its corresponding coefficient:  $B_{mn}$ ,  $\tilde{B}_{mn}$ ,  $C_{mn}$  and  $\tilde{C}_{mn}$ .

Equations (1.15) to (1.17) define the boundary conditions for the pumping problem — i.e., the flow field produced without considering the contribution from the induced motion of the squirmer as a consequence of the very same boundary actuation. As shown in the preceding section, the contribution of the induced translational and rotational motion of the squirmer can be calculated by integral theorems and added to the pumping problem solution to give the overall flow field of the squirmer:

$$\mathbf{v} = \mathbf{u} + \mathbf{u}_T + \mathbf{u}_R \quad (1.18)$$

where  $\mathbf{u} = u_r \mathbf{e}_r + u_\theta \mathbf{e}_\theta + u_\phi \mathbf{e}_\phi$  is the solution of the pumping problem and  $\mathbf{u}_T, \mathbf{u}_R$  are the flows due to the induced translation ( $\mathbf{U}$ ) and rotation ( $\mathbf{\Omega}$ ).

When  $m = 0$ , we obtain axisymmetric flow fields about the  $z$ -axis of the squirmer's *local* spherical coordinate system (see Fig.1.2) — or what is commonly referred to as the polar axis (we will use these two terms interchangeably throughout this work). In this case, the  $B_{01}$  and  $B_{02}$  modes correspond to the forementioned, well-known and widely-used  $B_1$  and  $B_2$  coefficients appearing in the standard squirmer model:  $\mathbf{u} = B_1 \sin\theta + \frac{1}{2}B_2 \sin\theta$ . The contribution of the  $B_1$  term to the overall flow field surrounding the squirmer corresponds to that of a source dipole oriented along the polar axis and is responsible for the *translational* motion of the particle along this axis with speed  $v_0 = \frac{2}{3}B_1$ .  $B_2$  corresponds to a stresslet and is the mixing term, leading to a force dipole flow field around the squirmer (in the polar/ $z$ -direction), and is used for defining pushers and pullers (see appendix A) which we do *not* consider in this work. Finally, the  $C_{0n}$  mode, which we will refer to as  $C_1$ , defines a rotlet in the  $z$ -direction and is the only mode that leads to *rotational* motion about the polar axis (see appendix B.4). However, it is important to note that the contribution of the rotlet to the overall flow field is null. Given that there is no external torque acting on the system and the swimmer is spherical in shape, the flow from the pumping problem cancels out completely with that due to its induced rotational motion, and angular momentum is effectively conserved (this is very nicely explained by Pak and Lauga in [83]). At  $\text{Re} = 0$ , a squirmer comprised of *just* the rotlet term therefore rotates without disturbing the surrounding fluid.

The modes with  $n = 1$  and  $m = 1$  are equivalent to the  $n = 1$  and  $m = 0$  modes discussed above but act in different directions. That is, their axis of symmetry is not the polar axis (or  $z$ -axis). The  $B_{11}$  and  $C_{11}$  modes are axisymmetric about the  $x$ -axis, and the  $\widetilde{B}_{11}$  and  $\widetilde{C}_{11}$  modes are axisymmetric about the  $y$ -axis. Therefore, perhaps the “simplest” case of a squirmer that does *not* swim in a straight line, consisting of just a hydrodynamic source dipole in the overall flow field (neutral squirmer), can be constructed by combining  $B_1$  with  $C_{11}$  or  $\widetilde{C}_{11}$ ;  $B_{11}$  with  $C_1$  or  $\widetilde{C}_{11}$ ; or  $\widetilde{B}_{11}$  with  $C_1$  or  $C_{11}$ . (Using  $B_1 + C_1$ ,  $B_{11} + C_{11}$ , or  $\widetilde{B}_{11} + \widetilde{C}_{11}$  would produce squirmers that swim in a straight line while spinning around their axis of symmetry). Each one of the six pairs of modes mentioned above leads to the squirmer having a circular trajectory in a given plane perpendicular to its axis of rotation. Fig. 1.3 of the next section gives a schematic representation of such a case.

Going one step further, helical motion can be produced by adding another “ $B$ ” mode (source dipole) in the direction of the axis of rotation of the squirmer, perpendicular to the plane of its circular motion. What this effectively does is lead to a situation where the induced rotational and translational velocities of the squirmer are no longer perpendicular ( $\mathbf{U} \times \mathbf{\Omega} \neq 0$  and  $\mathbf{U} \cdot \mathbf{\Omega} \neq 0$ ). The superposition of the two perpendicular source dipoles effectively leads to a source dipole along the diagonal with an angle given by the relative strength of the initial dipoles (see Figs. 1.4 and 1.5 of the following sections). This will be explained further and made more clear by end of this chapter as we go into the

specifics of the model.

## 1.5 Choosing the parameters for chiral swimmers

Without loosing generality, in this work, we use  $C_1 + \tilde{B}_{11}$  for circular swimmers; and  $B_1 + C_1 + \tilde{B}_{11}$  for helical swimmers (see Figs. 1.3 and 1.4). Hence, the boundary conditions defining the slip velocity profile of our squirmer model are given in the polar  $\hat{e}_\theta$  and azimuthal  $\hat{e}_\varphi$  directions, by:

$$\begin{aligned} u_\theta|_{r=a} &= B_1 \sin\theta + \tilde{B}_{11} \cos\theta \sin\varphi \\ u_\varphi|_{r=a} &= C_1 \sin\theta + \tilde{B}_{11} \cos\varphi, \end{aligned} \quad (1.19)$$

with the  $B_1$ ,  $C_1$  and  $\tilde{B}_{11}$  coefficients being our model parameters.

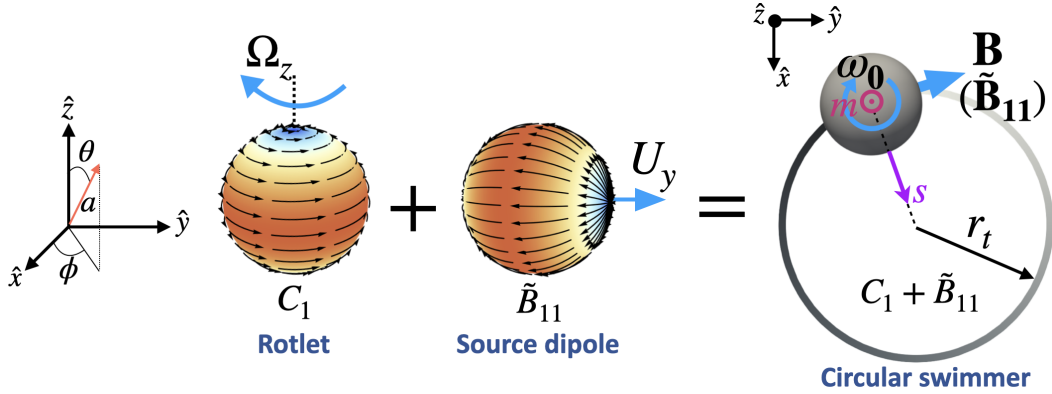


**Figure 1.3. Building circular swimmers.** Model for circular squirmers. The surface slip-flows corresponding to the modes:  $C_1$  and  $\tilde{B}_{11}$  in the particle frame (left and middle). The magnitude of the normalised surface velocity (slip flow) for each mode is represented by a colour-code just like in Fig. 1.2 and the streamlines are coloured black. The particle trajectory in the lab frame corresponding to circular swimming perpendicular to the polar axis ( $z$  or  $\mathbf{m}$ ) with radius  $r_t$  (right) and an angular velocity  $\omega_0$ . The unit vectors  $\mathbf{m}$  and  $\mathbf{s}$  correspond to the particle polar and azimuthal axes respectively.

In order to study synchronisation, and more generally the level of alignment in the system, we define the local azimuthal  $\mathbf{s}$  and polar  $\mathbf{m}$  unit vector of the swimmer as shown in Fig. 1.3 and Fig. 1.4.  $\mathbf{m}$  points in the direction of the swimmer's polar axis ( $z$ -axis); and  $\mathbf{s}$  points in the direction of the (local)  $x$ -axis. For circular swimmers,  $\mathbf{s}$  points towards the centre of the circular path, and for helical swimmers it points towards the screw axis.

The  $B_1$  mode corresponds to the source dipole in the standard squirmer model (bottom left in Fig. 1.4).  $C_1$  leads to a rotation of the particle around its polar axis  $z$  (or  $\mathbf{m}$ ) with an angular velocity  $\omega_0 = C_1/a$  (left in Fig. 1.3 and top left in Fig. 1.4).  $\tilde{B}_{11}$  corresponds to a source dipole along  $\mathbf{y}$  (middle in Fig. 1.3

and top right in Fig. 1.4). The total swimmer flow field corresponds to a single source dipole  $\mathbf{B}$  with magnitude  $B = \sqrt{\tilde{B}_{11}^2 + B_1^2}$ , which rotates around the polar axis ( $\mathbf{m}$ ) at an inclination  $\psi = |\tan^{-1}(\tilde{B}_{11}/B_1)|$  (Fig. 1.4). As already shown in the previous section, an isolated particle has a swimming speed  $v_0 = \frac{2}{3}B$ . When  $\psi = 90^\circ$  ( $B_1 = 0$ ) the swimmers have circular trajectories in the plane perpendicular to  $\mathbf{m}$  (right in Fig. 1.3). The radius of the trajectory is given by  $r_t = 2\tilde{B}_{11}a/(3C_1)$  and the period by  $T_0 = 2\pi/\omega_0 = 2\pi a/C_1 = 2\pi r_t/\tilde{B}_{11}$ .

For  $\psi \neq 90^\circ$  and  $\psi \neq 0^\circ$  the trajectories become helical with pitch length  $p = 4\pi B_1 a/(3C_1)$  corresponding to the distance  $p$  travelled along the direction given by the particle's polar axis  $\mathbf{m}$  during one period  $T_0$  (bottom left in Fig. 1.4). To characterise the helical swimming ( $0^\circ < \psi < 90^\circ$ ), we define the ratio  $\lambda \equiv r_t/p = \tilde{B}_{11}/(2\pi B_1)$ , which leads to:  $\psi = |\tan^{-1} 2\pi\lambda|$ .

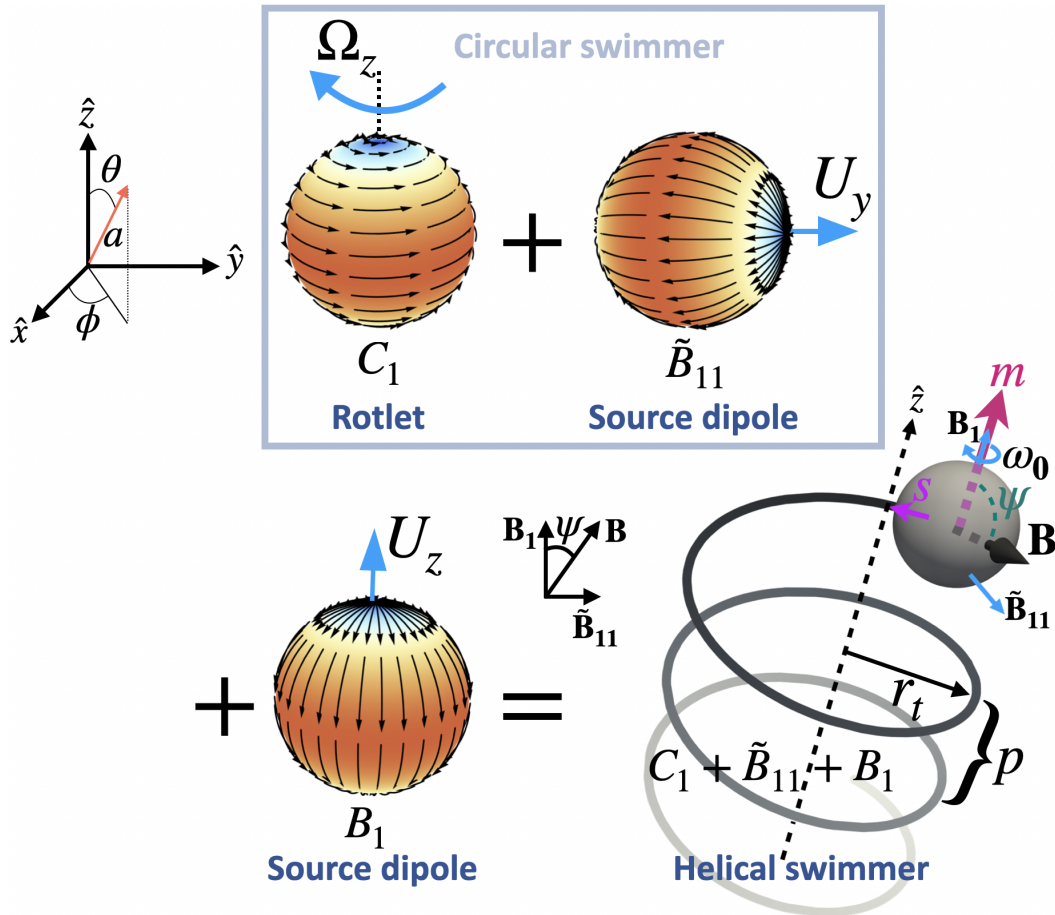


**Figure 1.4. Building helical swimmers.** Model for helical squirmers. The surface slip-flows corresponding to the modes:  $B_1$ ,  $C_1$  and  $\tilde{B}_{11}$  in the particle frame (top and bottom left). The magnitude of the normalised surface velocity (slip flow) for each mode is represented by a colour-code just like in Fig. 1.2 and the streamlines are coloured black. The particle trajectory in the lab frame corresponds to helical swimming along the polar axis ( $\mathbf{z}$  or  $\mathbf{m}$ ) with radius  $r_t$ , angular velocity  $\omega_0$  and a pitch length  $p$  (bottom right). The unit vectors  $\mathbf{m}$  and  $\mathbf{s}$  correspond to the particle polar and azimuthal axes respectively and  $\psi$  is the inclination angle with respect to  $\mathbf{m}$  that depends on the relative strength of the  $B_1$  and  $\tilde{B}_{11}$  modes.

## 1.6 Simulation details

To study the collective dynamics of suspensions of  $N$  swimmers, we use the lattice Boltzmann method, where the microswimmers are modelled as spherical squirmes with radius  $a$  [93, 94]. The no-slip boundary condition at the particle surface [95–97], is modified to take into account the active slip-flows [98, 99].

We use lattice units where distance is given by the lattice spacing  $\Delta x = 1$  and time in simulation time-steps  $\Delta t = 1$ . Particles of radius  $a$  (and diameter  $\sigma$ ) are placed within a cubic lattice  $L_x = L_y = L_z$  with periodic boundary conditions, corresponding to a volume  $V$ . A short-range repulsive interaction is implemented to avoid particle overlaps [93, 94] with a cut-off distance of  $1\Delta x$ .

The fluid density is set to  $\rho = 1$  and the dynamic viscosity to  $\mu = 0.5$ . For this entire work we set  $C_1 = 0.001$  leading to an intrinsic angular velocity of

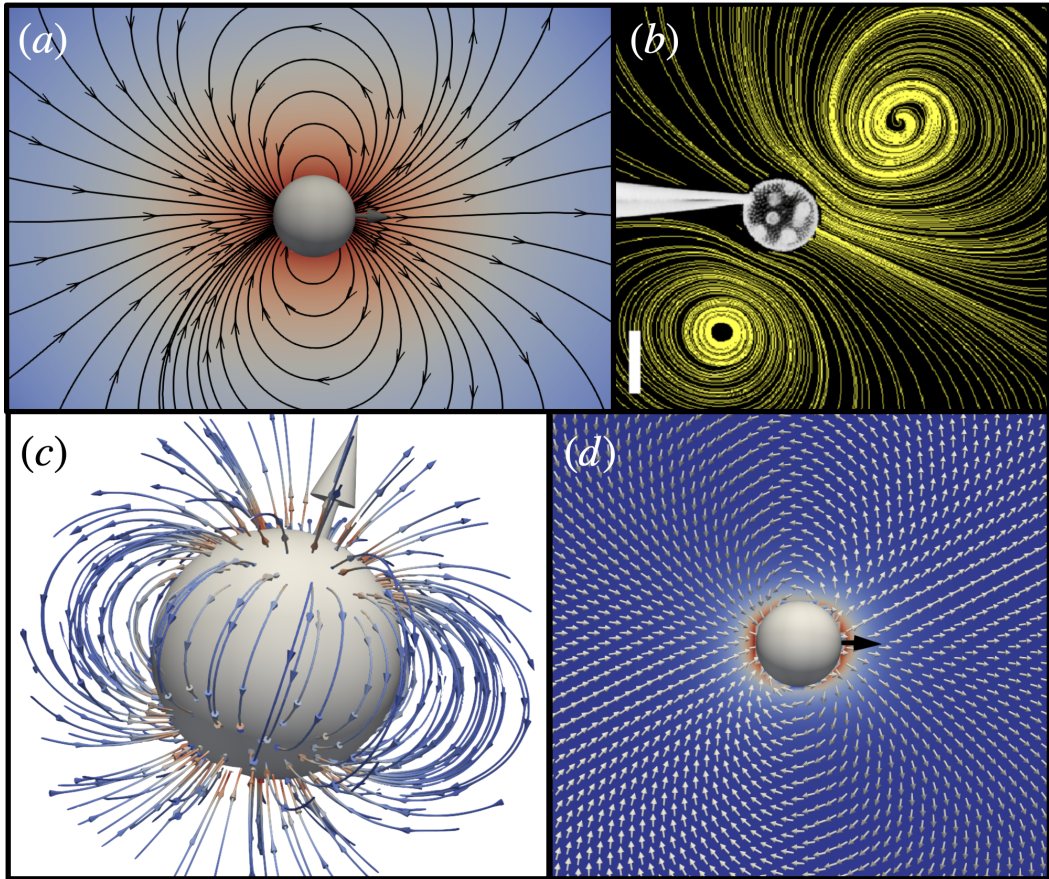


**Figure 1.5. Rotational swimmer flow field.** (a), (c) and (d): Circular and helical swimmer flow field obtained directly from the simulations, corresponding to a source dipole  $\mathbf{B}$  (neutral squirmer). (b) Image of a neutral squirmer flow field form [100] for comparison with simulation results. The magnitude of the fluid velocity is coloured using a logarithmic scale and overlaid by black streamlines in (a); and a linear scale overlaid by white arrows in (d). A 3D image of a rotational squirmer with its streamlines coloured in the linear scale according to the magnitude of the fluid velocity. Images (a), (c) and (d) were created using the Paraview visualisation software [101].

$\omega_0 = C_1/a = 1.25 \cdot 10^{-4}$  and to a rotational Reynolds number  $Re_\Omega = \rho\omega_0 a^2/\mu = 0.016$ . To realise different trajectory radii ( $r_t$ ) for a given  $a$  the source dipole strength is varied  $\widetilde{B}_{11} \in [0, 0.007]$ . These correspond to swimming speeds of  $v_0 = 2/3\widetilde{B}_{11} \in [0, 4.67 \cdot 10^{-3}]$  and  $r_t = v_0 a_0/C_1 \in [0, 4.67a]$ . The (linear) Reynolds number is given by:  $Re = \rho v_0 a/\mu$ . The typical particle Reynolds number throughout this work is  $Re \sim 0.1$ .

For the helical swimmers we use  $B_1 = 0.005$  and vary  $\widetilde{B}_{11} \in [0, 0.007]$  corresponding to a maximum  $Re \approx 0.09$ . The parameters give a pitch length  $p = 4\pi B_1 a/3C_1 \approx 21a$  (for the results presented in chapter 3).

Assuming a particle radius  $1\mu\text{m}$  and using the viscosity of water  $10^{-3}\text{Pas}$  as well as typical  $Re \sim 10^{-2}$ , a single lattice length  $\Delta x$  and time  $\Delta t$  can be mapped to  $\sim 0.1\mu\text{m}$  and  $\sim 10\mu\text{s}$ , respectively. Therefore a typical simulation run of  $\sim 10 \times 10^6$  LB steps corresponds to 100s in real time.

.....

## 2 Circular swimmers

As mentioned in the introduction, theoretical studies have predicted the spontaneous formation of uniform polarised flocks in suspensions of linear microswimmers [31–37]. In this chapter, we present the work we have carried out in order to discover if circle swimmers display a similar behaviour and align their velocities in such a way as to rotate in an ordered fashion. Namely, synchronisation.

An ordered state, corresponds to the alignment of the source dipoles  $\mathbf{B}$ . The amount of alignment can be measured by considering a velocity order parameter:

$$P_v(t) = \frac{|\sum_i^N \hat{\mathbf{v}}_i|}{N} \quad (2.1)$$

where  $\hat{\mathbf{v}}_i = \mathbf{v}_i/v_i$  is the unit velocity vector of particle  $i$ . To further quantify the ordering, we measure the alignment along the azimuthal  $\mathbf{s}$  and polar  $\mathbf{m}$  directions, by calculating:

$$P_{s|m}(t) = \frac{|\sum_i^N \mathbf{s}_i | \mathbf{m}_i |}{N} \quad (2.2)$$

Therefore,  $P_{v|s|m} = 1$  corresponds to complete order, and 0 to an isotropic state.

For the simulations, we generate initial configurations with the squirmers of radius  $a = 8$  randomly and homogeneously distributed in the simulation box in an isotropic state, with partial alignment, or in the fully ordered state. The simulations are typically run for a minimum run-time  $t_{max} = 500T_0$  (where  $T_0 = 2\pi/\omega_0$  is the intrinsic period of a single rotor) corresponding to  $\sim 25 \times 10^6 \Delta t$  LB steps. For dilute suspensions (packing fractions up to 10%), we use  $t_{max} = 1000T_0$  ( $\sim 50 \times 10^6 \Delta t$  LB steps).

### 2.1 Synchronisation of circular microswimmers

We find that circular swimmers are capable of reaching a globally synchronised state depending on the packing fraction  $\phi$ . More specifically, starting from isotropic initial conditions, spontaneous synchronisation is attained for:  $\phi \approx 3 \dots 23\%$  and  $r_t \approx 2 \dots 5a$ . The synchronisation diagram for circular swimmers with  $r_t \sim a$  is shown in Fig. 2.1. The synchronisation corresponds to the spontaneous alignment of the particle velocities, with the growth of both azimuthal and polar order, where typically  $P_s \approx P_m \approx P_v \gtrsim 0.85$  at long times (Fig. 2.2a).

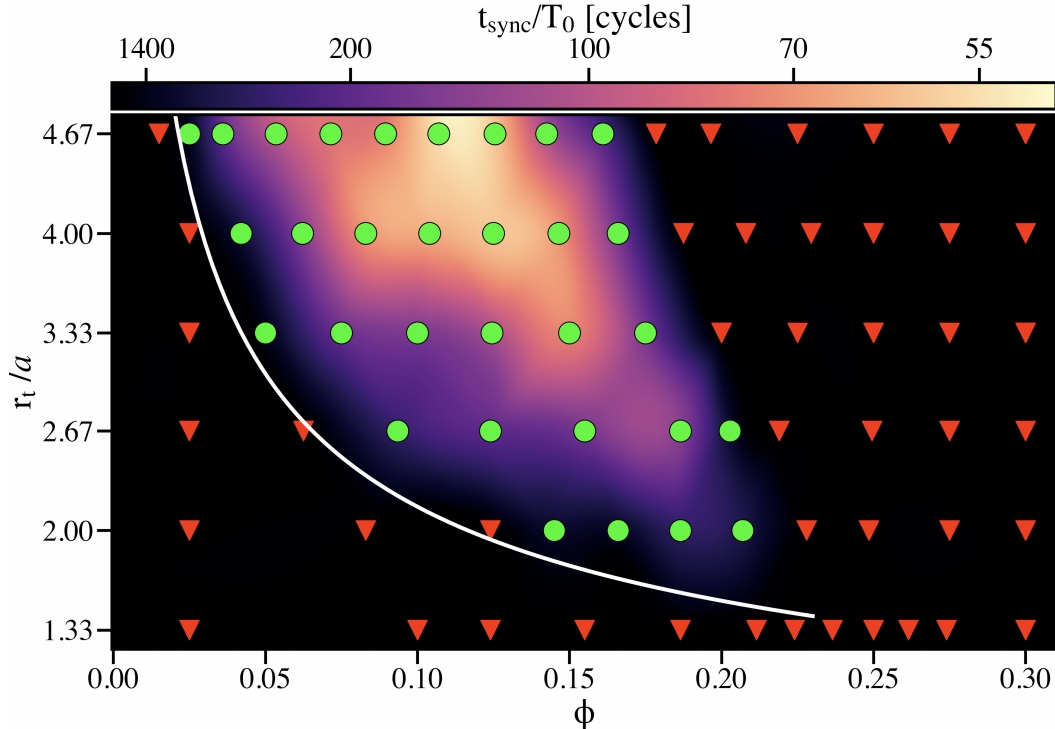


**Figure 2.1. Synchronisation diagram for circular swimmers.** Synchronisation diagram for circular swimmers ( $\psi = 90^\circ$ ) as a function of the volume fraction  $\phi$  and particle trajectory radius  $r_t$ . Green circles indicate global synchronisation, and the red triangles mark isotropic states. The synchronisation region is coloured according to a waiting time  $t_{sync}/T_0$  corresponding to the total time elapsed from the start of the simulation until synchronisation is reached. The white curve corresponds to  $\phi = \phi'_c \frac{4/3\pi a^3}{2\pi r_t^2 a}$  with  $\phi'_c = 70\%$ . (see subsection 2.3 for details).

In the steady state, the system shows both frequency and phase locking (Fig. 2.2c and d). The angular velocity  $\omega$  distribution has a peak at the single particle value  $\omega_0$  and its width corresponds to the fluctuations arising from the hydrodynamic coupling between the particles. These are reduced in the synchronised state (Fig. 2.2c). The phase locking is apparent from the distribution of the lag angle  $\alpha = \alpha_{1,2}^{\perp}$  calculated for all the particle pairs, by considering the angle between the  $\mathbf{s}$  vectors of two different rotors in the plane perpendicular to the global polar director,  $\mathbf{P}_M \sim \sum_i^N \mathbf{m}_i$ . The distribution of  $\alpha$  changes from uniform at  $t \approx 0$  to a normal distribution with a peak at  $\alpha \approx 0$  in the globally synchronised state (Fig. 2.2d). In this state, the particle trajectories are circular and aligned perpendicularly to  $\mathbf{P}_M$  (the global polar direction) (right in Fig. 2.3). The particle positions remain isotropic with the pair-correlation functions  $g(r)$ ,  $g(r_\perp)$  and  $g(r_\parallel)$  showing liquid-like structure (Fig. 2.2b).

The likelihood of the synchronisation depends on the volume fraction  $\phi$  and the trajectory radius  $r_t$  (Fig. 2.1). At low  $\phi$  the system remains in an isotropic state with the circular trajectories randomly oriented and distributed. For a dilute suspension, with very low  $\phi$ , the swimmers are far apart and carry out their circular trajectories seemingly independently. Since the flow field of the squirmers is that of a source dipole (decaying as  $\sim 1/r^3$  in the far-field), long range

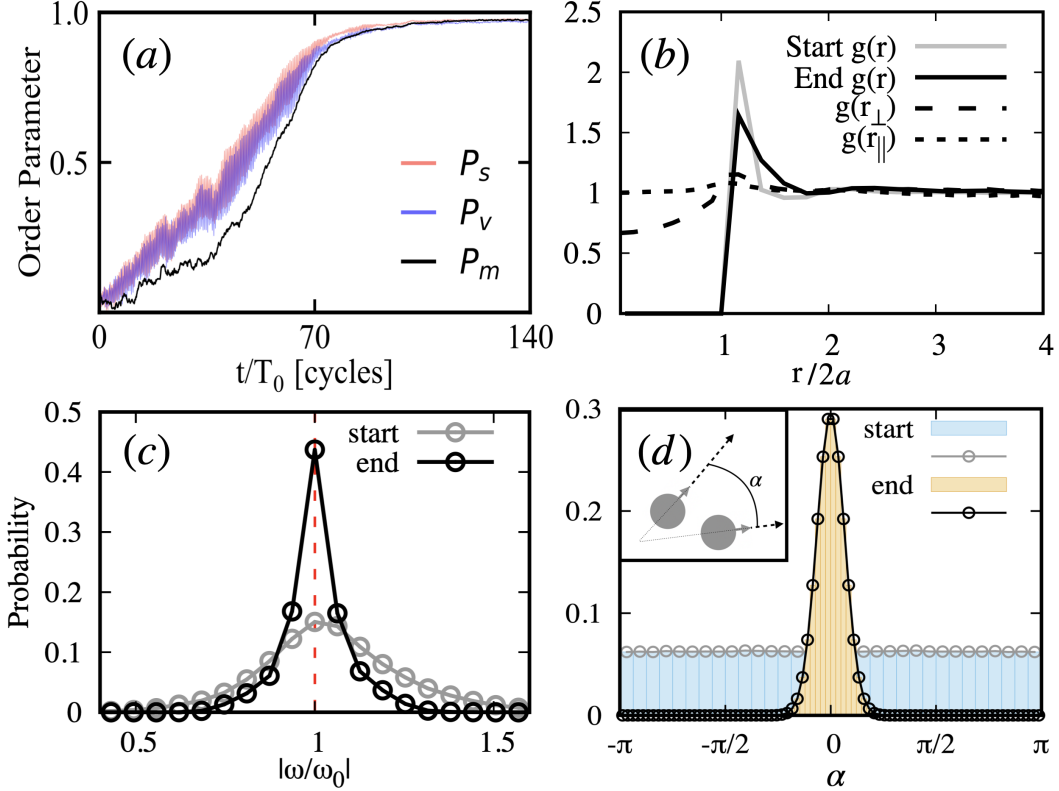


**Figure 2.2. Circular microswimmer ordering dynamics.** (a) Example of a typical time evolution of the azimuthal  $P_s$  (red), velocity  $P_v$  (blue) and polar  $P_m$  (black) order parameters. (b) Radial distribution function  $g(r)$  of the system at the beginning (gray) and at the end (black) of the simulation. The  $g(r_\perp)$  ( $g(r_\parallel)$ ) are calculated perpendicular (parallel) to the polar director  $\mathbf{P}_M$ . Probability distribution of the (c) angular velocities  $\omega$  and (d) phase lag angle  $\alpha$  between all particle pairs, at the start and end of the simulation. (The data corresponds to  $\phi \approx 0.15$  and  $r_t \approx 3.33a$ ).

hydrodynamic dipole-dipole interactions are present. Hence, for the moment we cannot rule out with certainty the possibility of these systems eventually synchronising over longer, computationally-prohibitive, time scales; even though there appear to be no changes in the order parameter values over our chosen waiting time  $t_{max}$ . In the final subsection of this chapter we address this.

When  $\phi$  is increased, the trajectories become jagged in the isotropic state (left in Fig. 2.3). At long times the trajectories align (right in Fig. 2.3). The distribution of rotational frequencies  $\omega$  has a peak at  $\omega_0$  and the width likely arises from the hydrodynamic fluctuations (Fig. 2.2c).

To study the ordering dynamics, we measure the total time  $t_{sync}$  from the beginning of the simulation until synchronisation is reached. Here, both  $P_s$  and  $P_m$  reach a plateau. In general, when studying the order parameter evolution with time, the dynamics leading to synchronisation seem to be quite rich and diverse. This indicates that there could be more than one path for the system to reach the synchronised state. Fig. 2.4 shows a few examples of the order parameter time-evolution as the system synchronises (or not).

The fastest formation is observed in the middle of the synchronised region

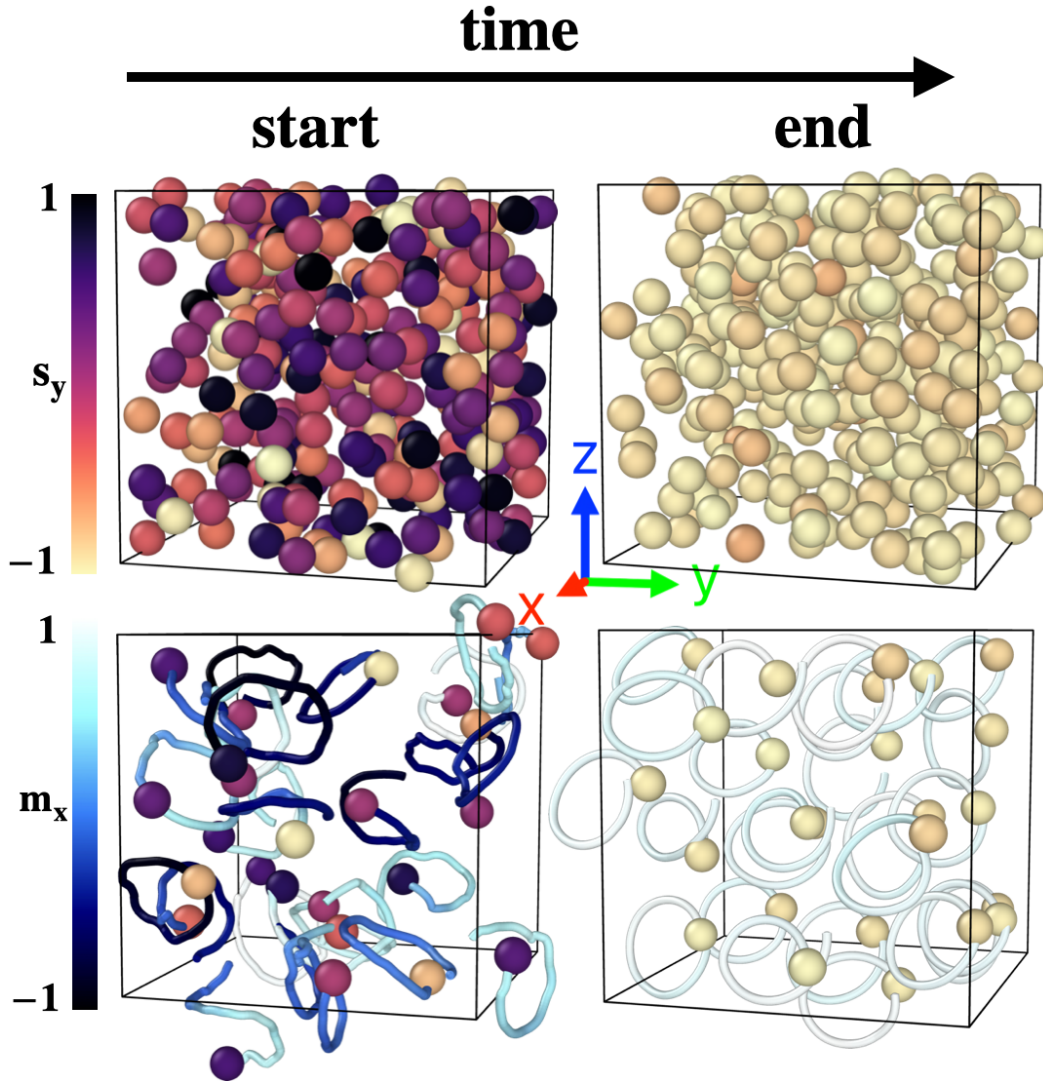


**Figure 2.3. Circular swimmer synchronisation example.** Snapshots of the system at the beginning (left) and end (right) of the simulation, composed of 286 particles corresponding to  $\phi \approx 0.15$  and  $r_t \approx 3.33a$ . 25 selected particles with their trajectories are shown on the bottom. The particles are coloured according to the  $y$ -component of their  $\mathbf{s}$  vector. The trajectories are shown over one period and coloured according to the  $x$ -component of the swimmer's  $\mathbf{m}$  vector.

(Fig. 2.1). For a given  $r_t$ , if  $\phi$  is too large no synchronisation is observed. This implies the existence of a dynamic bottleneck where the particles have multiple collisions during their full-rotation time  $T_0$ , hindering the growth of global alignment. This effect can be observed for some simulations towards the high- $\phi$  end of the synchronisation region, where the temporal evolution of the order parameters presents delay times before the transition to the synchronised state begins (see for example top-middle panel in Fig. 2.4).

Here,  $t_{sync}$  is increased (Fig. 2.1), and the order parameters fluctuate close to zero before the growth of the order begins. This effectively leads to the system presenting a hysteresis-type behaviour close to the high  $\phi$  limit of the synchronisation region. Fig. 2.5 shows the time evolution of the order parameters  $P_s$

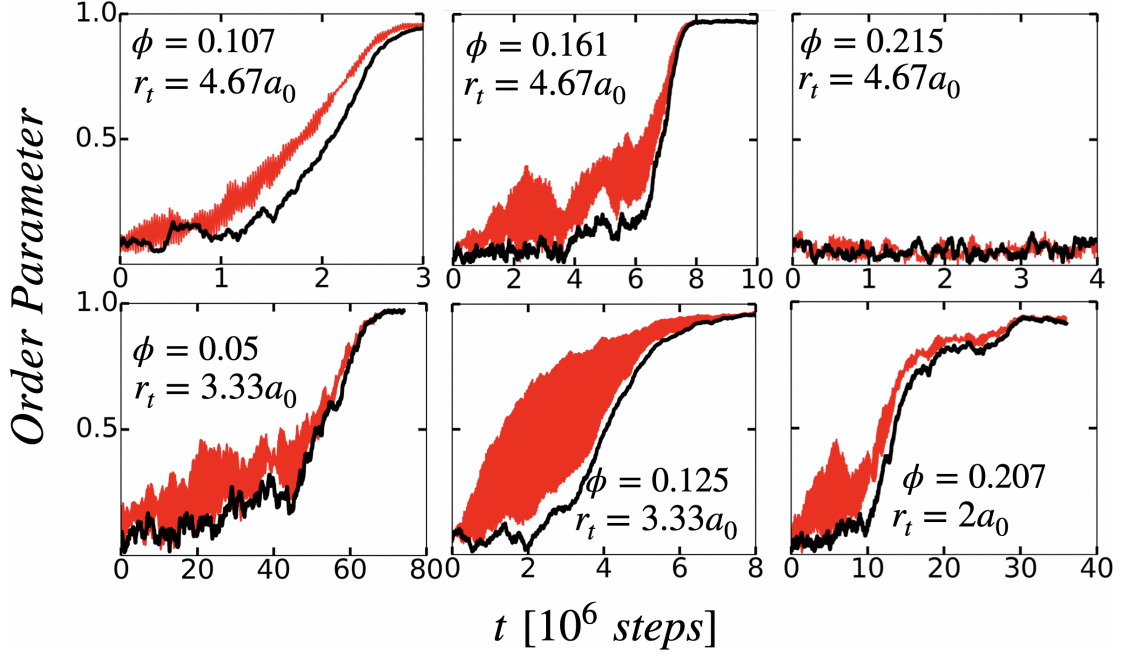


**Figure 2.4. Circular swimmer order parameter dynamics.** A few examples of the trajectories of the order parameters  $P_s$  (red) and  $P_m$  (black) leading to synchronisation (or not) for circular microswimmers.

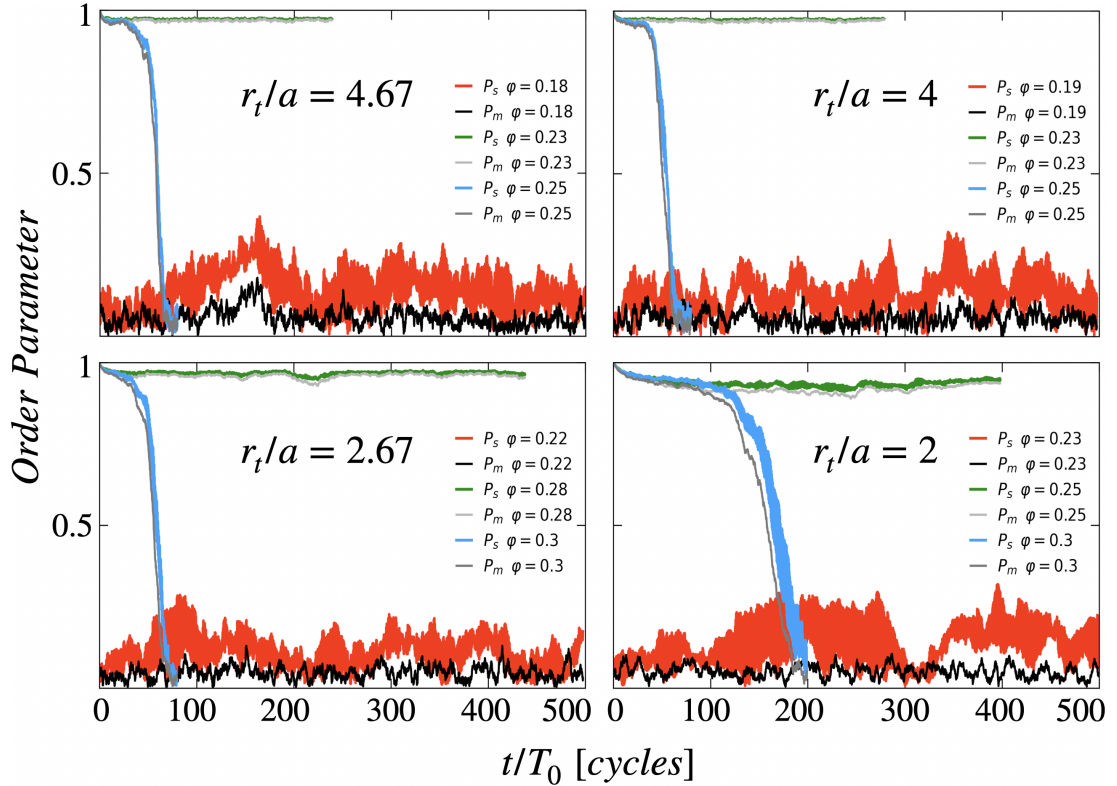


**Figure 2.5. Hysteresis in circular swimmer synchronisation.** Comparison between starting the simulations from an isotropic initial state (as used in the main text) and fully ordered states for different  $\phi$  at constant  $r_t$ . The system shows hysteresis-type behaviour within the simulation time, near the high density transition line.

and  $P_m$  after 500 cycles at the high- $\phi$  end of the synchronisation region. For simulations starting from an initial isotropic configuration, the order parameters fluctuate close to 0 (red and black), whereas at higher  $\phi$  order is maintained for simulations starting in an initially ordered configuration (green and light-grey). For even higher  $\phi$  the ordered state with a high ( $P_s/P_m \approx 1$ ) degree of alignment becomes unstable and the order parameters quickly drop to 0 with a steep gradient (blue and dark-grey). Further investigation is currently being carried out to determine the exact nature of the dynamic bottleneck and its dependence on the system parameters.

## 2.2 Circular microswimmer diffusive dynamics

Interestingly, the particle dynamics is reminiscent of the absorbing-active state transition predicted for dry active particles with circular trajectories in 2-dimensions (2D) [63]. Fig. 2.6 shows the dynamic phase diagram for the dry system presented in [63]. The system is composed of particles of diameter  $\sigma$  programmed to undergo circular trajectories of radius  $R$ . For low  $\phi$  and small  $R$  the system is found in the absorbing state. Here, the particles undergo their circular trajectories uninterrupted by collisions and therefore the mean squared displacement (MSD) develops a plateau at long times (blue curve in middle panel in Fig. 2.6). When  $\phi$  or  $R$  is increased, the collisions between particles increase. Beyond certain values of  $\phi$  and/or  $R$  the system is unable to find a non-interacting state and finds itself in the active state. Here, the MSD of the system grows proportionally with time (red curve in middle panel in Fig. 2.6) just as one would expect for a diffusive system.

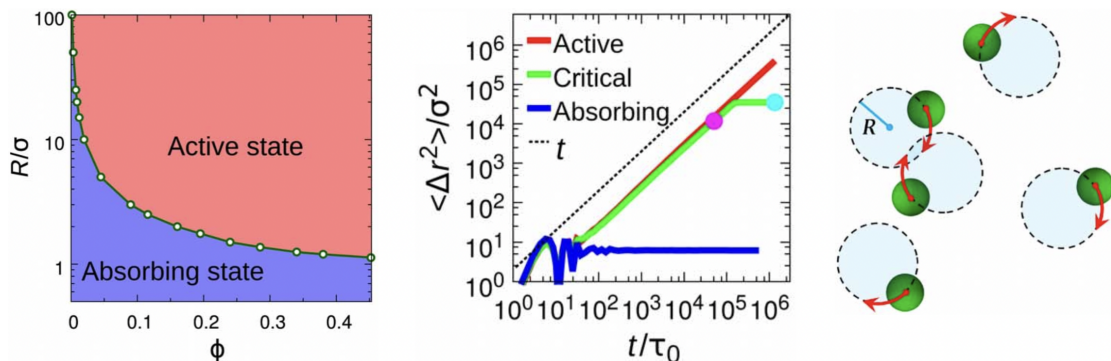


**Figure 2.6. Dynamic phase diagram and diffusive dynamics of a 2D dry system of chiral active particles with circular trajectories.** From [63]. The dynamic phase diagram for dry systems of chiral active particles of diameter  $\sigma$  that carry out circular trajectories of radius  $R$  independently (left). Mean square displacement (MSD) corresponding to the active, critical and absorbing states (middle). Schematic of the 2D circle active particles (right).

At the boundary between the absorbing and active states, the system is found in a critical state where it is initially active for some time, and then falls into the

absorbing state (green curve in middle panel in Fig. 2.6). For these cases, the system displays local synchronisation in the final absorbing state. Here, finite clusters can be found within which the particles have a similar orientation. At the beginning of the simulation when the system is in the active state, it is more homogeneous.

In our case however, working at small finite  $Re$ , we observe diffusion both after synchronisation and even at very low  $\phi$  due to the hydrodynamics. For the simulations found in the synchronisation region (coloured region of synchronisation diagram in Fig. 2.1), the diffusive dynamics in the early-time homogeneous isotropic state becomes sub-diffusive once the spontaneous synchronisation occurs. An example of this is shown in Fig. 2.7.

The synchronising state with  $\phi \approx 0.125$  and  $r_t \approx 4a$  (red curve in Fig. 2.7) is ballistic at the very beginning of the simulation for  $t < T_0$ , then becomes diffusive with  $MSD \sim t$ , and finally enters the synchronised state where  $MSD \sim t^a$  with  $a < 1$ . On the other hand, the non-synchronising active isotropic state at  $\phi \approx 0.188$  and  $r_t \approx 4a$  (blue curve in Fig. 2.7) remains diffusive with  $MSD \sim t$  throughout. In the 2D dry system, where the particles interact exclusively via steric collisions, only local synchronisation was observed [63]. This suggests that hydrodynamic interactions are crucial for the large scale synchronisation observed here.

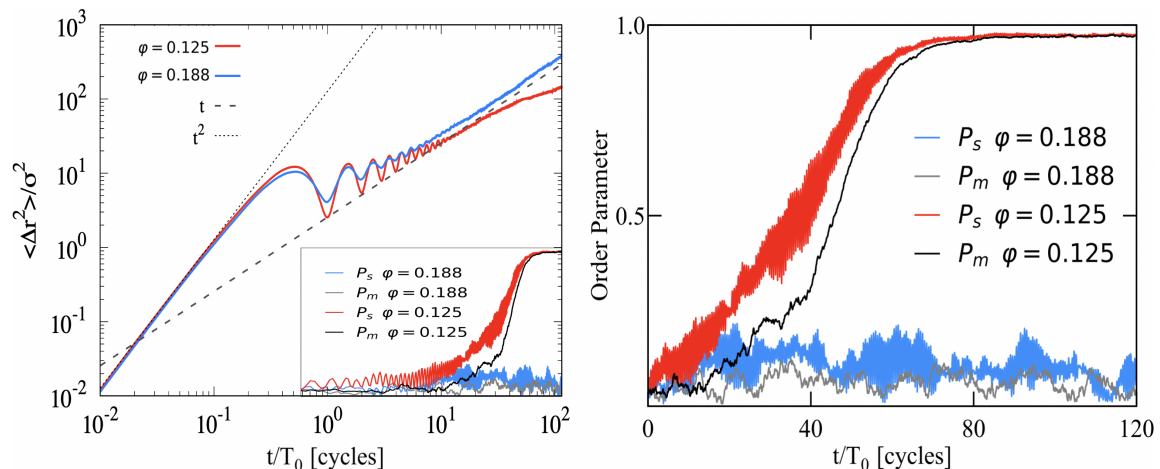


**Figure 2.7. Mean square displacement for circular swimmers in the active and synchronising states.** Left panel: The mean square displacement (MSD) for the the high density isotropic state (blue) and synchronising state (red) for circular swimmers with  $r_t \approx 4a$ . At short times, the ballistic regime corresponds to the the swimmers completing one cycle during their intrinsic period  $T_0$ . At long times, the active isotropic state shows diffusion  $MSD \sim t$  (blue), while at the synchronised state the dynamics becomes sub-diffusive  $MSD \sim t^\alpha$  with  $\alpha < 1$  (the red curve at long times). The inset shows the corresponding azimuthal  $P_s$  and polar  $P_m$  order parameters (in the same log-log scale). Right panel:  $P_s(t)$  and  $P_m(t)$  in linear scale.

Fig. 2.8 shows how the circular microswimmer diffusive dynamics depends on  $\phi$  and  $r_t$  by taking various cuts across the synchronisation diagram. Predictably, diffusion increases monotonically with both  $\phi$  and  $r_t$ . Just like in Fig. 2.7,

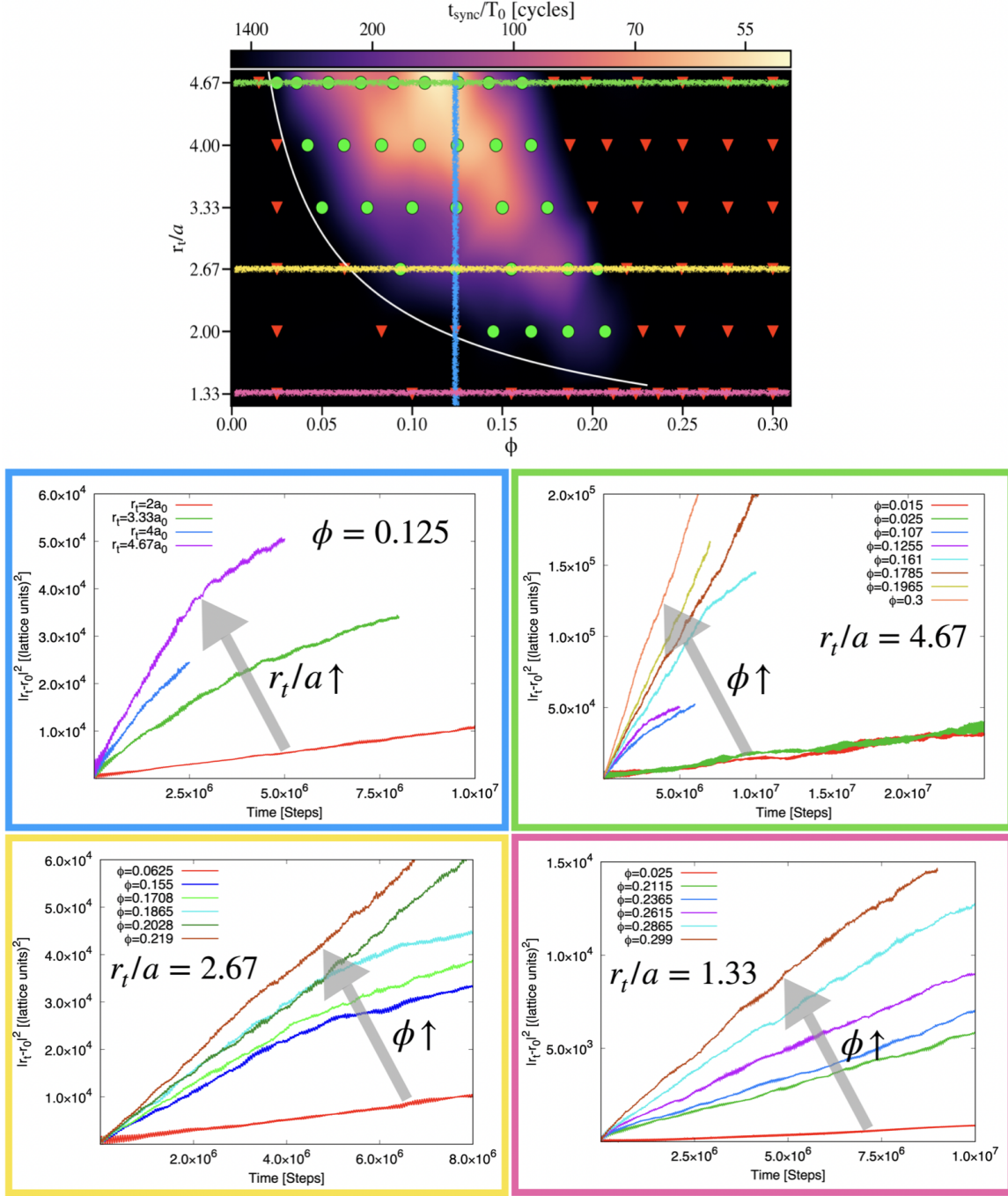


**Figure 2.8. Circular microswimmer diffusive dynamics.** Study of the mean square displacement (MSD) of circular microswimmers depends on the packing fraction  $\phi$  and the radius of trajectory  $r_t$ . The MSD is shown for points with  $\phi \approx 0.125$  and different  $r_t$  values (blue) and different values of  $\phi$  for  $r_t$  of 4.67 (green), 2.67 (yellow) and 1.33 (magenta).

the points in the synchronisation diagram ending in a globally synchronised state present bends or kinks in their respective MSD curves, corresponding to the sub-diffusive dynamics that indicate the onset of global synchronisation. When comparing our system to the 2D dry system studied by Lei et al. in [63], we could argue that the synchronisation region here would, in some way,

correspond to the critical line separating the absorbing and active states in the dry system (see and compare dynamic phase diagrams presented in Figs. 2.6 and 2.8). The presence of hydrodynamic interactions therefore allows for global synchronisation to be spontaneously achieved across a whole region between the absorbing and active regions in the dynamic phase diagram of active particles with circular trajectories that is unachievable for dry systems.

### 2.3 Random close packing argument for the onset of synchronisation in circular swimmer suspensions

Previous studies of linear squirmers predict that the alignment of source dipoles corresponding to the formation of uniaxial polar order is dominated by near-field hydrodynamic interactions [33, 34]. When  $r_t \sim a$ , an isolated swimmer sweeps an area  $\sim r_t^2$  during one period  $T_0$ , and can be thought to occupy an effective volume  $2\pi r_t^2 a$ . The lower- $\phi$  limit for the synchronisation region, closely corresponds to the random close packing of discotic cylinders with volume  $2\pi r_t^2 a$  (white line in Fig. 2.1). Above this line, the effective volumes overlap in the isotropic state, and the swimmers have a high probability of interacting via near-field hydrodynamics.

According to this argument, if the volume fraction  $\phi$  is below a given threshold value, the circular swimmers are far enough from each other so that the near-field hydrodynamic interactions are negligible, and there will be no aligning interaction between them to eventually lead to the synchronised state. For  $t > T_0$ , an isolated circular swimmer with a diameter  $\sigma$  encircles an area  $A = \pi r_t^2$  (in the plane perpendicular to the polar axis). Therefore, when  $r_t \sim \sigma$ , a circular swimmer can be thought to occupy an effective volume:  $v_{\text{eff}} \approx \pi r_t^2 \sigma$ , where  $\sigma = 2a$  is the diameter of the particle.

Consequently, we can expect the aligning interaction between two swimmers to arise when there is an overlap of their respective effective volumes  $v_{\text{eff}}$ . The validity of this argument can be tested by studying the random close packing  $\phi'_c$  of different oblate geometrical objects with a volume  $v'$  and an aspect ratio  $w = \sigma/(2r_t)$ . Fig. 2.9 shows the  $\phi$  curves, given by equations 2.3, corresponding to the *mapped*  $\phi'_c$  for systems with the same number density  $N/V$  and with particle volumes  $v'$ : Oblate ellipsoids [102, 103] (blue), oblate hard spherocylinders — OHSC [104] (yellow), discotic cylinders [105, 106] (orange), rectangular cuboids [107] (green) and spheres using random close packing of 64% [108–110] (purple). The lower boundary data for the synchronisation, is generally well fitted with disk-like objects  $w \sim \sigma/(2r_t) < 1$ , while spheres  $w = 1$  (purple) fail to do so.

The mapping for each curve appearing in the steady state diagram is given by:

$$\phi = \phi'_c \frac{v}{v'} \quad (2.3)$$

where  $v = 4/3\pi a^3$  is the actual volume a single spherical swimmer and  $\phi'_c$  is the

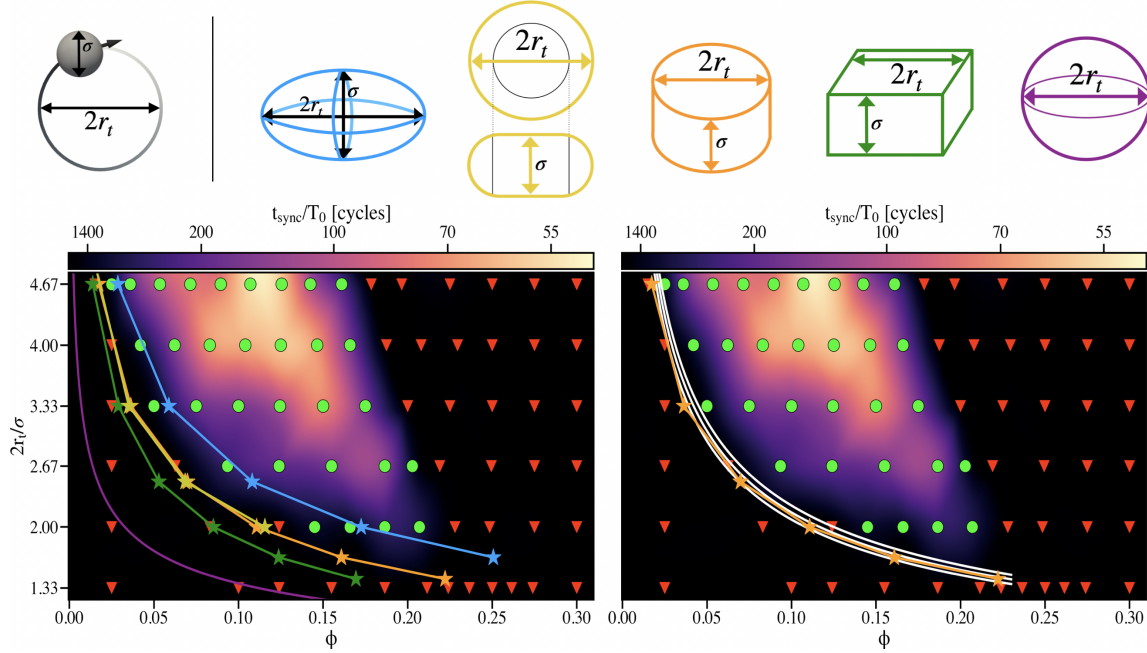


**Figure 2.9. Random close packing for circular swimmers.** The steady state diagram of the circular swimmers. Bottom left panel: mapped fits of different shapes (top panel) at their random close packing  $\phi'_c$  (according to eq.2.3). Oblate ellipsoids corresponding to the average values of ref [102, 103] (blue), oblate hard spherocylinders — OHSC ref. [104] (yellow), discotic cylinders ref. [105, 106] (orange), rectangular cuboids ref. [107] (green) and spheres ref. [108–110] (purple). All oblate shapes, with volumes  $v' \sim r_t^2 \sigma$  give a reasonable fit to the data, while spheres, with  $v' \sim r_t^3$ , do not. Bottom right panel: random close packing for discotic cylinders in orange just as before, according to ref. [105, 106], and assuming a constant  $\phi'_c$  (white) for:  $\phi'_c = 75\%$ ,  $70\%$  and  $65\%$ . We use  $\phi'_c = 70\%$  in the main text.

random close packing for the corresponding shape with a volume  $v'$  at the same number density.

In the synchronisation diagram presented in section 2.1 (Fig. 2.1) we fit the boundary using discotic cylinders ( $v' = \pi r_t^2 \sigma$ ) at  $\phi'_c = 70\%$ . The bottom right panel in Fig. 2.9 shows the data using the random close packing of discotic cylinders  $\phi'_c(w)$  (orange) from references [105, 106]. The three white curves use a constant  $\phi'_c = 65\%$ ,  $\phi'_c = 70\%$  and  $\phi'_c = 75\%$  from left to right, respectively.

Let it be noted that the above reasoning is only valid for circular swimmers with a reasonably small radius of curvature  $r_t \sim a$ . When  $r_t \gg a$  the trajectories could easily interpenetrate without affecting the particle dynamics.

## 2.4 De-synchronisation of circular microswimmers

In this final section of chapter 2, we focus on the region below the lower- $\phi$  limit of the synchronisation diagram (striped region below the white curve of synchronisation diagram presented in Fig. 2.10) in an attempt to discover whether or not dilute suspensions with the swimmers far apart from each other

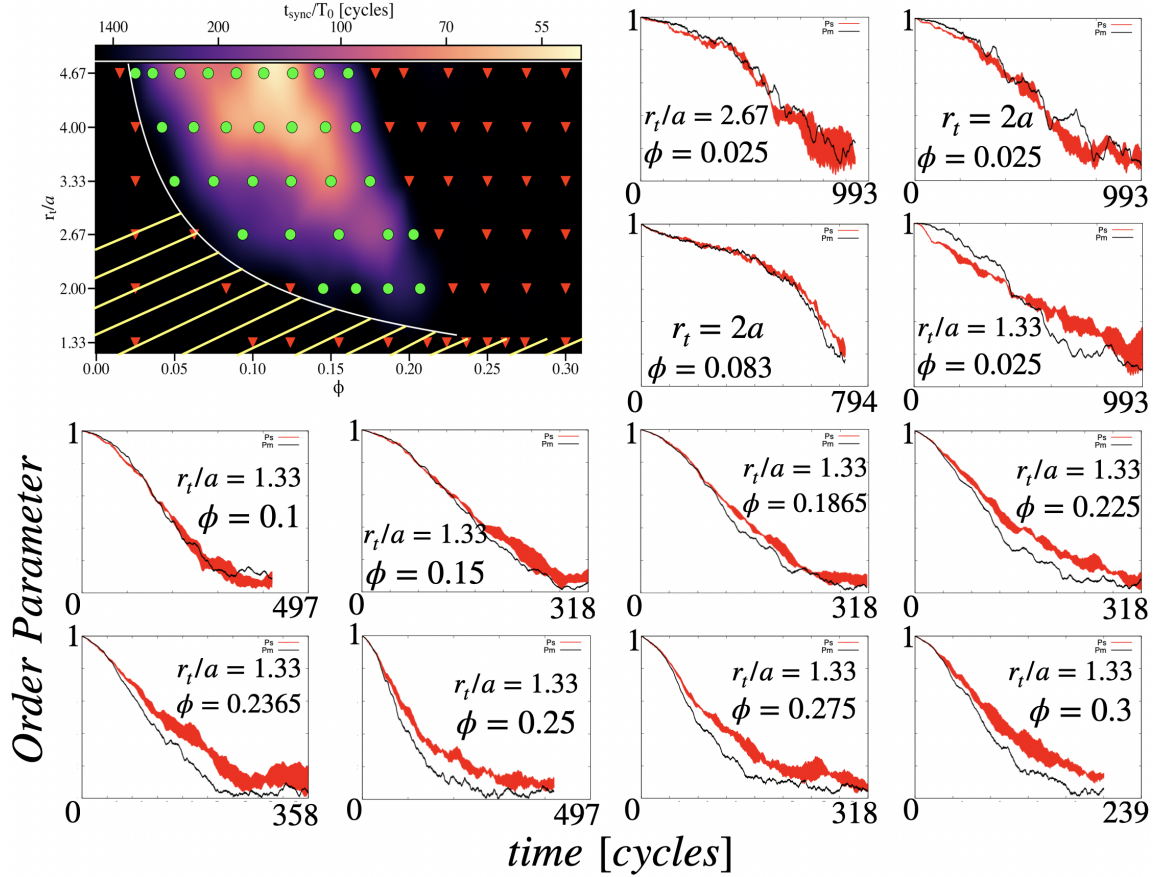


**Figure 2.10. De-synchronisation of circular microswimmers.** Examples of the time evolution of the order parameters  $P_s$  (red) and  $P_m$  (black) for points in the synchronisation diagram below the lower- $\phi$  limit of the synchronisation region.

are capable of synchronisation.

Earlier in the chapter we argued that synchronisation arises due to the near-field hydrodynamic interactions between particles that lead to an alignment between them at moderate packing fractions. Once the swimmers are far apart, these interactions are not present in the system and therefore if the system was ever to eventually synchronise, it would have to be attributed to the far field hydrodynamic interactions.

The far-field flow generated by a neutral squirmer [83] presents no vorticity and therefore is incapable of generating a torque on a point particle. On the other hand, a finite sized particle found in the far-field flow of another could experience a torque due to the difference in the flow field magnitude across its body. However, any torque produced this way would be significantly small and thus negligible, especially taking into account the fact that the far-field flow of a neutral squirmer decays as  $1/r^3$ . Nevertheless, we cannot rule out with certainty the possibility of the far-field flows of an ensemble composed of finite sized particles having a resulting aligning interaction at extremely long times well beyond  $t_{max}$ .

A good place to start to hopefully gain some insight regarding this problem, is to determine if these dilute systems are stable in the synchronised state.

Remarkably, we find that the orientational order in the system is in fact lost after long times. The results presented in Fig. 2.10 show how simulations that were initialised with the particles fully-aligned in the synchronised state ( $P_s / P_m / \approx 1$ ) and with random positions eventually end up in the isotropic state with  $P_s / P_m / \approx 0$ . Furthermore, for a given  $r_t$ , as the system becomes more dilute, the de-synchronisation takes longer. This result suggests that if anything, the far-field hydrodynamic interactions disorder the squirmers. This finding highlights the importance of the near-field hydrodynamic interactions even more, since in direct contrast to near-field hydrodynamic interactions, far-field hydrodynamic interactions appear to have a destructive contribution to synchronisation.

The reason why exactly the collective far-field interactions lead to disorder is unclear and needs to be investigated. As a first guess, we speculate that the far-field velocity fluctuations may play a role by slowing down and speeding up different squirmers at different times. Since the squirmers are intrinsically chiral, this effect would interfere negatively with the phase locking in the system and eventually lead to the loss of order.

.....

## 3 Helical swimmers

In this chapter we study suspensions of helical swimmers. Similarly to the preceding chapter concerning circular swimmers, we are mainly interested in the synchronisation of helical microswimmers. We therefore make use of the same order parameters defined in equations (3.1) and (2.2):  $P_v(t)$ ,  $P_s(t)$  and  $P_m(t)$  to quantify the amount of alignment in the system and track its temporal evolution.

Once more, we generate initial configurations with the squirmers homogeneously and randomly distributed in the simulation box in an isotropic state, with partial order, or in the completely ordered (synchronised) state. In this case, the simulations are typically run for a minimum time  $t_{max} = 60T_0$  ( $\sim 3 \times 10^6 \Delta t$  LB steps) for  $\phi > 10\%$ , and  $t_{max} = 1000T_0$  ( $\sim 50 \times 10^6 \Delta t$  LB steps) for  $\phi \leq 10\%$ .

### 3.1 Synchronisation of helical microswimmers

The helical swimmer trajectories are characterised by the ratio between the radius of curvature of the trajectory and the pitch length  $\lambda = r_t/p$  (Fig. 1.4). The particle motion is now 3-dimensional, leading to an increase of the probability of near-field interactions. Hence, synchronisation is observed at lower  $\phi$  than in the case of pure circular rotors. The synchronisation diagram for helical swimmers is shown in Fig. 3.1.

When comparing the synchronisation diagram for helical swimmers to that of circular swimmers (Fig. 2.1 and 3.1), we notice that the high- $\phi$  limit of the synchronisation region has been slightly shifted back towards lower  $\phi$ . This means that the dynamic bottleneck (discussed in section 2.1 of the previous chapter) occurs at more dilute systems for helical swimmers. This result is expectable since the squirmers now have a higher probability of meeting and interacting via the near-field hydrodynamics.

Another key difference between the two synchronisation diagrams which comes as a consequence of the swimmers now having 3-dimensional motion, is that synchronisation can now be achieved at very low packing fractions, well in the circular swimming dilute de-synchronisation region. The squirmers now actively explore space due to their swimming and eventually meet each other interacting directly rather than relying in just far-field interactions.

Additionally, the synchronisation region for helical swimmers extends down to values of  $r_t$  smaller than  $a$ . In our case, we observe synchronisation for values of  $r_t \approx 0.67a$  which correspond to  $\lambda = 0.03$  and  $\psi = 11^\circ$  (see Fig. 3.1). Whereas circular swimmers appear to be incapable of synchronising below  $r_t \approx 2$  (see

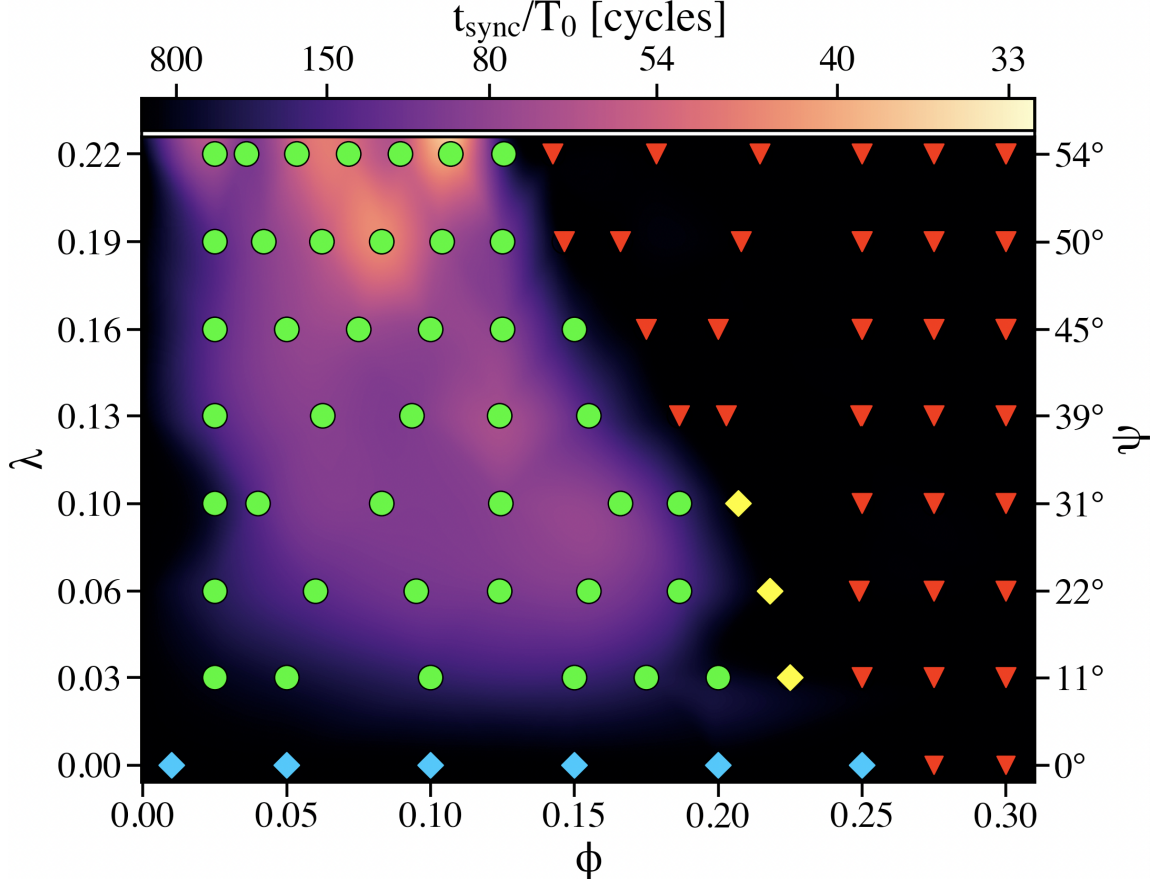


**Figure 3.1. Synchronisation diagram for helical swimmers.** Synchronisation state diagram for helical swimmers as a function of  $\phi$  and  $\lambda = r_t/p$  (or  $\psi = |\tan^{-1}(\tilde{B}_{11}/B_1)|$ ). The green circles correspond to global synchronisation, and red triangles to isotropic states. The blue diamonds mark polar order for classic linear neutral squirmers and yellow diamonds correspond to finite polar order in the absence of synchronisation for chiral swimmers. (data corresponds to  $p \approx 21a$ ). The synchronisation region is coloured according to a waiting time  $t_{sync}/T_0$  corresponding to the total time elapsed from the start of the simulation until synchronisation is reached.

Fig. 2.1).

When  $\lambda = 0$  ( $r_t = 0$  or  $\tilde{B}_{11} = 0$ ), the swimmers swim in a straight line with  $v_0 = 2/3B_1$  similar to classic neutral squirmers. In this case we are left with  $P_m$  as the only relevant order parameter accounting for the global polar order. In these cases, we observe the formation of pure polar order ( $P_m > 0$ ;  $P_s \sim 0$ ) (blue diamonds in Fig 3.1) in agreement with [31–37]. Remarkably, we also find cases with  $\lambda > 0$  with stable polar order in the absence of azimuthal ordering and hence synchronisation ( $P_m > 0$ ;  $P_s \approx 0$ ) (yellow diamonds in Fig. 3.1). These cases occur in the bottom half of the phase diagram right at the high- $\phi$  limit of the synchronisation region.

Just like with circular swimmers, a high degree of order is observed in the synchronised state. (Fig. 3.2a and b), and the particles swim along a common direction, with their helical trajectories aligned (Fig. 3.2c). Interestingly, when the ratio  $\tilde{B}_{11}/B_1$  is decreased, moving into regions of  $\lambda \lesssim 0.1$  and  $\psi \lesssim 31^\circ$ ,

the ordering dynamics is observed to change from a smooth growth for all three order parameters  $P_v(t)$ ,  $P_s(t)$  and  $P_m(t)$ , to a two-step process where the velocity alignment initially corresponds only to alignment in the polar direction, followed by a subsequent growth corresponding to alignment in the azimuthal direction (see *e.g.* Fig. 3.2a and b, for  $\lambda \approx 0.19$  and  $\lambda \approx 0.1$ , respectively).

The initially isotropic configuration of helical squirmers first spontaneously attains polar order, similar to classic neutral squirmer simulations. Then, once the polar flock has formed with the swimmers' helical trajectories aligned, they begin to synchronise their rotation aligning their velocities in the azimuthal direction as well. It is in this same region ( $\lambda \lesssim 0.1$  and  $\psi \lesssim 31^\circ$ ) where we observe the steady states with polar order and a lack of azimuthal order, as  $\phi$

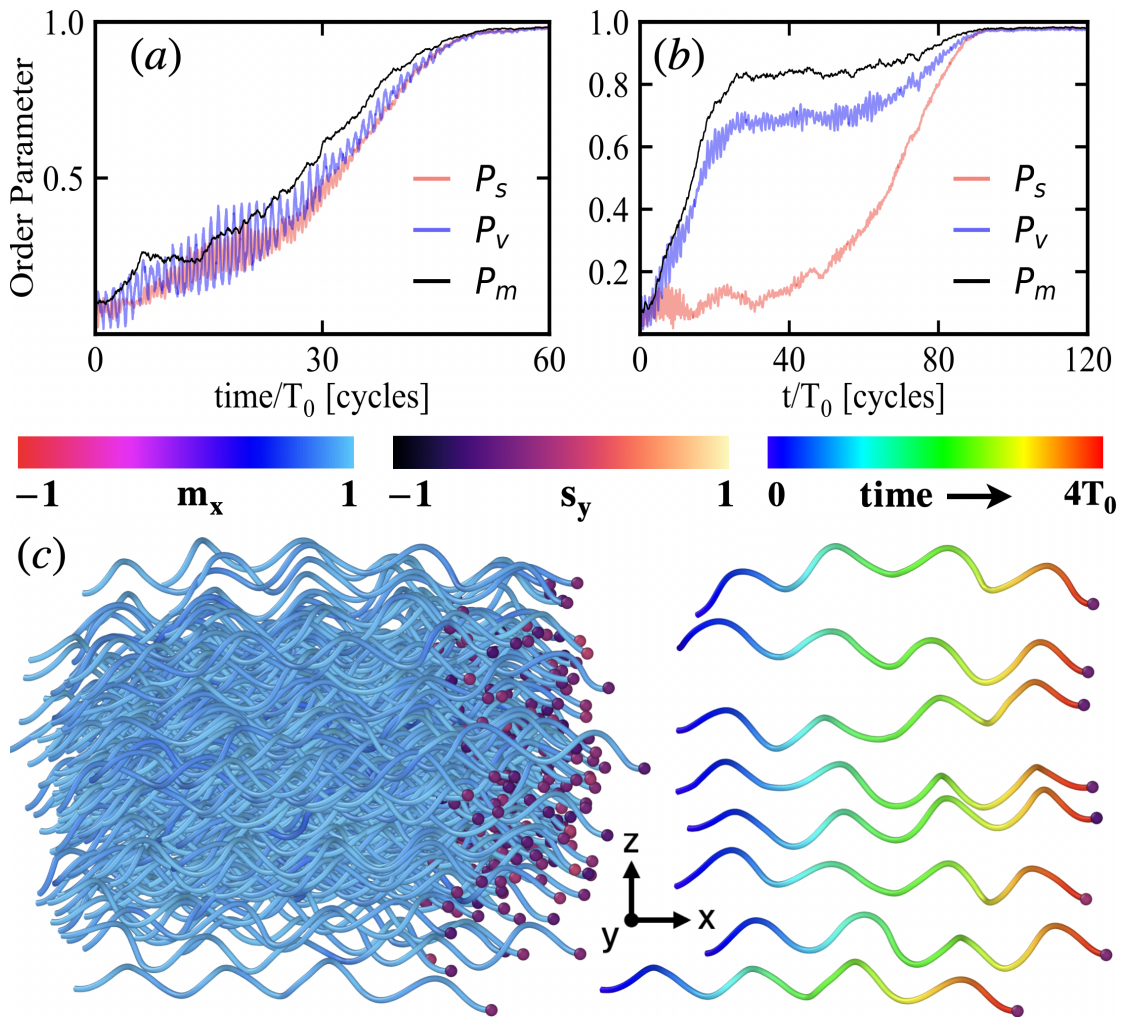


**Figure 3.2. Helical microswimmer ordering dynamics.** Time-evolution of the order parameters  $P_s$  (red),  $P_v$  (blue) and  $P_m$  (black) for (a)  $\phi \approx 0.083$ ,  $\lambda \approx 0.19$  and (b)  $\phi \approx 0.125$ ,  $\lambda \approx 0.1$ . (c) Snapshots of the system in the synchronised state with the swimmers homogeneously distributed in space. The unwrapped trajectories of all the  $N = 286$  helical swimmers over  $4T_0$  coloured according to  $m_x$  (left). 8 selected microswimmers with their trajectories coloured as a function of time (right). The particles are coloured according to  $s_y$ . (The snapshots in (c) correspond to  $\phi \approx 0.15$ ,  $\lambda \approx 0.16$ ).

is increased to the high- $\phi$  limit of the synchronisation region corresponding to the dynamic bottleneck.

These observations are perhaps easily understood when keeping in mind the linearity of the Stokes equation. If we break down the helical swimmer consisting of a source dipole  $\mathbf{B}$  rotating about its polar axis  $\mathbf{m}$  at an inclination  $\psi = |\tan^{-1}(\widetilde{B}_{11}/B_1)|$  (see section 1.4 of chapter 1) into the two modes  $B_1$  and  $\widetilde{B}_{11}$  used to build it (see Fig. 1.4), we end up having *two* source dipoles. One in the polar  $\mathbf{m}$  direction and the other in the azimuthal  $\mathbf{s}$  direction. Therefore, as we decrease the ratio  $\widetilde{B}_{11}/B_1$  moving to lower values of  $\lambda$  and  $\psi$ , towards the bottom of the phase diagram, we can expect the dynamics in the polar direction to be faster than those in the azimuthal one as a consequence of the linearity of the Stokes equation and the principle of superposition. As a result, while the system steady state may be the same across the synchronisation region, we have a certain degree of control over the path to it, with the linearity of the system making it easy for us to fine-tune the ordering dynamics of the microswimmer suspension.

Both the rotational frequency and the phase locking show comparable behaviour to the circular swimmers (see Fig. 3.3). Typical examples of frequency and phase locking for a system with  $N = 286$  at  $\phi = 0.15$  and  $r_t = 3.33$  are shown in Fig. 3.3a and b. In Fig. 3.4 we give a comparison of the two synchronisation diagrams for circular and helical swimmers.

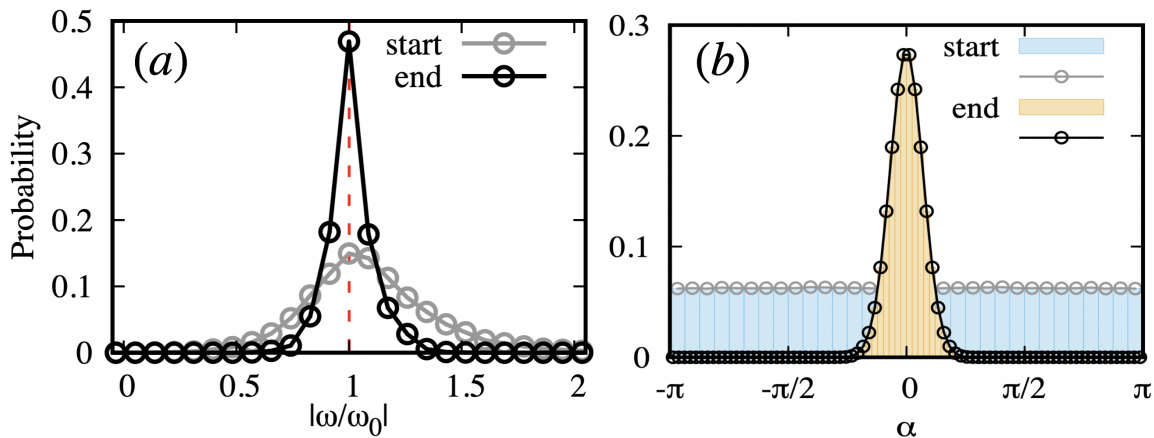


**Figure 3.3. Frequency and phase locking for helical microswimmers.** Probability distribution for  $N = 286$  helical swimmers corresponding to  $\phi \approx 0.15$ ,  $r_t \approx 3.33a$ ,  $\lambda \approx 0.16$  and  $\psi \approx 45^\circ$  of the (a) angular velocities  $\omega$  and (b) phase lag angle  $\alpha$  between all particle pairs, at the start and end of the simulation.

As mentioned earlier, the synchronisation spans to low chiralities, and is observed for  $\lambda \approx 0.03 \dots 0.22$  and  $\phi \approx 2.5 \dots 20\%$  (Fig. 3.1). The  $\lambda$  range corresponds to experimentally observed trajectories of biological swimmers such as  $\lambda = r_t/p \approx 0.05$  for *T. thermophila* [42] and  $\lambda \approx 0.15$  for the 3-dimensional swimming of sperm [43]. We note that the transition between synchronised chiral states and the linear-swimming polar state ( $\lambda = 0$ ) is predicted to occur between  $\lambda \lesssim 0.03$  and  $\lambda = 0$  (Fig. 3.1). This suggests that synchronisation may well be observable at lower chiralities than  $\lambda \approx 0.03$  considered in Fig. 3.1.

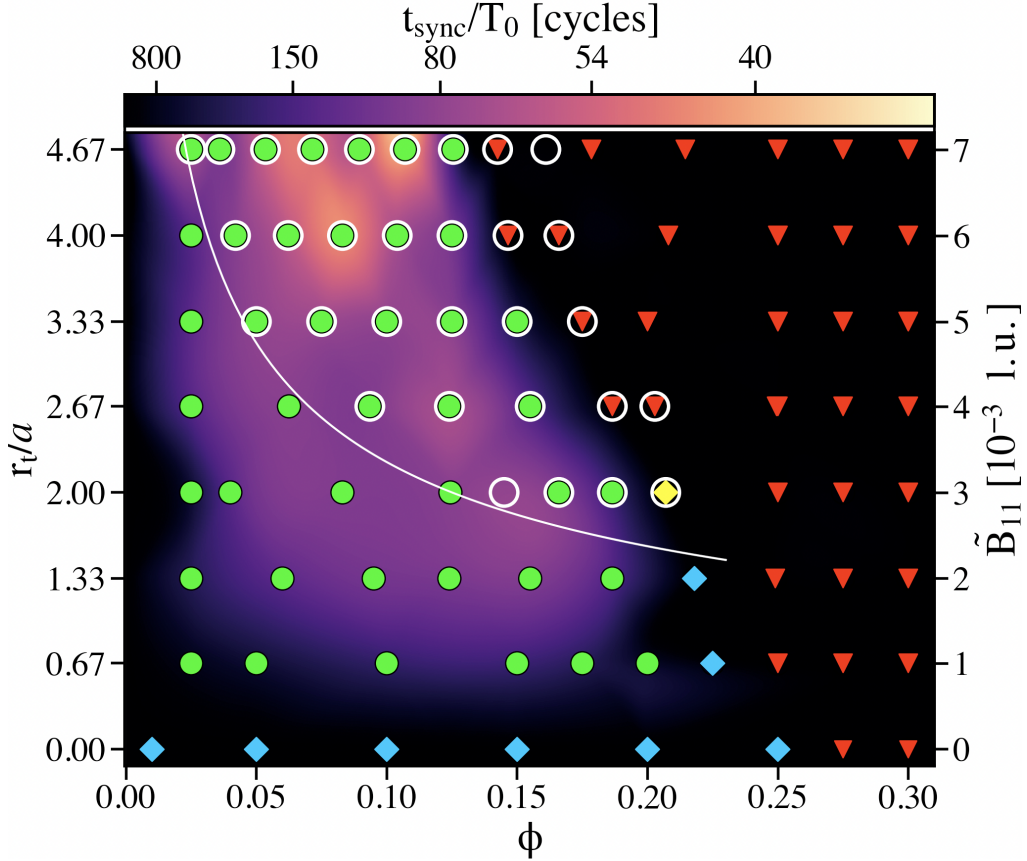


**Figure 3.4. Circular-helical microswimmer synchronisation state diagram comparison.** Synchronisation state diagram for helical swimmers as a function of  $\phi$  and  $r_t/a$ . The green circles correspond to global synchronisation, and red triangles to isotropic states. The blue/yellow diamonds mark polar order in the absence of azimuthal order above/below the  $\phi_c$  line for circular swimmers (see Fig. 2.1). The white circles mark the states for the same  $\phi$  and  $r_t$  leading to global synchronisation for circular swimmers.

A summary of the order parameter dynamics for helical swimmers is shown in Fig. 3.5. Here, we present the synchronisation diagram for helical swimmers as a function of  $r_t$ ,  $\tilde{B}_{11}$  and  $\phi$  (with  $B_1 = 0.005$ ). In this case, the shaded region is coloured according to  $\tau = 1/t_{sync}$ . Typical examples of the time-evolution profile of the  $P_m$  and  $P_s$  order parameters are shown for different points across the phase diagram. Similar to circle swimmers (Fig. 2.2), we observe a variety of dynamics for the order parameters, with this case presenting even more richness.

Starting with the synchronisation region, just as we discussed a moment ago, we notice a clear trend in the time-evolution of the order parameters where the separation (in time) of the growth between  $P_m$  and  $P_s$  increases as we move to smaller values of  $r_t$  (decreasing the ratio  $\tilde{B}_{11}/B_1$ ). In general, the synchronising region can be categorised into 3 groups (see Fig. 3.5): A nearly simultaneous growth of both  $P_m$  and  $P_s$  ( $\tilde{B}_{11}/B_1 \gtrsim 1$ );  $P_m$  leading the ordering dynamics ( $\tilde{B}_{11}/B_1 \approx 1$ ); and the two-step process where  $P_m$  grows and reaches a plateau before  $P_s$  begins to grow ( $\tilde{B}_{11}/B_1 \lesssim 1$ ). As already discussed, close to the high- $\phi$  limit of the synchronisation region  $P_m \neq 0$  and  $P_s \approx 0$  for the steady state

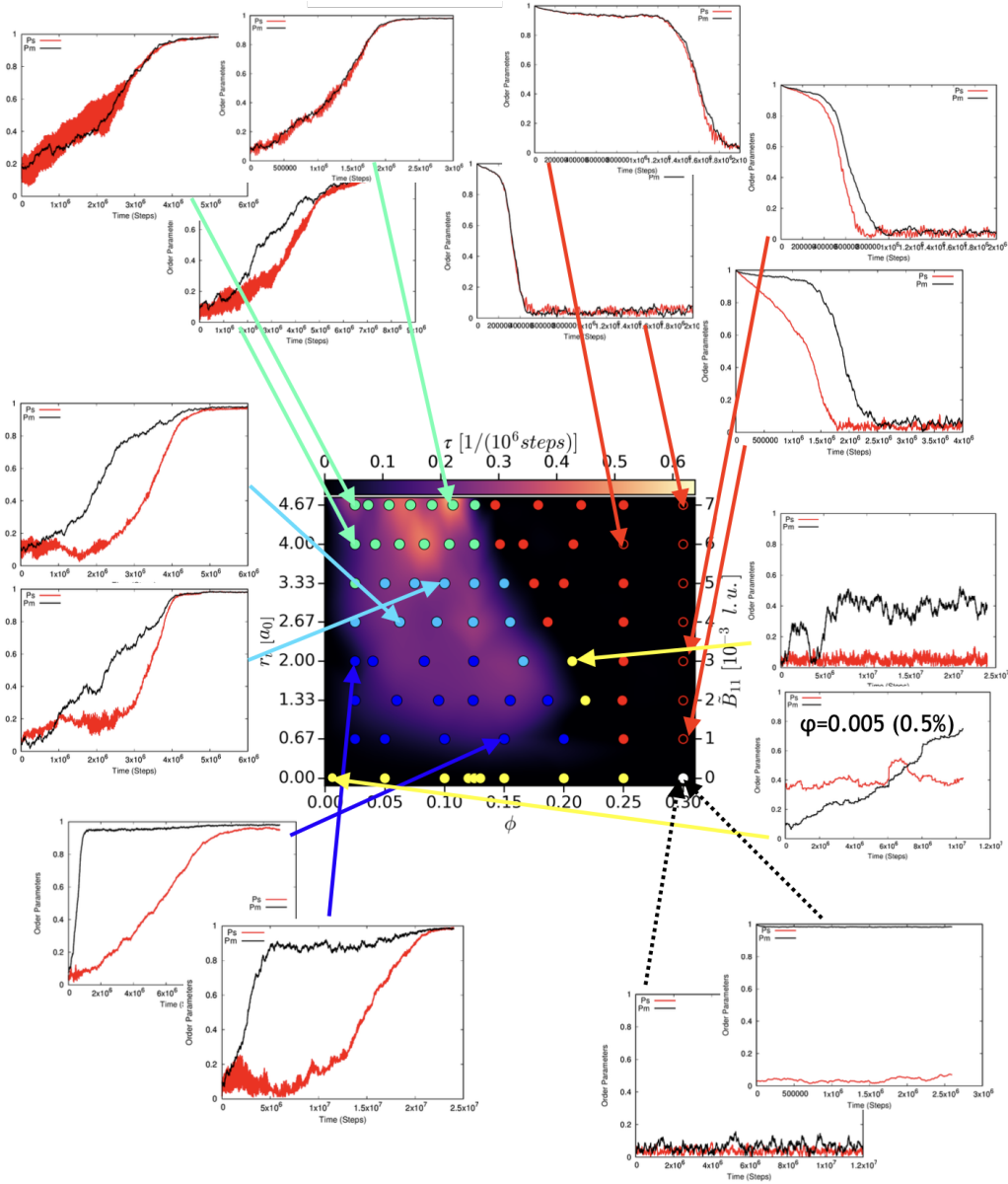


**Figure 3.5. Helical swimmer order parameter dynamics.** Synchronisation state diagram for helical swimmers as a function of  $\phi$  and  $r_t/a_0$  ( $a_0 \equiv a$ ). The synchronisation region is coloured according to the inverse of the waiting time  $\tau = 1/t_{sync}$  corresponding to the total time elapsed from the start of the simulation until synchronisation is reached (in lattice units). Examples of typical time-evolution trajectories for the order parameters  $P_m$  (black) and  $P_s$  (red) are shown corresponding to different points in the phase diagram. Circles in the synchronisation region mark simulations that end in global synchronisation with both  $P_m$  and  $P_s$  growing at the same time (mint),  $P_m$  leading the ordering dynamics (light blue), and the two-step process where  $P_m$  reaches a plateau before  $P_s$  begins to grow (blue). Red closed/open circles correspond to isotropic states that keep/lose their order when initialised in the fully-ordered state. Yellow circles mark states that correspond to finite polar order in the absence of synchronisation in the steady state. The white circle corresponds to an isotropic state for classic neutral squirmers that keeps its polar order when initialised in the ordered state.

(see order parameter time-evolution corresponding to  $r_t = 2$ ,  $\widetilde{B}_{11} = 0.003$  and  $\phi \approx 0.21$  Fig. 3.5).

Similar to circular swimmers, hysteresis also exists for helical swimmers. We see that the synchronised state is maintained well beyond the high- $\phi$  limit of the synchronisation region (closed red circles in Fig. 3.5). Eventually, at packing fractions above 0.25% the order is not maintained and the system ends up in the isotropic state with  $P_m/P_s \approx 0$  (open red circles in Fig. 3.5). For these cases ( $\phi > 0.25$ ), the higher the packing fraction the faster the loss of order to the isotropic state. Unsurprisingly, once again as the ratio  $\widetilde{B}_{11}/B_1$  is decreased,  $P_s$  presents a faster decay than  $P_m$  (see for example order parameter time-evolution corresponding to  $r_t \approx 0.67$ ,  $\widetilde{B}_{11} = 0.005 = 0.001$  and  $\phi \approx 0.3$  in Fig. 3.5).

At the bottom of the synchronisation state diagram, for  $r_t = 0$ , spontaneous polar order is observed for  $\phi$  up to 25%. For  $\phi = 0.3$  (white circle in bottom right corner of state diagram in Fig. 3.5), the system remains in the isotropic state unable to spontaneously align. When initialised in the aligned state, polar order is maintained with the system exhibiting hysteresis-like behaviour once again. Interestingly, we find that polar order can spontaneously emerge for packing fractions as low as 0.5% (see order parameter time-evolution corresponding to  $r_t = 0$ ,  $\widetilde{B}_{11} = 0$  and  $\phi \approx 0.005$  in Fig. 3.5). This is an important result since it sheds more light on the exact nature of the aligning mechanism in microswimmer suspensions. If we look closely at the order parameter curves, we notice kinks that lead to an abrupt increase or decrease in the value. This is additional proof that the particle aligning mechanism is due to near-field hydrodynamic interactions between particles coming into close proximity in a collision-like fashion.

## 3.2 Racemic mixture of helical microswimmers

Finally, to study the effect of frustration, we construct a racemic mixture composed of right-handed and left-handed helical swimmers by choosing  $C_1 = \pm 0.001$ . Fig. 3.6 shows the analysis for one such case where we start the simulation from a fully mixed isotropic state with particles from both right-handed and left-handed populations randomly distributed in space.

The  $P_m$  and  $P_s$  order parameter time-evolution (Fig. 3.6a) shows how the system spontaneously evolves from an isotropic state to a polar flock with  $P_m \approx 0.8$ . Agreeing with the predictions made for suspensions of linear neutral squirmers [31–37]. However, when compared to our results with homochiral suspensions of helical squirmers, we notice that there is a difference in the amount of order (alignment) in the steady state. For the homochiral case,  $P_m \approx 1$  (see Fig. 3.2a and b and synchronising states in Fig. 3.5). Whereas in our racemic mixture  $P_m \approx 0.8$ . This is due to the system experiencing a certain degree of frustration because of the oppositely-rotating populations. This effect is also reflected in the  $P_s$  curve (red curve in Fig. 3.6a), where huge oscillations are

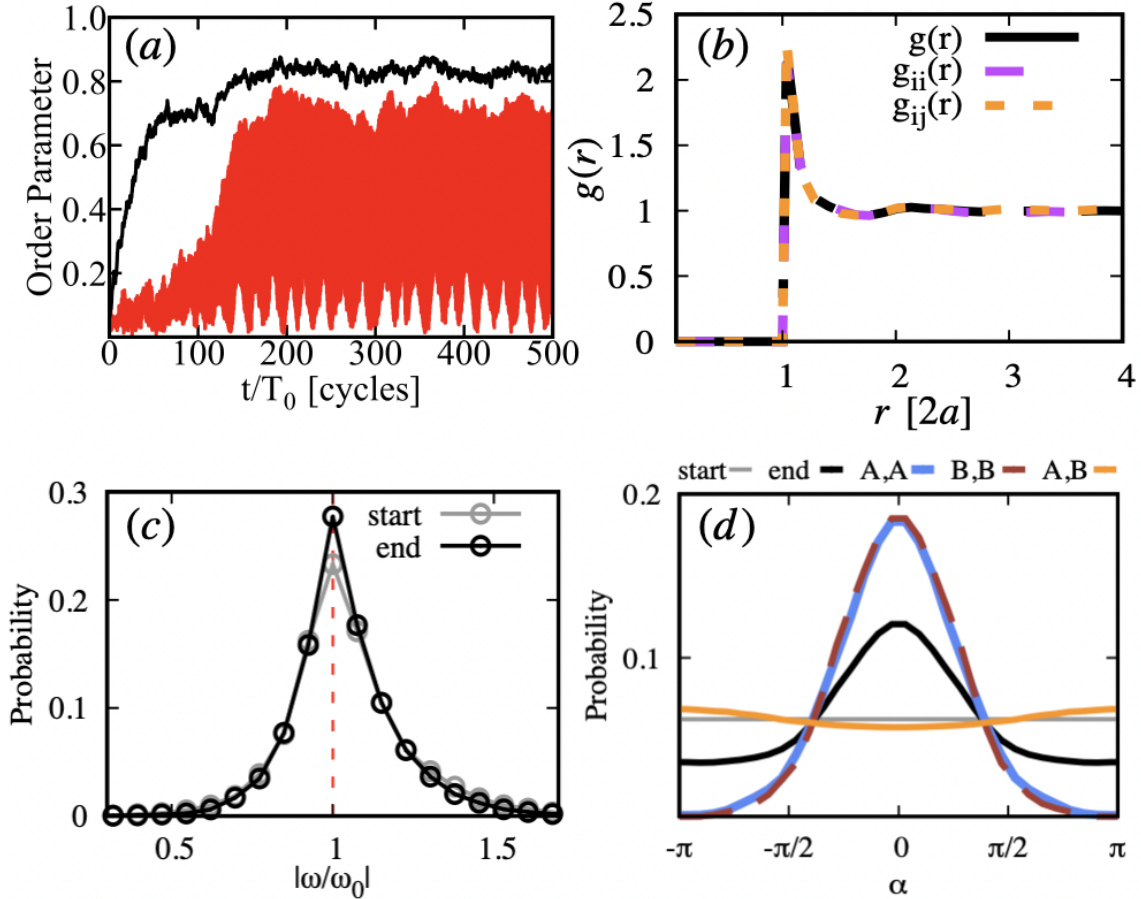


**Figure 3.6. Helical swimmer racemic mixture ordering dynamics.** Racemic mixture of helical swimmers at  $\phi \approx 0.1$  and  $\lambda \approx 0.16$ : Distributions of the (b) spinning frequency  $\omega$  and (c) the phase-angle difference  $\alpha$  calculated for all swimmer pairs (black), for clockwise (blue) and counter-clockwise (red) rotating populations, as well as for the cross population (orange). (d) Total (black), homochiral (violet) and heterochiral (orange) radial distribution functions.

observed spanning from 0 to 0.8 in the order parameter value. To understand exactly what is happening, we calculate the polar and azimuthal order parameters for *each* population. A detailed presentation of this analysis is given in Fig. 3.7. On a side note, the apparent long-time oscillation in  $P_s$  in Fig. 3.6a is just an artefact of the frequency of points chosen when plotting the curve and has no physical meaning behind it.

Fig. 3.7 shows simulation results corresponding to two cases of a racemic mixture of helical squirmers. Starting from a completely isotropic initial configuration with  $P_m \approx 0$ ,  $P_s \approx 0$ ; and starting in a configuration where the particles are completely ordered in the polar direction  $P_m = 1$ ,  $P_s \approx 0$ . In both cases, the particles are homogeneously distributed in space.

The population order parameters now clearly show how each population of rotating squirmers (left-handed and right-handed) is synchronised. This now explains the large fluctuations of  $P_s$ . Since both populations display a high degree of order within themselves and they both swim in roughly the same

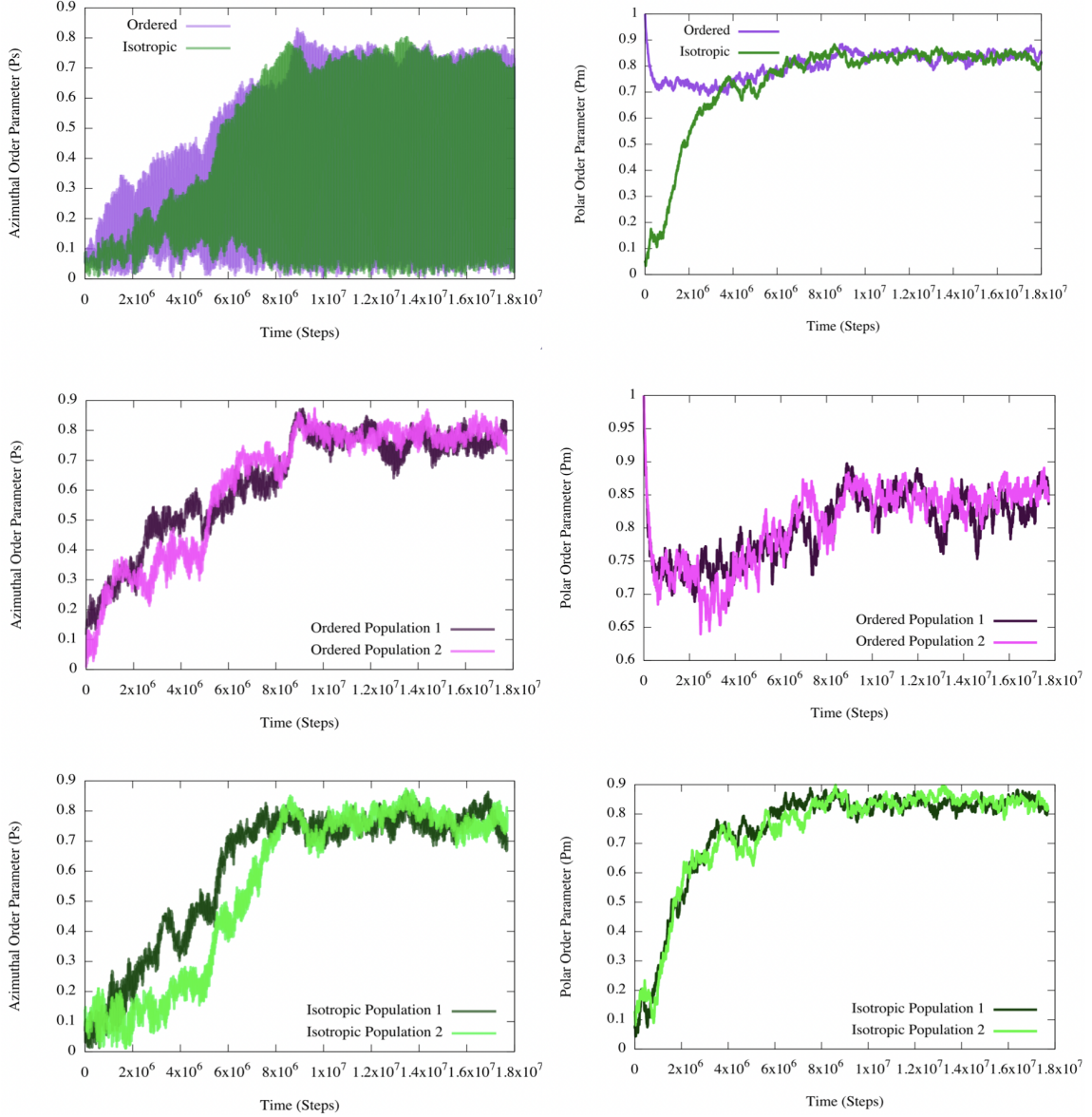


**Figure 3.7. Helical swimmer racemic mixture order parameter analysis.** Azimuthal  $P_s$  (left) and polar  $P_m$  (right) order parameters for a racemic mixture of helical microswimmers at  $\phi \approx 0.1$  and  $\lambda \approx 0.16$  starting in an isotropic initial configuration (green) with  $P_m \approx 0$ ,  $P_s \approx 0$ , and polar-ordered initial configuration (violet) with  $P_m = 1$ ,  $P_s \approx 0$ . Top row: global order parameters. Middle row: Population order parameters for the ordered initial configuration. Bottom row: population order parameters for the isotropic initial configuration.

direction, the azimuthal unit vectors  $\mathbf{s}$  will almost completely align or cancel out twice per period  $T_0$ , leading to the large fluctuations in  $P_s$  with period  $T_0/2$ . Within the time-scale of the simulations, we observe no spatial separation of the swimmers whatsoever — the fluid-like pair-correlation function calculated within species and cross-species matches with the  $g(r)$  of the whole system (Fig. 3.6b). Remarkably, the system remains homogeneously mixed consisting of two synchronised, interpenetrating fluids.

At the steady state, the particles, on average, swim along a common direction

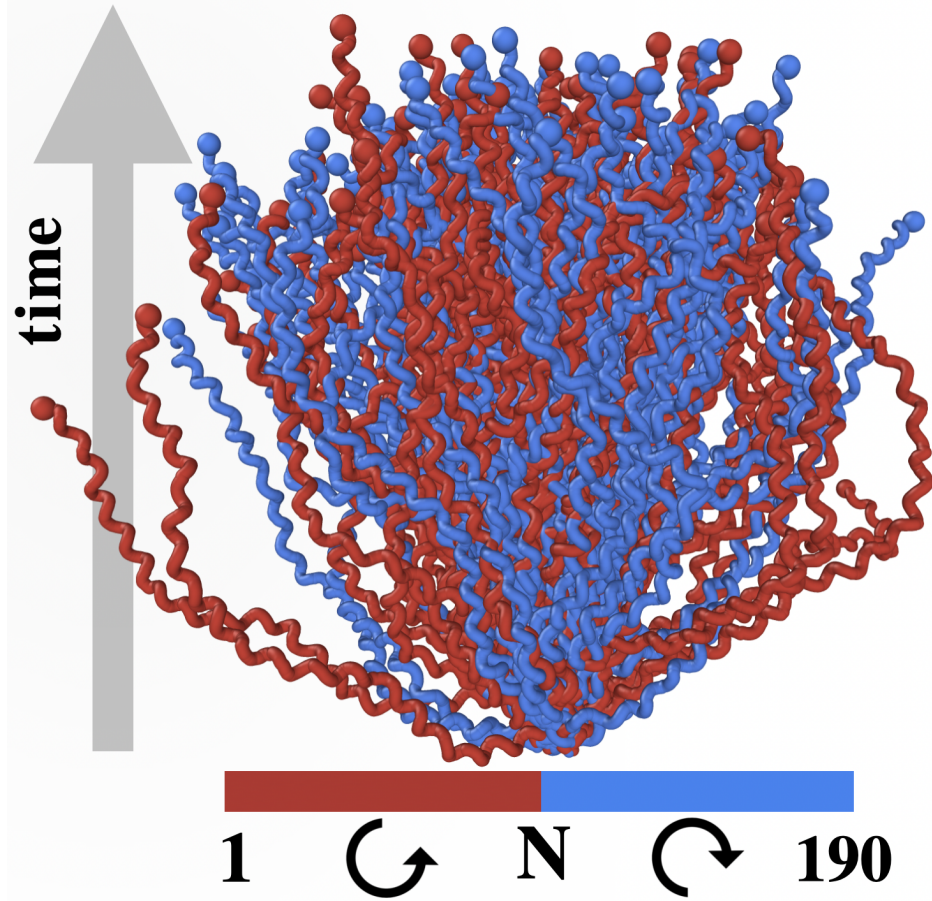


**Figure 3.8. Helical swimmer racemic mixture snapshot.** Snapshot of the helical swimmer racemic mixture at  $\phi \approx 0.1$  and  $\lambda \approx 0.16$  with unwrapped trajectories at the steady state after  $20T_0$ . The system is composed of  $N = 190$  squirmers. 95 with right-handed rotation (red) and 95 with left-handed rotation (blue).

and the rotational frequency  $\omega$  distribution is observed to peak at  $\omega_0$  (Fig. 3.6c). The frustration in the system can be perceived again when comparing the pre- and post-steady state distributions of the angular velocities for this case to those of the homochiral case (compare Fig. 3.6c to Fig. 3.3a). Here the distribution in the final steady state is almost the same as that in the initial isotropic state whereas for the homochiral case, the distribution in the steady state has a much more pronounced shape with the peak (at  $\omega \approx \omega_0$ ) more than twice the height of the initial distribution's peak.

Similarly, at the steady state the phase-lag angle  $\alpha$  distribution is wider compared to that of the homochiral system (compare black curve in Fig. 3.6d to Fig. 3.3b). However, the intra-species  $\alpha$  shows strong phase-locking (blue and red curves in Fig. 3.6d), whereas for the cross-species no significant peak is observed (orange curve Fig. 3.6b). This implies that we have two oppositely spinning populations in the system. This way, each population can present a relatively high degree of alignment within itself while the total alignment in the system is less pronounced. Upon closer inspection, the cross-species phase-lag angle distribution shows a slight preference for  $\alpha = \pm\pi$ , which corresponds to

a parallel orientation of the in-plane projections of the source dipoles (orange curve in Fig. 3.6d). For  $\alpha = \pm\pi$ , the in plane source dipole velocities are aligned, corresponding to a polar state in the plane perpendicular to the rotational (polar) axis given by the polar director  $\mathbf{P}_M$ . (see Fig. 3.9). This means that as the two populations swim roughly in the direction of  $\mathbf{P}_M$  while rotating in opposite directions, they spend slightly more time, on average, in the configuration where their in-plane velocities are aligned in parallel rather than unaligned and anti-parallel to each other. Once again this highlights the importance of the near-field interactions and more generally, the importance of hydrodynamics.

This result is effectively a manifestation of the linearity of the Stokes equations, agreeing with the aforementioned observations of the spontaneous formation of polar order in suspensions of classic neutral squirmers [31–37]. In dry models, we could expect the opposite effect — particles spending more time together when their velocities are in the anti-parallel configuration as a result of head-to-head collisions. This could lead to density variations (inhomogeneities) in the system and perhaps even clustering under certain circumstances. Hydrodynamic interactions therefore would appear to suppress density variations, allowing the system of left-handed and right-handed helical swimmers to remain in a homogeneous phase despite the relatively high degree of frustration.

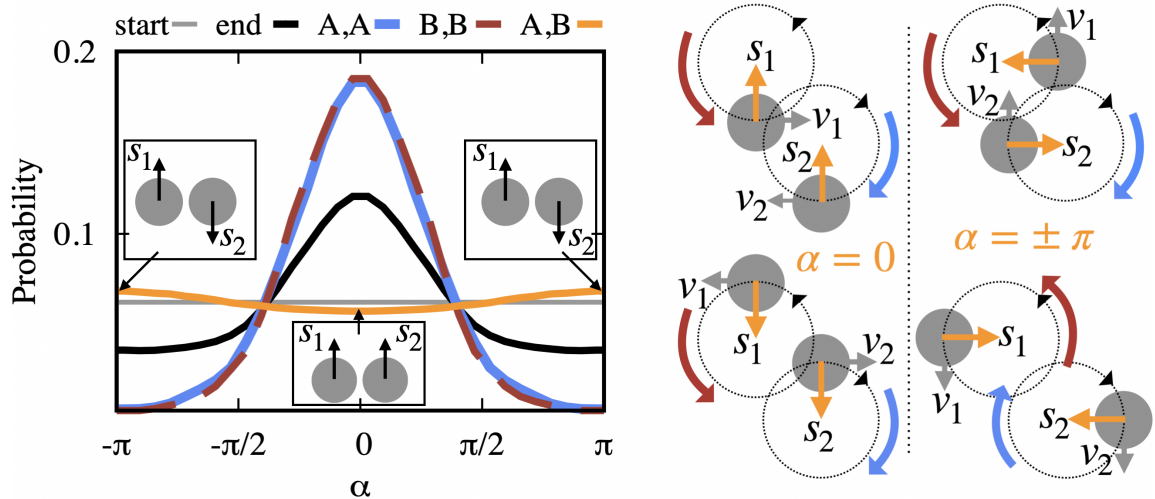


**Figure 3.9. Racemic mixture cross-population phase-lag analysis.** Schematic showing the parallel ( $\alpha = 0$ ) and anti-parallel ( $\alpha = \pm\pi$ ) configurations of a pair of rotors with opposite chirality in the plane perpendicular to the average global polar director  $\mathbf{P}_M$ . When the lag-angle  $\alpha = 0$ , the in-plane velocities  $\mathbf{v}_1$  and  $\mathbf{v}_2$  (given by the gray arrows) are antiparallel. For  $\alpha = \pm\pi$  the velocities are aligned, corresponding to a polar state in the plane perpendicular to the rotational (polar) axis. The arrows  $\mathbf{s}_1$  and  $\mathbf{s}_2$  mark the direction of the assigned azimuthal directors. The polar directors  $\mathbf{m}_1$  and  $\mathbf{m}_2$  are perpendicular to the plane shown.

### 3.3 Comparison to racemic mixture of circular microswimmers

Finally, for comparison, we attempt to create a racemic mixture of circular swimmers. For helical swimmers, this corresponds to the case where  $\lambda = \infty$  of  $\psi = 90^\circ$ . We use  $N = 190$  circular squirmers at  $\phi \approx 0.1$  and  $r_t \approx 0.33$  with  $\overline{B}_{11} = 0.005$  and  $C_1 = \pm 0.001$ .

Fig. 3.10 shows the order parameter analysis similar to that carried out in Fig. 3.7 for racemic mixtures of helical squirmers. Here, we show the time-evolution of the order parameters for the whole system  $P_m$  and  $P_s$ ; and the time-evolution of the order parameters for the two oppositely-spinning populations  $P_m^1, P_m^2, P_s^1$  and  $P_s^2$ . The system is initialised with the particles randomly and homogeneously distributed in space with polar order  $P_m = 1$  and no azimuthal order  $P_s \approx 0$ .

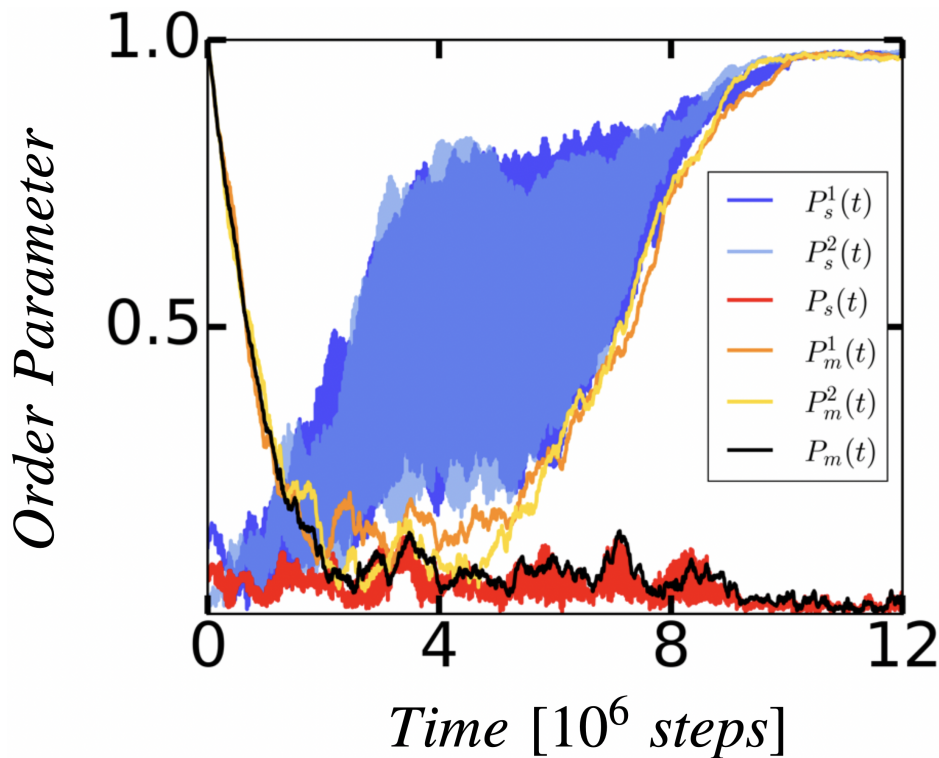


**Figure 3.10. Circular swimmer racemic mixture order parameter analysis.** Time-evolution of the azimuthal  $P_s$  (red) and polar  $P_m$  (black) order parameters of the racemic mixture of circular microswimmers system at  $\phi \approx 0.1$  and  $r_t \approx 0.33$ . The population azimuthal and polar order parameters are given by  $P_s^1$  (blue),  $P_s^2$  (light-blue),  $P_m^1$  (orange) and  $P_m^2$  (yellow).

The results show how in the final, steady state both  $P_m \approx 0$  and  $P_s \approx 0$  with small fluctuations. When looking at the population order parameters, we see that there is a very high degree of order in the system just like with homochiral systems:  $P_m^1 \approx P_m^2 \approx P_s^1 \approx P_s^2 \approx 1$ . Each population is in the fully synchronised state, and in fact, the whole system is fully synchronised

with the two populations being indistinguishable (as far as practical purposes are concerned) with all the particles now rotating in the same direction.

As already mentioned, the system is initialised with all the particle polar axes  $\mathbf{m}$  aligned in the same direction. Half the squirmers rotate clockwise and the other half rotate counter-clockwise. Just like in the case of the racemic mixture of helical swimmers, this creates a certain degree of frustration with oppositely-spinning neutral squirmers “wanting” to align their velocities. In contrast to helical swimmers, there is nothing stopping the squirmers from reorienting over time in such a way as to always swim in the same direction, similar to the case of the emergence of polar order in linear neutral swimmer suspensions [31–37]. Therefore, the swimmers simply align their velocities over time with all of them swimming in the same direction at the end (just like in the homochiral situations of circular swimmers studied in chapter 2). This is equivalent to flipping one of the populations’ global polar director by  $180^\circ$  from the start to the end of the simulation (see Fig. 3.11). When this happens, half the squirmers have their polar unit vector  $\mathbf{m}$  in the opposite direction of those in the other population (that hasn’t flipped). The same happens with the azimuthal unit vectors  $\mathbf{s}$ . Hence,  $P_m \approx 0$  and  $P_s \approx 0$  in the steady state. Interestingly, during the re-ordering process, both the population polar order parameters  $P_m^1$  and  $P_m^2$  are decreased to values of almost 0 while the population azimuthal order parameters  $P_s^1$  and  $P_s^2$  begin to grow. Basically, the system completely loses its

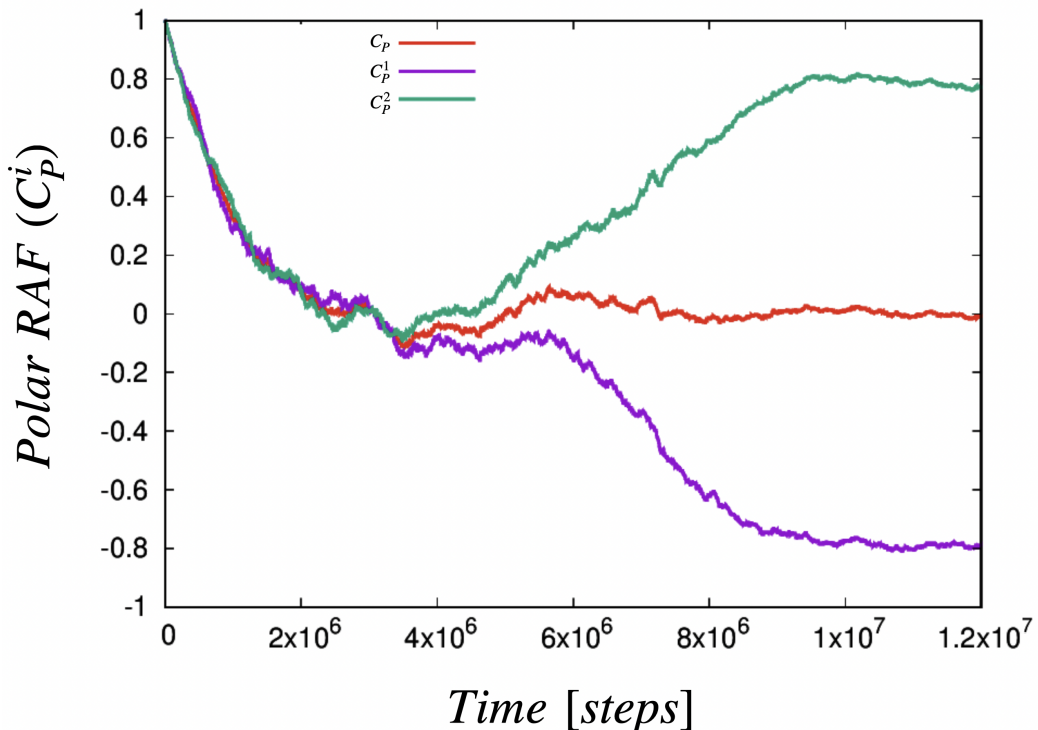


**Figure 3.11. Polar rotational autocorrelation function for a racemic mixture of circular microswimmers.** Time-evolution of the polar rotational autocorrelation function  $C_P^i(t)$  for the whole system (red) and for each of the two populations  $C_P^1(t)$  (purple),  $C_P^2(t)$  (green) for a racemic mixture of circle swimmers.

partial order (polar order) entering a fully isotropic state and then builds the order back up again to reach the fully synchronised state. This is a manifestation of spontaneous symmetry breaking.

The large fluctuations during the growth of  $P_s^1$  and  $P_s^2$  are an indication of the fact that particles from different populations begin to align between themselves, highlighting the fact that the system is indeed homochiral and we are merely tagging the particles with our definitions of  $\mathbf{m}$  and  $\mathbf{s}$ . The same is not true for helical swimmers however, since in this case the symmetry is explicitly broken by the presence of the  $B_1$  term; allowing us to construct frustrated states composed of two separately-synchronised, mixed, chiral fluids.

In Fig. 3.11 we show the time-evolution of the polar rotational autocorrelation function  $C_P^i$  of the system  $C_P$  and both populations  $C_P^1$  and  $C_P^2$  over time:

$$C_P^i(t) = \langle \mathbf{m}_j^i(0) \cdot \mathbf{m}_j^i(t) \rangle_N \quad (3.1)$$

where  $\mathbf{m}_j(0)$  is the  $j$ th squirmer's  $\mathbf{m}$  at in the initial configuration  $t = 0$  and  $\mathbf{m}_j(t)$  is the  $j$ th squirmer's  $\mathbf{m}$  at time  $t$ .

The curves in Fig. 3.11 clearly show how one population has almost flipped its  $\mathbf{m}$  vectors from the beginning of the simulation to the end while the other has almost returned in the same orientation. (Obviously, it is not necessary for the system to re-orient in exactly the same direction in space and therefore we do not expect  $C_P^1/C_P^2 \approx 1/-1$  or vice versa).



## 4 Post-synchronisation collective phenomena

In this final chapter, we present preliminary results concerning findings we have come across in the case of circular microswimmers, after the system has reached the fully-synchronised state. Notably, we observe post-synchronisation phase separation and wave propagation of local polarisation. Since we are still trying to understand these observations, we limit ourselves to showcasing the results and the initial analysis carried out so far in an attempt to understand the underlying phenomena while sharing our current hypotheses.

### 4.1 Post-synchronisation phase separation in circular microswimmer suspensions

In chapter 2 we showed how circular swimmers of radius  $a = 8$  (lattice units) can spontaneously synchronise their swimming and reach a globally aligned state. In the synchronised state, all the particles rotate with their angular velocities aligned and present a high degree of phase-locking whilst maintaining a homogeneous, liquid-like structure. The spontaneous emergence of global synchronisation is observed for packing fractions and radii of trajectory of  $\phi \approx 3 \dots 23\%$  and  $r_t \approx 2 \dots 5a$  respectively.

For most of the simulations, once the system has reached the synchronised state, it remains there for the rest of the simulation time. Once the synchronised state has been reached in a time  $t_{sync}$  (see Fig. 2.1), our protocol involves extending the simulations for an additional time of  $t_{sync}$ . This way, we deem the state stable if the system remains in the synchronised state with no further changes in its dynamics.

For some cases however this is not the case. For certain simulations, a high degree of alignment is maintained, but the system phase separates into a dense, particle-laden region and a dilute region with very few particles in it (see Fig. 4.1). The simulations where this occurs are found at the centre of the synchronisation region, corresponding to the fastest synchronisation times  $t_{sync}$ .

In Fig. 4.1 we show the synchronisation state diagram presented in section 2.1 of chapter 2 (Fig. 2.1) with the preliminary, phase-separating region marked out by a black dashed line. To the right of the state diagram we show a snapshot of a typical configuration corresponding to a post-synchronisation, phase-separated system corresponding to a simulation with  $\phi \approx 0.11$  and  $r_t \approx 4.67a$ .

Our initial guess as to what could be causing the onset of post-synchronisation phase separation, is the single particle Reynolds number, which we will refer to

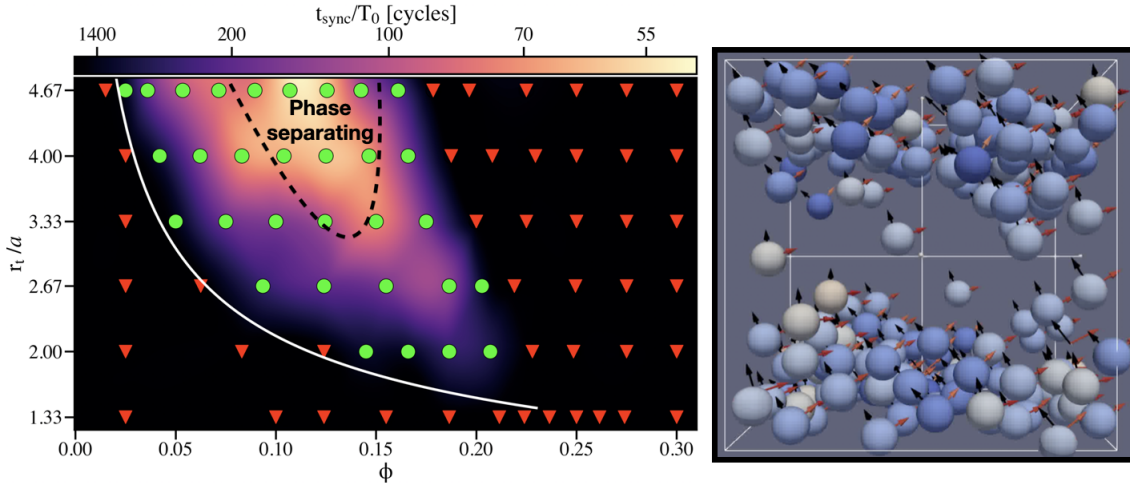


**Figure 4.1. Phase separation for circular swimmers.** The synchronisation diagram for circular swimmers presented in chapter 2 (Fig. 2.1) with the phase separating region in the middle of the synchronisation region (left). A snapshot of the system at  $\phi \approx 0.11$  and  $r_t \approx 4.67a_0$  after the post-synchronisation phase separation has occurred. The particles are coloured using a blue/red scale according to the projection of their  $\mathbf{m}$  unit vector (black arrows) in the direction upwards of the page, while their  $\mathbf{s}$  unit vector is coloured using the same scale, according to the projection in the direction to the left of the page.

as  $\text{Re}_0$  in this chapter. As mentioned at the beginning of chapter 1, the Stokes equations are a good approximation for systems with  $\text{Re} \ll 1$  ( $\text{Re} \rightarrow 0$ ). In our case, we are dealing with particles of  $\text{Re}_0 \approx 0.02 \dots 0.075$ . In the best case, the system Reynolds number  $\text{Re} \approx \text{Re}_0$ . One could argue that this value is far from being 0. We therefore suspect that the post-synchronisation phase separation observed is linked to the single particle Reynolds number  $\text{Re}_0$  not being strictly 0.

In the following sections, we present the simulations and analysis we have carried out in our attempt to elucidate this result. We set  $\phi = 11\%$ ,  $\rho = 1$  and  $\mu = 0.5$  for all the simulations.

## 4.2 Finite $\text{Re}$ analysis and size effects

In order to study any finite  $\text{Re}$  effects on the system dynamics and see if our results agree with what is expected at low  $\text{Re}$ , we have carried out a series of simulations where we vary a single or multiple parameters from amongst: the particle radius  $a_0$ , simulation cubic box length  $L$ , particle Reynolds number  $\text{Re}_0$ , packing fraction  $\phi$  and surface slip flow  $\tilde{B}_{11}$ ; whilst maintaining the rest constant. For the simulations, we choose values of  $\phi$  and  $r_t$  corresponding to points in the state diagram that lead to global synchronisation, specifically  $\phi \approx 11\%$ . We initialise the system with random homogeneous initial configurations of the particle positions starting from both an isotropic and a fully synchronised

state. We then compare these simulations to one another and try to draw conclusions. Our results from these simulations are presented in Fig. 4.2, 4.3 and 4.4.

Since we use the lattice Boltzmann method (LBM) for our simulations, one important parameter from those mentioned above is the particle radius  $a_0$ . If the particle size is too small, the numerical error of the average velocity and velocity fluctuations could increase to an extent where it could prove detrimental to the simulations [92, 111].

In Fig. 4.2, we show simulations at  $\phi \approx 0.11$  and  $r_t \approx 4.67a_0$  of  $N = 204$  squirmers for different  $L$  and  $a_0$ . Additionally,  $C_1 = 0.001$  and  $\tilde{B}_{11} = 0.007$ . Therefore,  $v_0 = \frac{2}{3}\tilde{B}_{11} \approx 0.0047$ . As we vary  $L$  and  $a_0$  from one simulation to another, the single particle Reynolds number  $Re_0$  also inevitably changes since it is proportional to  $a_0$  ( $Re_0 = \rho a_0 v_0 / \mu$ ).

The first interesting result is that the simulations with  $a_0 = 2$  do not synchronise whereas those for  $a_0 \geq 4$  do. Even when the system is initialised in the fully-synchronised state ( $P_s \approx 1$  and  $P_m \approx 1$ ), the order is steadily decreased over time until the system becomes isotropic ( $P_s \approx 0$  and  $P_m \approx 0$ ) (bottom plot in blue panel of Fig. 4.2). At this point, it is unclear whether this result has physical meaning or if it is simply due to the particle size being too small and therefore leading to spurious results as a consequence of numerical errors.

The second interesting result, is the behaviour of the order parameter curves once the system has synchronised for the simulations with  $a_0 = 12$ . The curves present dips and oscillations that seem to be absent from their smaller  $a_0$  counterparts. For  $a_0 = 4$  and  $a_0 = 8$ , once the system finds itself in the synchronised state, the order parameter curves are flat and present small fluctuations around

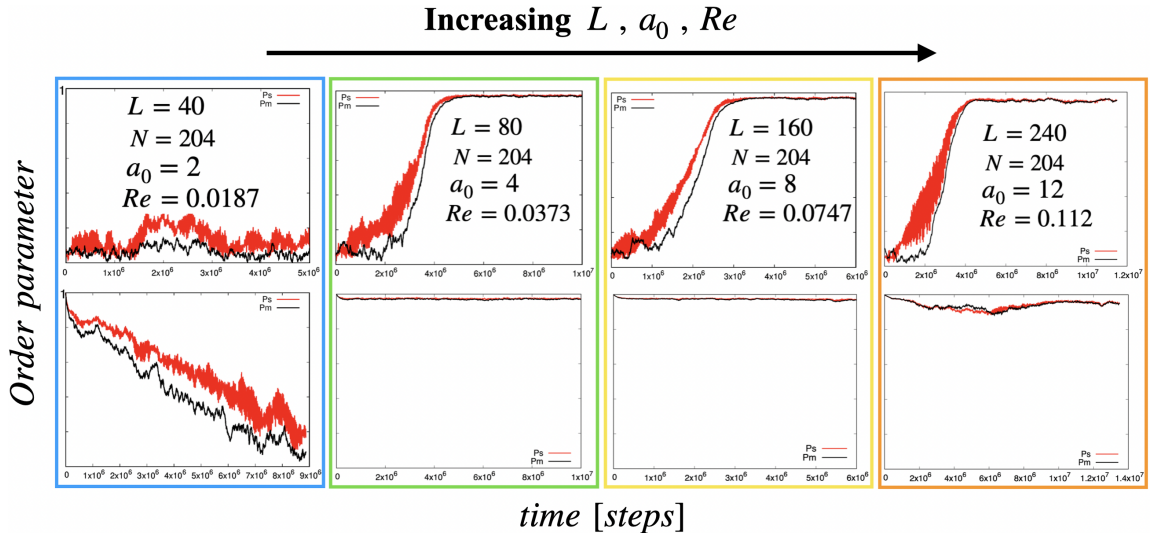


**Figure 4.2. Reynolds number and size effect in circular microswimmer suspensions.** Azimuthal  $P_s$  (red) and polar  $P_m$  (black) order parameter time-evolution for 8 different simulations of suspensions composed of 204 squirmers at  $\phi \approx 11\%$ ,  $C_1 = 0.001$  and  $\tilde{B}_{11} = 0.007$ . Moving from left to right (blue to orange) the particle radius  $a_0$ , box length  $L$  and Reynolds number  $Re_0$  are increased.

the high average values achieved (green and yellow panels in Fig. 4.2). Whereas for  $a_0 = 12$ , the curves present significantly bigger fluctuations. This is in direct contrast to what has been demonstrated in studies regarding the particle size leading to numerical errors using the LB method [92, 111]. Therefore, this result suggests that the large fluctuations for the simulations with larger particles could have a physical interpretation.

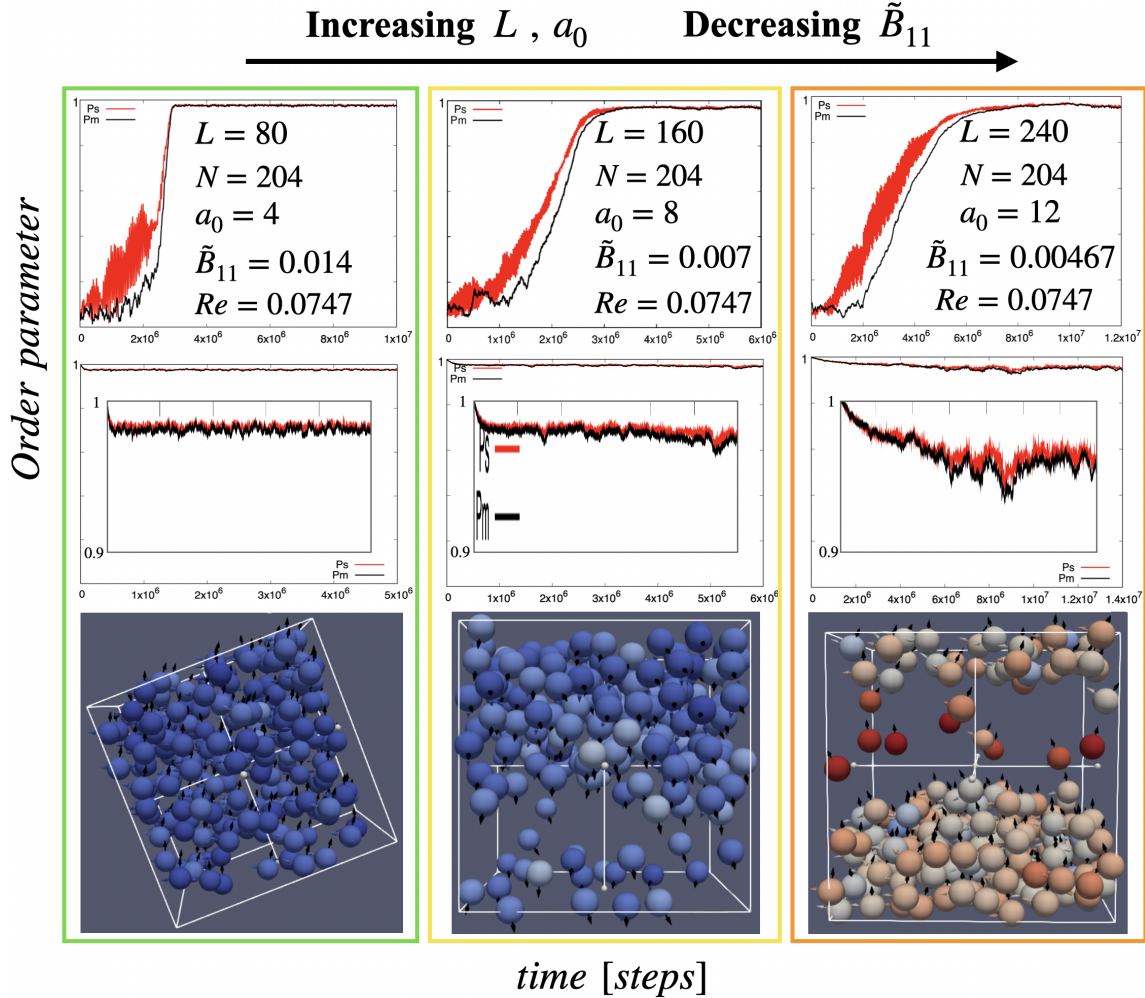


**Figure 4.3. Size effect in circular microswimmer suspensions.** Azimuthal  $P_s$  (red) and polar  $P_m$  (black) order parameter time-evolution for 6 different simulations of suspensions composed of 204 squirmers at  $\phi \approx 11\%$ ,  $C_1 = 0.001$  and  $Re_0 \approx 0.0747$ . Moving from left to right (green to orange) the particle radius  $a_0$  and box length  $L$  are increased while the swimming speed  $2\tilde{B}_{11}/3$  is decreased. Snapshot depicting the configuration of the system in the steady state are shown at the bottom for each case. The particles are coloured according to the  $x$ -component of their azimuthal  $s$  vector, pointing to the right side of the simulation box as seen from the reader's perspective. (Due to a limited storage space, the data corresponding to these curves was not preserved and therefore we resorted to a crude method for the creation of the insets which involves merely stretching out a zoomed-in screenshot of the curves along the vertical axis direction).

In Fig. 4.3, we carry out a similar analysis to that of Fig. 4.2, but this time, we eliminate the  $Re_0$  dependency from one simulation to another by varying

the surface slip-flow magnitude  $\widetilde{B}_{11}$  in such a way so that it scales according to  $a_0$ , leaving  $\text{Re}_0$  constant. When comparing the results of figures Fig. 4.2 and Fig. 4.3, we notice that in the steady, synchronised state ( $P_s \approx 1$  and  $P_m \approx 1$ ), the order parameter curves for  $a_0 = 12$  (orange panels) have flattened out considerably in the latter case, but still show significantly larger fluctuations than those for the  $a_0 = 4$  and  $a_0 = 8$  cases in the same figure (see insets in Fig. 4.3). This suggests that the fluctuations depend at least on  $\text{Re}_0$ . The higher  $\text{Re}_0$ , the larger the post-synchronisation fluctuations in the order parameters. Additionally, given that the simulations in Fig. 4.3 now all have the same  $\text{Re}_0$ , we know that there is an additional dependence of the post-synchronisation order parameter fluctuations on  $a_0$  and/or  $L$ . In the next section, we investigate further in this direction.

For  $a_0 = 4$  and  $L = 80$  the system remains homogeneous throughout the simulation, while for the other cases the system has phase separated into a dense, particle-laden region and a dilute region. When comparing the configurations in each snapshot at the bottom of Fig. 4.3 to each other, we notice that for larger values of  $a_0$ , the system is less monochromatic. Meaning that there is less alignment between the particles. This agrees with the larger fluctuations in  $P_s$ . Another noteworthy observation is that the phase separation always occurs in the direction of the global polar director  $\mathbf{P}_M$ . That is, the dense, particle-rich region spreads out in the plain perpendicular to  $\mathbf{P}_M$ .

Furthermore, the large fluctuations in the order parameters for the post-synchronisation phase-separating cases only appear after the system has already phase separated. This implies that the extensivity of the system (related to  $L$ ) may play a key role in their appearance. The squirmers forming the particle-rich region can be thought of as one single collective body since a high degree of alignment ( $P_s \approx P_m \geq 0.9$ ) is maintained across it. Visualising the system in this regime and following the dynamics frame by frame, it becomes apparent that the squirmers forming the dense region no longer carry out their circular trajectories individually, but instead now rotate in unison as if pertaining to one single body.

This beckons the reassessment of the system's Reynolds number  $\text{Re}$ . Thus far, the system Reynolds number has been directly associated to the single particle Reynolds number  $\text{Re}_0 = \rho v_0 a_0 / \mu \sim 0.02 \dots 0.1$ . In this case however, given that dense region spans across the size of the simulation box, perhaps a better approximation for the system Reynolds number would scale with  $L$  and be given by:  $\text{Re}_{coll} \sim \rho v_{coll} (L/2) / \mu$ . Where  $v_{coll}$  is the velocity of the dense phase which is approximately the same as the average single particle velocity:  $\langle v \rangle \approx v_0$ .

For the  $a_0 = 8$  simulations we have  $\text{Re}_{coll} \approx 0.747$  ( $\text{Re}_{coll} \approx 10 \times \text{Re}_0$ ) and for the  $a_0 = 12$  simulations we have  $\text{Re}_{coll} \approx 1.12$  ( $\text{Re}_{coll} \approx 15 \times \text{Re}_0$ ). Both these cases correspond to the weakly inertial regime rather the zero-Reynolds Stokes flow regime. Therefore, in both these cases we could expect the appearance of *inertial* effects that could be responsible for the growth of the velocity fluctuations in the system. The higher  $\text{Re}_{coll}$ , the stronger the inertial effects and

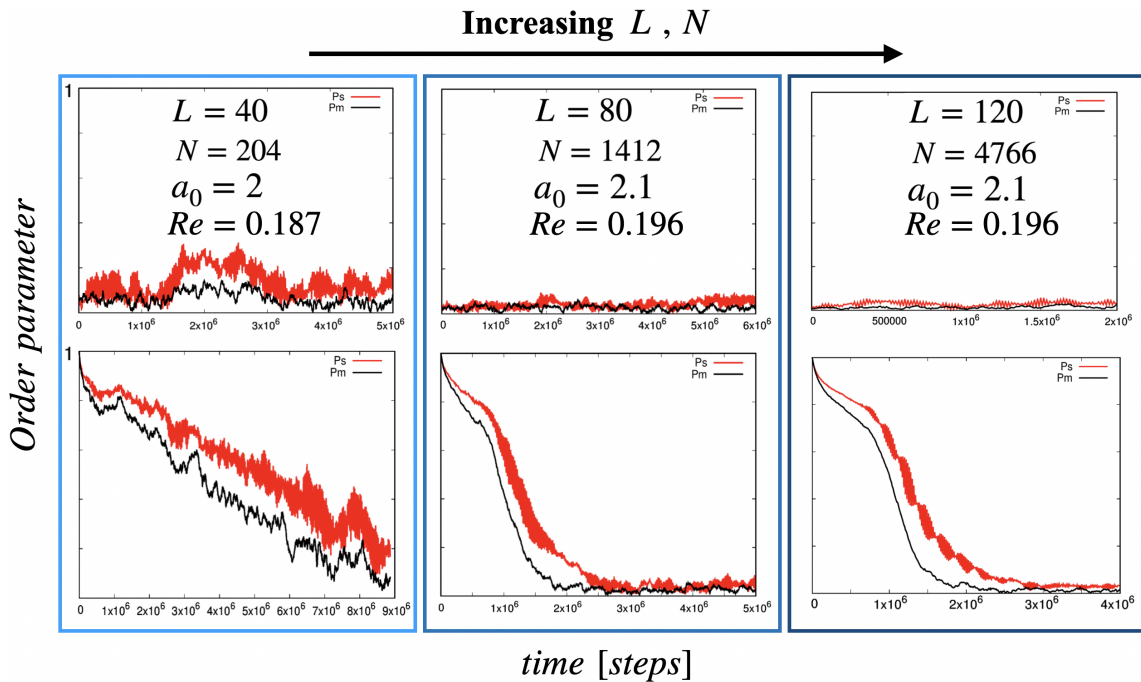


**Figure 4.4. Small circular microswimmers.** Azimuthal  $P_s$  (red) and polar  $P_m$  (black) order parameter time-evolution for 6 different simulations of squirmer suspensions at  $\phi \approx 11\%$ ,  $C_1 = 0.001$ ,  $\tilde{B}_{11} = 0.007$ ,  $a_0 = 2$  (or 2.1) and  $Re \approx 0.0187$  (or 0.0196). Moving from left to right the box length  $L$  and number of particles  $N$  are increased.

the larger the velocity fluctuations leading to a loss of alignment in the system, which is captured by the large fluctuations in  $P_s$  and  $P_m$ .

Before moving on to the next section, we look back at our results for small microswimmers ( $a_0 = 2$ ) in Fig. 4.2 (blue panel) where the system is incapable of reaching or maintaining the synchronised state. According to the work done in [92], for a fixed squirmer size  $a_0$ , a larger box  $L$  leads to smaller numerical errors in the velocity. In order to make sure our results corresponding to a fixed particle size of  $a_0 = 2$  hold independent of the box size, we carry out simulations with the same  $\phi \approx 0.11$  for bigger  $L$ . We also increase the particle size slightly to  $a_0 = 2.1$  in an attempt to minimise any additional uncertainties associated to the particles being able to fit exactly across 4 lattice nodes. The results are presented in Fig. 4.4.

As expected (just due to having better statistics), the fluctuations in the order parameters are smaller for the larger systems. More importantly, the results show that for the larger systems (with slightly bigger particles) synchronisation is lost even faster (bottom plots in Fig. 4.4). However, it still remains unclear to us whether or not this result is due to the velocity error associated to the small particle size or if it has a physical meaning behind it. In the unlikely scenario where the latter case is true, we hypothesise that it could be related to a curvature effect, suggesting that the ratio of surface flow to surface curvature plays an important role at least below a certain threshold.

To summarise, we have carried out a limited scaling analysis of  $a_0$ ,  $L$ , and

$Re_0$ , for  $\phi$  corresponding to a point in the synchronisation diagram for particles of radius  $a_0 = 8$  (see Fig. 4.1) that *first* leads to spontaneous synchronisation from an initial isotropic state; and then, subsequently presents post-synchronisation phase separation. The preliminary analysis presented in Fig. 4.2 and 4.3 suggests that the fluctuations in the order parameters after the system has phase separated depend on  $Re_0$ ,  $L$ , and possibly  $a_0$ . The dependence on  $Re_0$  is made clear by comparing the orange panels of Fig. 4.2 and 4.3 to each other. The dependence on  $L$  and/or  $a_0$  is made clear when comparing the the three panels of Fig. 4.3 to each other. When visualising the phase-separated system, we observe that the particles in the dense, clustered region move in unison. This leads us to the re-definition of the system  $Re$  as  $Re_{coll} \propto L$ . With  $Re_{coll} \sim 1$  in our simulations, corresponding to the weakly inertial regime, we hypothesise that this would give rise to inertial effects and increase the magnitude of the velocity fluctuations.

### 4.3 Large-scale simulations of circular microswimmers

In order to minimise any periodic boundary condition effects and get a better understanding of how the extensivity of the system affects the post-synchronisation phase separation, we move to bigger simulation boxes (larger  $L$ ) while trying to remain within feasible computational times.

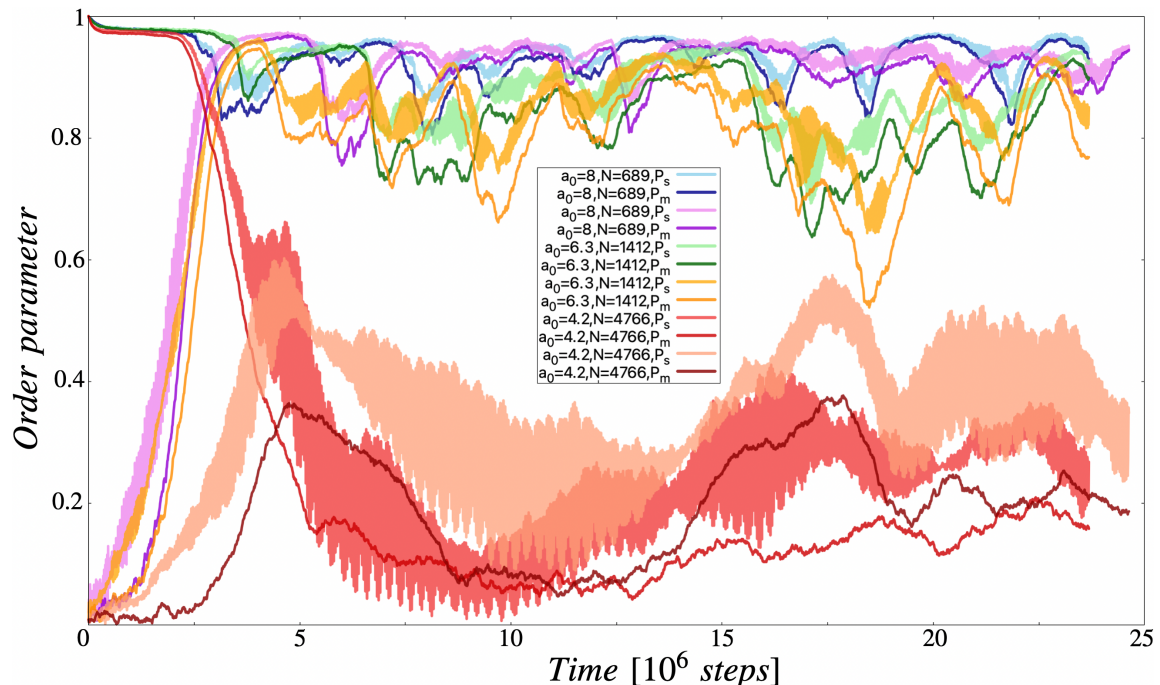


**Figure 4.5. Large-scale simulations of circular microswimmers.** Azimuthal  $P_s$  and polar  $P_m$  order parameter time-evolution for simulations of squirmer suspensions at  $\phi \approx 11\%$ ,  $C_1 = 0.001$  and  $\bar{B}_{11} = 0.007$ .

In Fig. 4.5 we present the simulation results for systems at  $\phi \approx 11\%$  and

$r_t = 4.67a_0$  with  $L = 240$ . We use three different particle sizes:  $a_0 = 4.2$ ,  $a_0 = 6.3$  and  $a_0 = 8$  to fill the simulation box homogeneously with random initial positions for the squirmers and carry out two production runs of almost  $25 \cdot 10^6$  steps for each case. One starting from an isotropic initial configuration with  $P_s \approx P_m \approx 0$ , and another starting from a completely synchronised state with  $P_s = P_m = 1$ .

When comparing the order parameter curves in Fig. 4.5 to those in Fig. 4.2 and Fig. 4.3 we notice a much more exacerbated effect of the fluctuations. The simulations with  $a_0 = 8$  and  $a_0 = 6.3$  present post-synchronisation phase separation. For the simulations with  $a_0 = 4.2$ , there is no phase separation in the system.

For the moment, we focus on the simulations with particle radii of  $a_0 = 8$  and  $a_0 = 6.3$ . In these cases, the system clearly reaches the fully synchronised state  $P_s \approx P_m \approx 1$  from an initially isotropic configuration (see violet and yellow curves in Fig. 4.5). Then, once again, the system phase separates into a dense, particle-rich region and a dilute region with almost no particles in it. After phase separation, large fluctuations in the order parameter values begin to develop. When comparing the order parameter fluctuations for  $a_0 = 8$  (violet and blue curves in Fig. 4.5) to their smaller-box equivalent in Fig. 4.3 and 4.3, the system-extensivity effect is evident. Here the simulation box is 50% bigger and we have more than 3 times more particles. This result agrees with our notion of  $\text{Re}_{coll} \propto L$ . Here,  $\text{Re}_{coll} \approx 1.12$ . For  $a_0 = 6.3$ , we have the same  $\text{Re}_{coll}$  but the order parameter fluctuations are even bigger than those for  $a_0 = 8$  (compare violet and blue curves to yellow and green curves in Fig. 4.5). This implies a dependence on either  $a_0$  or  $N$ , or both.

In [112], the authors study the dynamics of an active particle in an external Poiseuille flow, and explain how active particles in an external flow at low fluid inertia generate an active lift force (in addition to the classical inertial lift of passive particles) that can give rise to the emergence of complex dynamics. Moreover, they show that the dynamics is not only sensitive to the swimmer's hydrodynamic signature, but also its size. Therefore, it could be possible that in our case, we have similar effects due to the squirmers swimming in a self-induced, weakly-inertial, *collective* flow.

The duration and depth of the troughs in the order parameter curves for  $a_0 = 8$  and  $a_0 = 6.3$  in Fig. 4.5 does not seem to be well defined. However, there appear to be significant differences between those for one particle size when compared to those of the other. For  $a_0 = 6.3$  and  $N = 1412$  (yellow and green curves in Fig. 4.5), the troughs are more pronounced and more chaotic, looking more dissimilar between them and irregular in shape; seemingly extending over undefined time intervals. For  $a_0 = 8$  and  $N = 689$  (violet and blue curves in Fig. 4.5), they are less pronounced and less chaotic, with somewhat more regular and smooth shapes; being more well-defined and giving the impression of a similar pattern being repeated at more consistent time intervals.

When visualising the systems, we see notable differences in the dense phase cluster dynamics between the two cases. The cluster with larger and fewer par-

ticles (corresponding to the  $a_0 = 8$  and  $N = 689$  simulations) is much more stable in shape. It continuously breaks up and reforms after every trough in the order parameter time-evolution and more or less maintains a spheroid shape for as long as it lasts. Whereas the cluster with smaller and more particles (corresponding to the  $a_0 = 6.3$  and  $N = 1412$  simulations) undergoes more violent changes in its shape, appearing to stretch, splay and break up at certain parts, form swirls, and has an irregular shape over time. Fig. 4.6 shows snapshots of each system in configurations which are characteristic of each one. These observations match the profile of the order parameter curves well.

As for the squirmers found in the dilute region, they can, at times, be observed being advected in directions perpendicular to their circular motion, towards and away from the clustered, dense region. This observation appears to

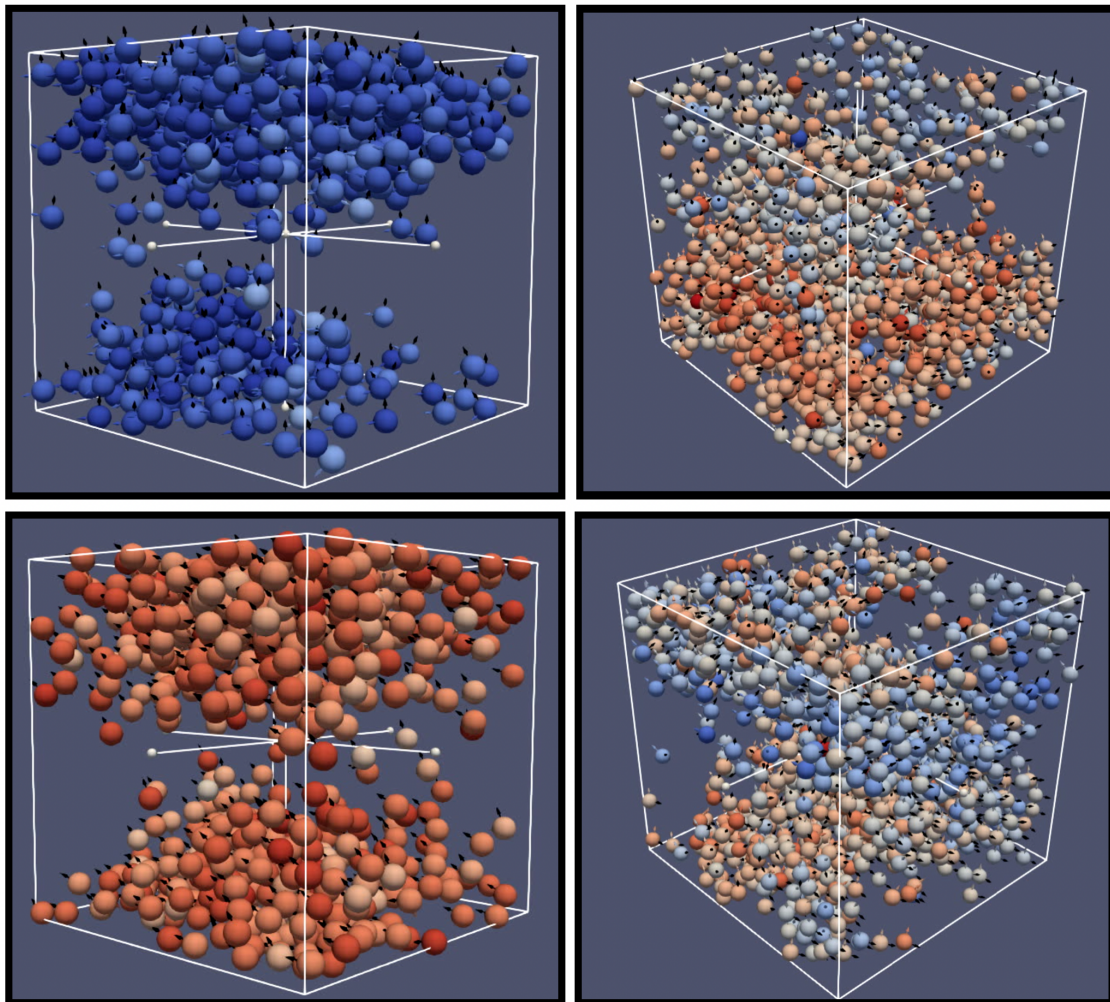


**Figure 4.6. Examples of phase separated circular microswimmer suspensions.** Left: Snapshots of the system corresponding to  $a_0 = 8$  and  $N = 689$  before (top) and after (bottom) the first trough in its order parameter time-evolution. Right: Snapshots of the system corresponding to  $a_0 = 6.3$  and  $N = 1412$  at two different times (top/bottom). The polar unit vectors  $\mathbf{m}$  are represented by black arrows and monochromaticity indicates alignment in the azimuthal direction according to  $s_y$ .

confirm our hypothesis of the emergence of collective flows as a consequence of the system  $Re$  entering the weakly inertial regime with  $Re_{coll} \sim 1$ . A study of the fluid velocity throughout the simulation would be ideal to confirm this hypothesis. Unfortunately, due to the limited time and resources at our disposal, and the size of the system, only the particle information was stored for these simulations. The *fluid* velocity files were saved only for the final configuration of the system due to the large amount of storage space required for them. Therefore, we leave this for future work while we limit ourselves to studying only the *particle* velocities instead.

In the next section, we carry out a more detailed analysis of the  $a_0 = 8$  and  $N = 689$  simulation, using only the particle information generated during the simulations.

## 4.4 Case study of post-synchronisation phase separation

With limited time to our disposal, we focus on the results corresponding to  $a_0 = 8$  and  $N = 689$  in Fig. 4.5 in this section since they are far less complex and easier to analyse than those for  $a_0 = 6.3$ . Specifically, we focus on the first  $t = 125T_0$  cycles of the simulation starting from a fully synchronised state (with homogeneous, random initial particle positions).

### 4.4.A Structure analysis of the clustered phase

To further analyse the cluster state, we calculate the pair-correlation functions  $g(r)$ ,  $g(r_\perp)$  and  $g(r_\parallel)$ . The functions are calculated over  $2T_0$  at three different moments of the dynamics. Just as in chapter 2 (Fig. 2.2b),  $g(r)$  corresponds to the standard radial distribution function of the system; whereas  $g(r_\perp)$  and  $g(r_\parallel)$  correspond to the radial distribution functions calculated perpendicular and parallel to the global polar director  $\mathbf{P}_M$  respectively. The pair-correlations functions are shown in Fig. 4.7.

At the start of the simulation, all three pair-correlation functions have exactly the form we would expect. They show a liquid-like structure with isotropic particle positions (left panel in middle of Fig. 4.7), just like in Fig. 2.2b of chapter 2. Here, the squirmers present a high degree of alignment in their swimming with  $P_v \approx P_s \approx P_m \approx 1$ .

The middle panel in Fig. 4.7 shows the pair-correlation function profiles once the post-synchronisation phase separation is almost complete. The pair-correlation functions now present notable differences between them and with respect to their form at the start of the simulation. As the system phase separates,  $g(r)$  still has the form of a liquid pair-correlation function, but now the density of the system decreases with distance, delineating the phase separation.

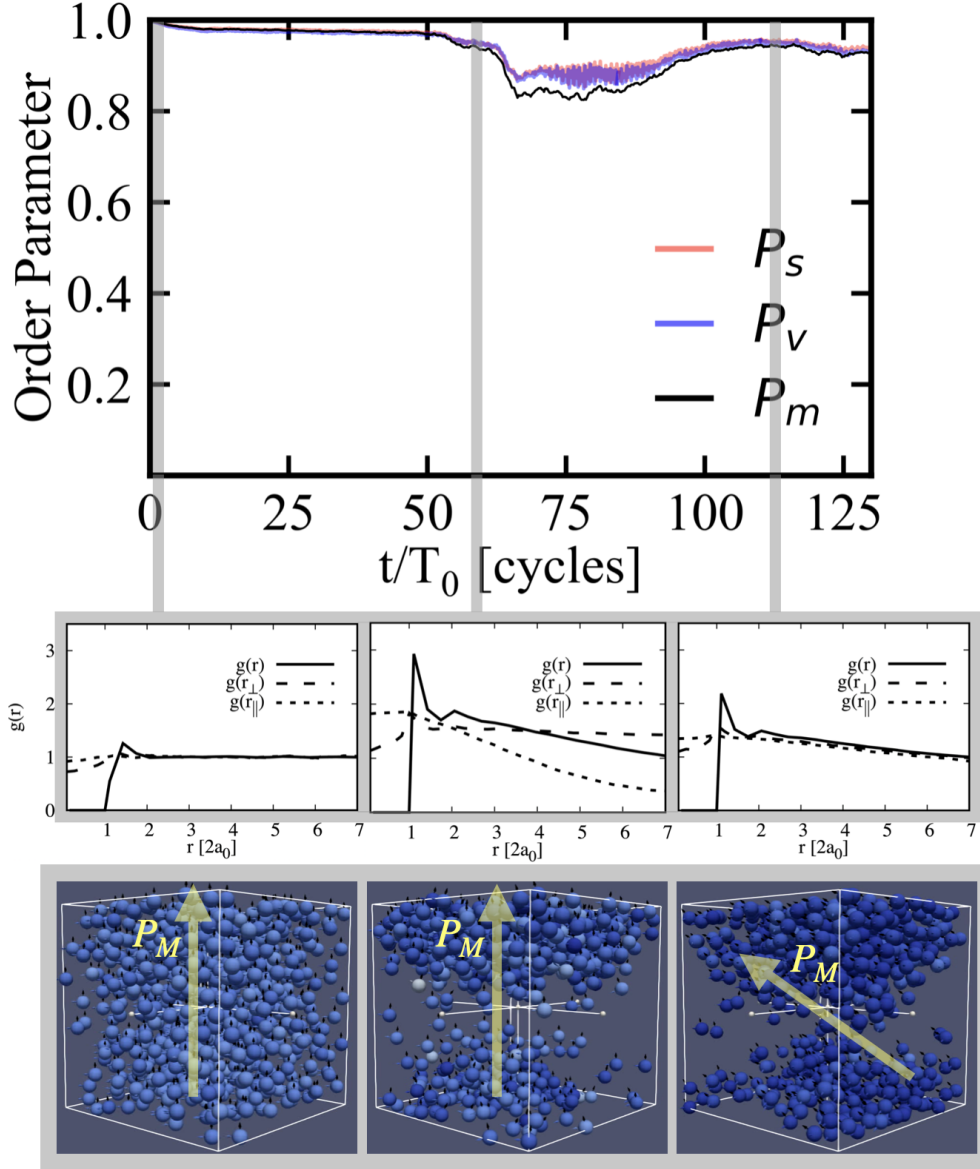


**Figure 4.7. Radial distribution function for phase separation dynamics of circle swimmers.** Time evolution of the azimuthal  $P_s$  (red), velocity  $P_v$  (blue) and polar  $P_m$  (black) order parameters for the first trough in their time-evolution profiles. Radial distribution function  $g(r)$  of the system calculated over  $2T_0$  for 3 different moments in time: at the start of the simulation (left), after phase separation before the loss of alignment (middle), and after the alignment has been recovered (right).  $g(r_\perp)$  ( $g(r_\parallel)$ ) are calculated perpendicular (parallel) to the polar director  $\mathbf{P}_M$ . Snapshots of the configuration of the system at each time interval are shown at the bottom below each case. The particle monochromaticity (over a colour spectrum ranging from blue to red) indicates the strength of alignment in  $P_s$ . Black arrows represent the squirmer polar unit vector  $\mathbf{m}$ .

The same trend, indicating clustering, is portrayed and exacerbated for  $g(r_\parallel)$ . Finally, in stark contrast to its analogues,  $g(r_\perp)$  shows no density variation with distance whatsoever. These observations mean one thing: the system phase separates along the direction of the global polar director  $\mathbf{P}_M$ , spreading out in the

perpendicular direction as it does so.

The panel on the right in Fig. 4.7 shows the form of the pair-correlation functions after the first trough in the order parameter time-evolution, once a high degree of alignment in the system has been recovered. Here, all three pair-correlation functions indicate that the system is phase separated with the cluster now being very much isotropic in shape (with respect to  $\mathbf{P}_M$ ) and therefore approximately spherical in form. Additionally, when compared to the  $g(r)$  profile of the previous time-window, we notice that the system now is more homogeneous despite still being in a clustered state.

Typical configurations of the system in each of these situations are depicted at the bottom of Fig. 4.7. While at first glance the two phase-separated configurations (middle and right snapshots at bottom of Fig. 4.7) may seem almost identical to each other, the change in the orientation of  $\mathbf{P}_M$  leads to the notable differences in the pair-correlation function profiles.

During these first  $125T_0$  of the simulation, the pair-correlation functions show how the system undergoes changes in its density, compressing and expanding before and after every trough, evocative of a “breathing motion”. Interestingly, at the end of the cycle, the global polar director  $\mathbf{P}_M$  re-orientates in a different direction.

#### 4.4.B Particle velocity analysis and enhanced diffusivity

With the order parameters  $P_v$ ,  $P_s$  and  $P_m$  providing limited information, in this subsection, we calculate the average velocity  $\langle u \rangle$  of the whole squirmer population and the associated standard deviation  $\sigma_u$  in an attempt to shed more light on the system’s dynamical behaviour. Since for these simulations almost all the squirmers are found in the dense clustered phase, with very few of them being in the dilute region, we can approximate  $\langle u \rangle$  and  $\sigma_u$  to the average velocity and velocity fluctuations of the particle cluster.

Fig. 4.8 shows the order parameter curves for  $P_s$ ,  $P_v$  and  $P_m$ , the mean squared displacement (MSD) of the system, and  $\langle u \rangle$  and  $\sigma_u$  during the the first  $t = 125T_0$  cycles of the simulation.

The most noteworthy aspect of Fig. 4.8 is the curve for the velocity fluctuations  $\sigma_u$ . Starting from the synchronised state, the velocity fluctuations slowly grow over time while  $\langle u \rangle$  remains roughly constant and the system begins to phase separate around  $t/T_0 \sim 50$ . As the system begins to phase separate and form the particle cluster, there is a small increase in  $\langle u \rangle$  and a drastic increase in  $\sigma_u$ . At around  $t/T_0 \sim 60$  (grey dotted vertical line in Fig. 4.8)  $\sigma_u$  peaks at its maximum value. This point corresponds to the end of a sharp fall in the order parameter values. From this point on,  $\sigma_u$  decreases and  $P_v$ ,  $P_s$  and  $P_m$  fluctuate at a plateau until the order slowly builds back up again as the squirmers begin to re-align their velocities and re-synchronise with a new orientation for  $\mathbf{P}_M$

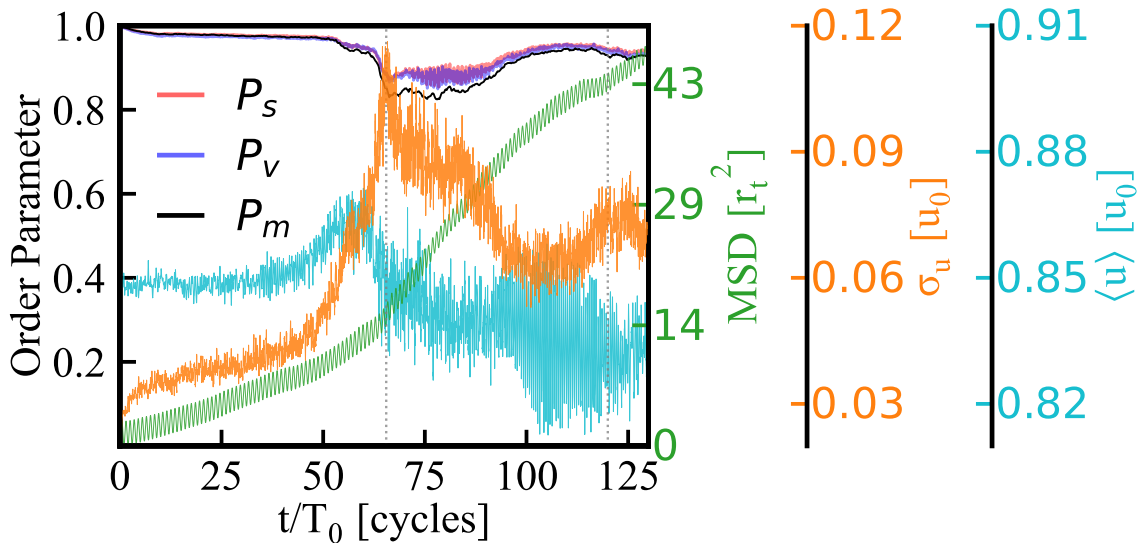


**Figure 4.8. Post-synchronisation velocity analysis for circular swimmers.** Time evolution of the azimuthal  $P_s$  (red), velocity  $P_v$  (blue) and polar  $P_m$  (black) order parameters for the first trough in their time-evolution profiles. The mean square displacement (MSD) (green), average velocity of the squirmer population  $\langle u \rangle$  (cyan) and the corresponding standard deviation  $\sigma_u$  (orange) are calculated during this time. The grey dotted vertical lines approximately mark peaks in  $\sigma_u$ .

(see snapshots in Fig. 4.7). Soon after, the velocity fluctuations begin to build up again as the system begins what would correspond to the second cycle of the “breathing motion”. We note that throughout this process  $\langle u \rangle$  roughly remains the same, with an associated standard deviation ( $\sigma_{\langle u \rangle}$ ) in the region of 1%. On the other hand, the standard deviation for  $\sigma_u$  ( $\sigma_{\sigma_u}$ ) is in the region of 33%. While magnitude of the average velocity of the system is conserved (blue curve in Fig. 4.8), it undergoes significant changes in the magnitude of its fluctuations (orange curve in Fig. 4.8) that are not random; but instead correspond to the form of a curve that presents notable variations with physical meaning behind them, reflecting the system dynamics.

During the time between consecutive peaks of  $\sigma_u$ , we notice that the MSD increases. The increase in the velocity fluctuations appears to be directly linked to an enhanced diffusivity in the system. In Fig. 4.9, we plot the order parameter ( $P_s$  and  $P_m$ ) time-evolution and the mean square displacement (MSD) of the system for 500 cycles (in  $T_0$ ) of simulation time. Grey dashed vertical lines approximately mark the points at which the order parameters experience a sharp and abrupt plunge in value (corresponding to maxima in the velocity fluctuations for each cycle of the system’s “breathing motion”). Most of the vertical lines roughly coincide with kinks or bends in the MSD that correspond to an increase of diffusivity.

The results in this subsection show a good agreement with our hypothesis of inertial effects: As the system phase separates with the squirmers forming one large cluster that spans the box length  $L$ , its Re increases due to the par-

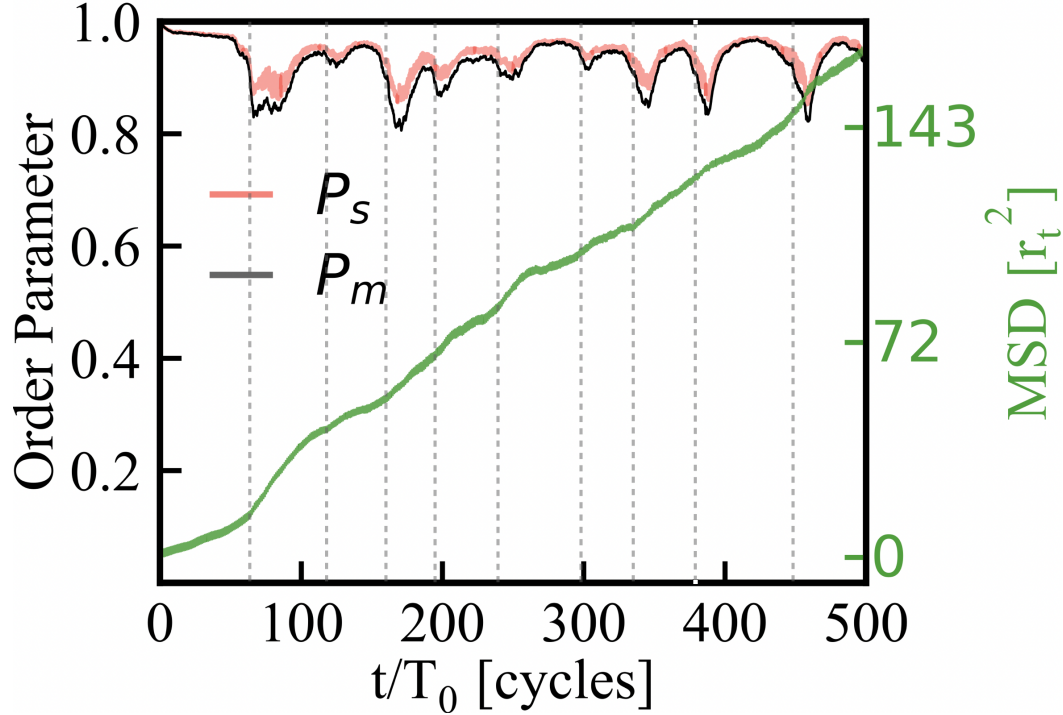


**Figure 4.9. Enhanced diffusivity for circle swimmers.** Time evolution of the azimuthal  $P_s$  (red) and polar  $P_m$  (black) order parameters. Mean square displacement (MSD) (green) presenting regions with enhanced diffusivity that roughly correspond to the grey dashed vertical lines which approximately mark the steepest negative gradients for the order parameter values.

ticles in the cluster roughly moving as one single body ( $Re_{coll}$ ). With  $Re$  now corresponding to the weakly inertial regime, a particle-driven, collective flow begins to develop while the squirmer velocity fluctuations experience a significant growth. These effects could be responsible for the observed enhanced diffusivity with every cycle of the breathing-motion.

As the squirmer velocity fluctuations increase, the degree of alignment between the squirmers is decreased. This breaks up the cohesion of the collective and would lead to a smaller  $Re$ . When  $Re$  is decreased, the system becomes less inertial. If the  $Re$  is such that there is nothing left to support the particle-driven flows, they will begin to vanish. As the collective flows die out with the particle cluster less intact, the squirmers begin to increase their alignment, recovering the fully-synchronised state, and bringing an end to the cycle.

#### 4.4.C Microswimmer dynamics

In this subsection we carry out a slightly more detailed study of the microswimmer dynamics before, during, and after the post-synchronisation phase separation.

In Fig. 4.10, we choose 13 microswimmers at random and track them throughout the first cycle of the breathing-motion. We trace out the trajectories of the

particles for  $2T_0$  or  $T_0$  and colour them according to the  $z$ -component of their  $\mathbf{m}$  unit vector ( $m_z$ ) (see Fig. 1.3 for reference). Depending on the case, the particles themselves are coloured according to the  $z$ -component of their  $\mathbf{s}$  vector ( $s_z$ ), or in a similar fashion to their trajectory ( $m_z$ ).

We show snapshots of the system at 5 different times: at the very beginning of the simulation (blue panel in Fig. 4.10); in the phase separated state just before the order parameters plummet in value (green panel in Fig. 4.10); at the beginning of the order parameter recovery (yellow panel in Fig. 4.10); at the peak of the order parameter values before the second cycle begins (magenta panel in Fig. 4.10); and at the end of the first breathing-motion cycle (orange panel in Fig. 4.10).

As mentioned earlier, the system is initialised in the fully synchronised state, with all the squirmers aligned ( $P_s \approx P_m \approx 1$ ) with their  $\mathbf{m}$  unit vectors pointing in the positive  $z$  direction. With the microswimmers programmed to undergo circular trajectories, this means that they would orbit in the  $xy$ -plane individually. The blue panel in Fig. 4.10 that corresponds to the first  $2T_0$  of the trajectory (marked by the vertical blue line in the order parameter plot) shows a very high degree of monochromaticity. This indicates a very high degree of alignment. The squirmers carry out their circular orbits while they remain phase locked and frequency locked with little fluctuations. The high degree of orientational order is maintained for about  $50T_0$ .

After about  $50T_0$ , the system begins to phase separate (as shown in Fig. 4.7) along the global polar director  $\mathbf{P}_M$  and the velocity fluctuations increase rapidly (Fig. 4.8). Once the system is well phase separated into a dense particle-laden phase and a dilute phase with almost no particles in it, the swimmers found in the dense phase cluster together and move in unison as if they were one single body. A relatively high degree of orientational order is still maintained. The green panel in Fig. 4.10 shows how some of the 13 chosen squirmers are found in the midst of the cluster, some on the periphery, and some in the dilute region. The microswimmers found well outside the cluster continue to have approximately circular trajectories in the  $xy$ -plane over the  $2T_0$  time-window. One of the swimmers found deep in the cluster however, seems to have moved upwards along the  $z$ -axis while orbiting in the  $xy$ -plane, presenting a helical trajectory (see top-left corner of top-right snapshot in green panel of Fig. 4.10. Due to the PBCs, the particle is at the bottom of the box). Curiously, the squirmers that find themselves at the periphery of the cluster during the time-window appear to have tilted their axis of rotation, no longer orbiting in the  $xy$ -plane. At the bottom of the top-right snapshot in the green panel of Fig. 4.10, we can even see a squirmer that appears to have initially been in the cluster, change the orientation of its axis of rotation within a time of approximately  $T_0$  and exit the cluster. Another squirmer close by, appears to have entered the cluster while initially being at the periphery.

These observations show that while the cluster roughly preserves its size and shape during an extended period of time, its composition is quite dynamic. Particles are continuously being exchanged at its border, exiting and entering

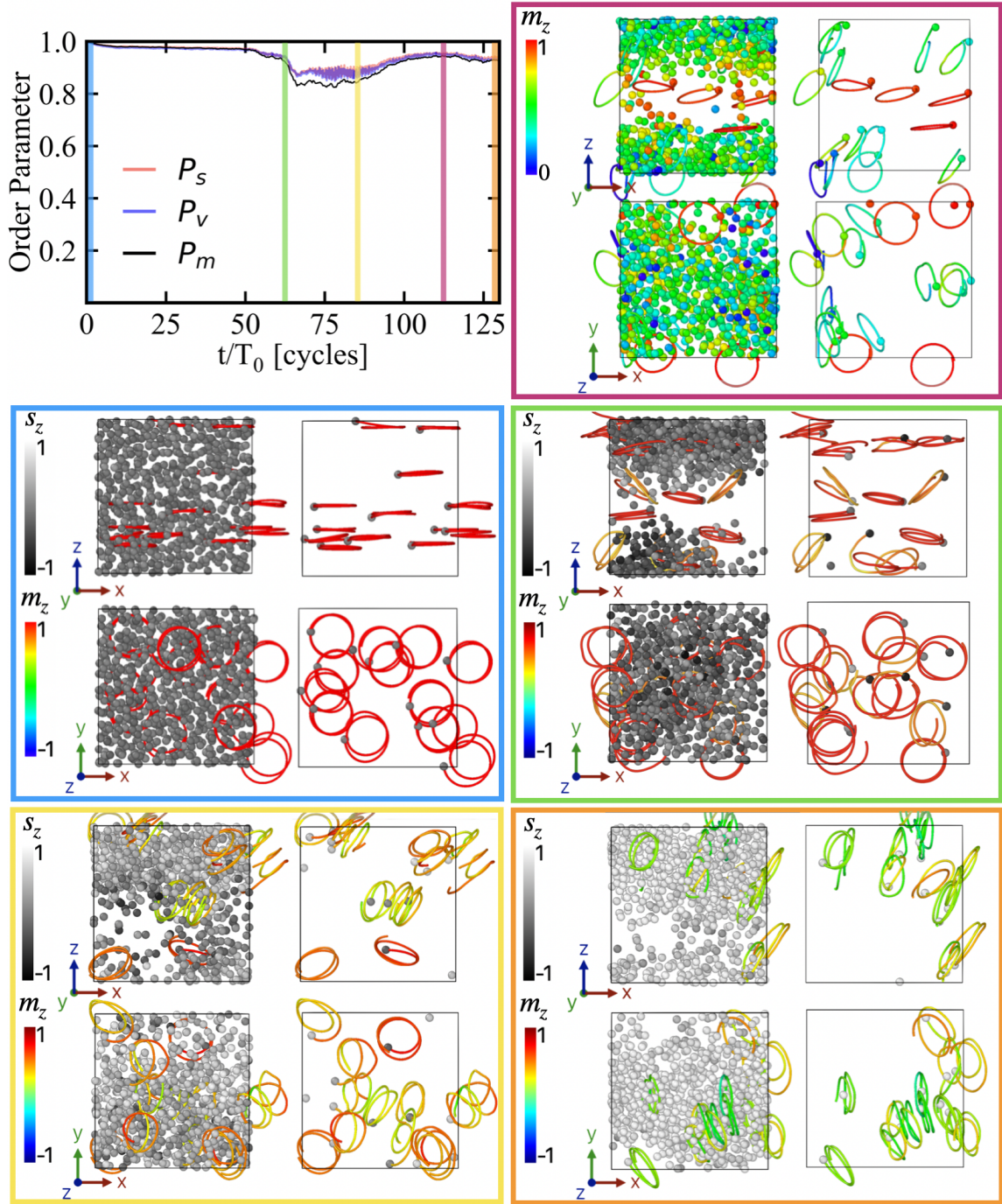


**Figure 4.10. Post-synchronisation circular microswimmer dynamics.** Time evolution of the azimuthal  $P_s$  (red), velocity  $P_v$  (blue) and polar  $P_m$  (black) order parameters for the first trough in their time-evolution profiles. Snapshots of the system for 5 different times with the particle trajectories over the previous  $2T_0$  or  $T_0$ : At the start of the simulation (blue); in the phase separated state just before the order parameters plummet in value (green); at the beginning of the order parameter recovery (yellow); at the peak of the order parameter values before the second cycle of the breathing motion begins (magenta); and at the end of the first breathing cycle (orange). The particles and their trajectories are coloured according to the colour schemes displayed on the left of each panel.

it. Here, it is important to recall that the neutral squirmer far-field flow is not expected to induce any torques [83]. Therefore the torques on the squirmers cannot be caused by the neutral squirmer far-field flow. When closely studied, some of the squirmer trajectories present kinks in certain parts, corresponding to an abrupt change in the swimmer’s motion. This means that the swimmer has most probably come into close contact with one or more other squirmers in a collision-like fashion. One hypothesis is that in this scenario the near-field hydrodynamic interactions, which remain unknown to us, could be responsible for inducing a torque on the squirmer.

As for the alleged emergent collective flows in the system, it is unclear to us as of yet whether they could be capable of inducing hydrodynamic torques as well. Instead, our results suggest that vertical flows develop in certain regions of space. For example, the trajectory lines of the squirmer found deep in the cluster with an upward helical motion is smooth and lacks any creases (top-left corner of top-right snapshot in green panel of Fig. 4.10). When studying the dynamics of the system frame by frame corresponding to this time-window, the cluster begins to wobble in the direction of  $\mathbf{P}_M$  while it continues to rotate in the perpendicular plane. It is as if a transversal wave propagated through it. The particles in the cluster now display periodic motion both in the  $xy$ -plane and along the  $z$ -axis. Both having a period of  $\approx T_0$ .

Signs of vertical advection in the system can also be seen outside the cluster. With the squirmers closer to the cluster being advected towards and away from it while orbiting in the plane perpendicular to the advection. Even two of the squirmers found in the dilute region present smooth helical trajectories, albeit with a very small pitch (top-right snapshot in green panel of Fig. 4.10). One of them moves upwards and away from the cluster during the time-window, and the other downwards towards the cluster (taking the shortest distance to the cluster into account).

After the peak in the velocity fluctuations and before the alignment in the system builds up again, most of the particle trajectories are no longer in the  $xy$ -plane (yellow panel of Fig. 4.10). The particle cluster is less well-defined as the system is more isotropic and homogeneous compared to the previous time-windows. Eventually, alignment is recovered and the cluster becomes more pronounced (magenta and orange panels of Fig. 4.10) with the particles in it now rotating about a newly oriented  $\mathbf{P}_M$  that points in a different direction. All the 13 tagged particles now find themselves in the re-oriented cluster. In the magenta panel of Fig. 4.10, we add 4 extra particles to show that not all the squirmers rotate approximately about  $\mathbf{P}_M$ . Curiously, these 4 particles do not form part of the cluster and are found rotating in the dilute region with approximately the same orientation as in the initial state of the system, despite all four of them having entered the cluster previously and having changed their initial orientation. As we move from the middle of the dilute region to the centre of the cluster, we notice a seemingly continuous change of the squirmer axis of rotation ( $\mathbf{m}$ ) going from the  $z$ -direction in the middle of the dilute region, to the  $x$ -direction in the middle of the cluster.

In Fig. 4.11, we track a single particle throughout the time duration of the trough in the order parameter values in Fig. 4.10. This time corresponds approximately to  $30T_0$ , spanning from  $60T_0$  to  $90T_0$  in the order parameter time-evolution (see top-left panel in Fig. 4.10). Here, the cluster is less well-defined and the particle velocity fluctuations are high. In this time period, we observe the maximum and minimum particle velocities in the simulations. We unwrap the particle positions and the tracked particle is marked black. The rest of the particles are coloured according to a colour-scheme ranging from the maximum, to the minimum vertical particle velocity detected throughout the simulation,  $v_{z_{max}} \approx 1.18v_0$  to  $v_{z_{min}} \approx -1.23v_0$ . The trajectory of the marked particle is coloured according to another colour-scheme that ranges from  $m_z = 1$

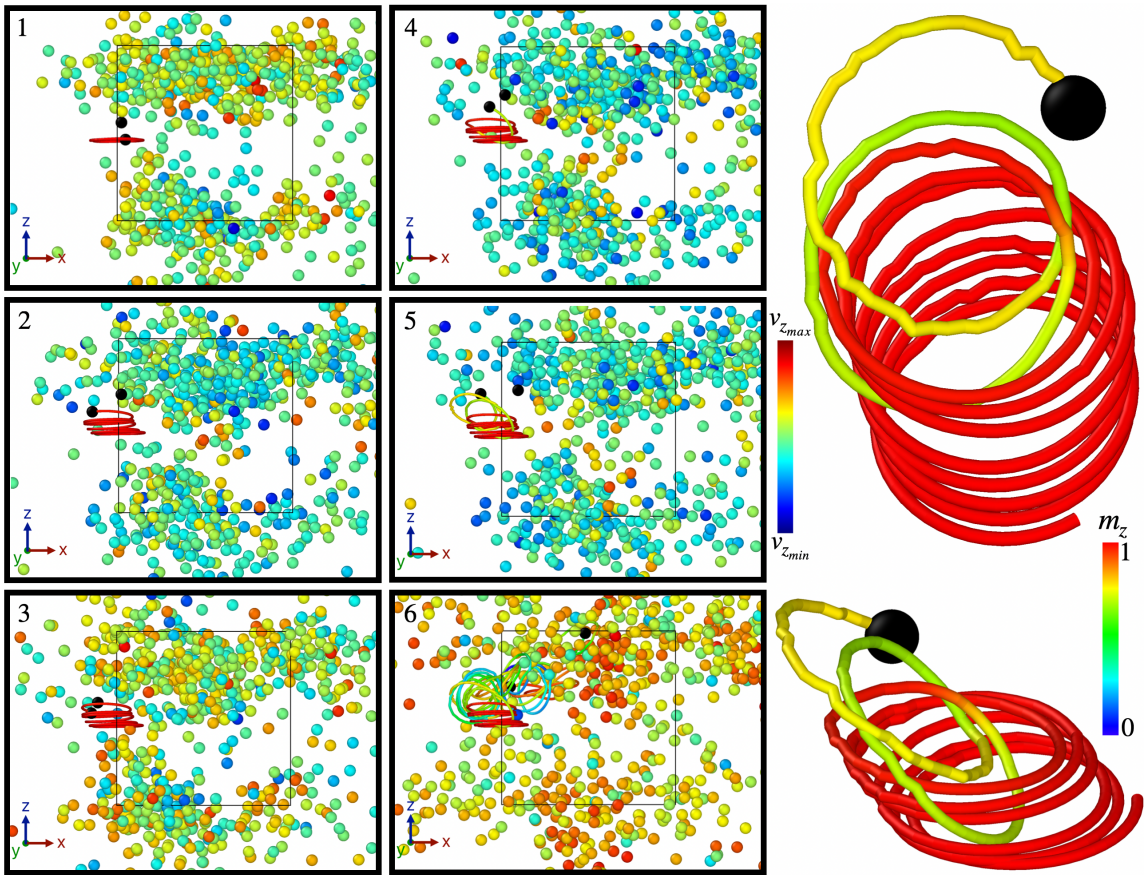


**Figure 4.11. Advection in phase-separated circular microswimmer suspensions.** Panels 1 – 6 show the sequential evolution of the system and selected particle trajectory at six different moments in time. The selected, tracked particle is coloured black. The particle with which it collides within the time frame given from panel 1 to 6 is also coloured black. The unwrapped trajectory is coloured according to the projection of the squirmer  $\mathbf{m}$  unit vector in the  $z$ -direction,  $m_z$ , with the “rainbow” colour-scheme that ranges from  $m_z = 1$  to  $m_z = 0$ . The rest of the particles are coloured according to the “jet” colour-scheme ranging from the maximum, to the minimum vertical particle velocity detected throughout the simulation,  $v_{z_{max}}$  and  $v_{z_{min}}$  respectively. Enlarged images of the tracked particle trajectory from two different view-points are shown at the right.

to  $m_z = 0$ . Additionally, we also colour black a second particle that comes into very close contact with the first particle. In order to have a high resolution of the particle trajectory, we record the particle positions every  $0.02T_0$ , corresponding to free-particle travelled distances of  $\approx 0.6a_0$  or 4.7 lattice nodes, and giving us 50 frames per  $T_0$ .

A total of 6 snapshots are shown in Fig. 4.11. In the first snapshot, we show the trajectory of the tagged particle over  $2T_0$ . Here, the particle is in the dilute region. As we can see, the trajectory is coloured red ( $m_z = 1$ ) and flat. In the next snapshot (2), the particle has moved upwards over a time of  $3.5T_0$ . Snapshot 3 corresponds to one frame before the tracked particle alters its trajectory significantly due to coming into very close contact with the other black particle. The change in motion of the particle is seen in snapshot 4. Its axis of rotation, or polar axis  $\mathbf{m}$ , has shifted significantly, with a change of approximately  $45^\circ$ . The particle then rotates in the new direction for about  $2T_0$  (snapshot 5) before it finds itself at the periphery of the dense clustered phase. It then begins to carry out a more chaotic trajectory, continuously changing the direction of axis of rotation  $\mathbf{m}$  as it passes through the dense region (snapshot 6).

Looking closely at the marked particle trajectory, we notice that as it comes close to other neighbouring particles, its trajectory begins to become less smooth. It begins to present small kinks and become jagged. For the first few circular revolutions (each corresponding to a time of  $T_0$ ), while the particle is still in the dilute region and before the collision with the other marked particle, the trajectory presents small kinks only on one side as it comes closer to other neighbouring particles also in the dilute region (see enlarged images of particle trajectory at the right of Fig. 4.11). Otherwise, the trajectory is smooth. Moreover, the particle presents a net upwards motion with time that is not due to collisions with other particles nor the particle's motion itself since its active swimming is in the plane perpendicular to the vertical motion. This observation agrees with our hypothesis of the existence of collective flows.

As the particle moves upwards and approaches the dense region, the kinks in its trajectory become more frequent and more pronounced (end part of red coloured section of particle trajectory at the right of Fig. 4.11). Eventually it collides with the neighbouring particle and changes its orientation of rotation (change of colour of the trajectory in Fig. 4.11). This observation suggests that the near-field hydrodynamics can indeed induce torques on the squirmers. With the particle now rotating in a different direction, it finds itself interacting more violently with the other particles at the edge of the clustered region. It experiences multiple close contact interactions with its trajectory now being more jagged rather than smooth (yellow part of trajectory in Fig. 4.11). Eventually, it enters the dense region where it changes direction of rotation much more frequently as it chaotically moves through the cluster (change of colours of trajectory in panel 6 in Fig. 4.11) and is no longer found in close proximity to the other tagged particle it collided with.

In a back-of-the-envelope calculation, the tracked squirmer in Fig. 4.11 shows

a maximum vertical velocity of  $\sim a_0/(T_0/4)$ . This corresponds to  $\approx 0.14v_0$ , not too far from  $|v_{z_{max}}|$  (which is the maximum recorded vertical velocity for the whole simulation), and giving a rough estimate of the strength of the advection (in the region of 10% of  $v_0$ ).

Finally, in Fig. 4.12 we show the full, unwrapped trajectories of 3 tagged microswimmers at 4 different times. The tagged particles are coloured red while the trajectories and the rest of the particles are coloured according to the projection of their polar unit vector  $\mathbf{m}$  (which points in the direction of their axis of rotation) in the  $x$ -direction  $m_x$ .

Panel 1 corresponds to a time shortly before phase separation occurs. The system is in the synchronised state, homogeneous, and with all the particle  $\mathbf{m}$  vectors pointing approximately in the positive  $z$ -direction with small fluctuations, corresponding to a green colour. In panel 2, the system has phase separated into a dilute region and a clustered, dense region. On average, the particles close to the borders of the clustered region undergo the biggest changes in their  $\mathbf{m}$  orientation. Their  $\mathbf{m}$  begins to point along the negative  $x$ -direction, corresponding to a colour change from green to blue. One of the 3 tagged

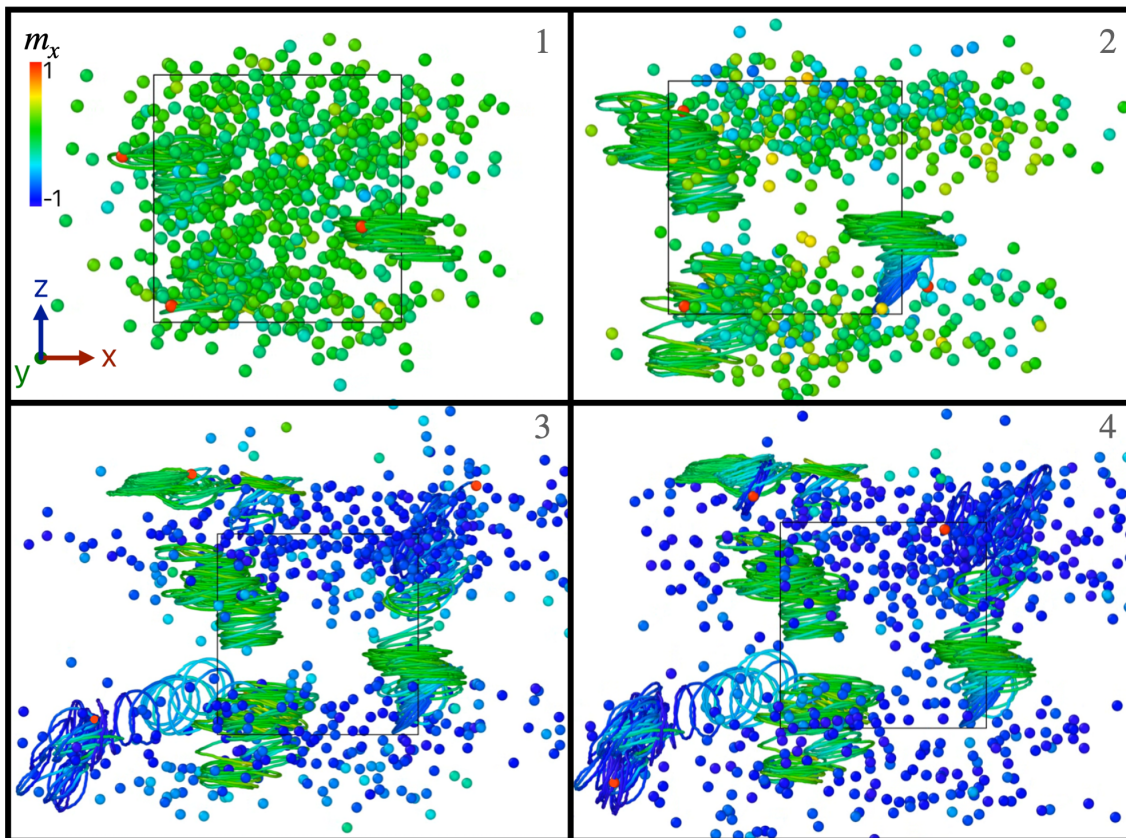


**Figure 4.12. Tracking circular microswimmer trajectories before and after phase separation.** The panels 1 – 4 show the sequential evolution of the particle trajectories at four different moments in time. The three tagged particles are coloured red. Their trajectories, and the rest of the particles are coloured according to the projection of the squirmer  $\mathbf{m}$  unit vector in the  $x$ -direction,  $m_x$ . The trajectories and particle positions are unwrapped.

particles is in this situation.

Panel 3 shows the state of the system after the reorientation of  $\mathbf{P}_M$  and the average cluster rotation. The polar axes  $\mathbf{m}$  of the particles in the cluster now point in approximately the same direction as that of the particles found at the cluster periphery in the previous panel (panel 2). That is, in approximately the  $x$ -direction, corresponding to a blue colour. Two of the tagged particles are now in the clustered phase and the other one has re-entered the dilute phase after having spent some time in the cluster. Similarly, The two particles in the cluster have previously spent some time in the dilute phase. Once again, this shows that the clustered phase is dynamic, continuously exchanging particles with the dilute region. Furthermore, the trajectories of the particles appear to be more chaotic when they are close to the cluster's periphery. For example the end of the trajectory of the particle at the bottom-left corner of panel 3. In panel 4 the particles begin to spread out in the  $zy$ -plane perpendicular to  $\mathbf{P}_M$ . The system is in the synchronised state presenting a high degree of alignment.

## 4.5 Formation of travelling bands with local polarisation

In this section we present our brief analysis corresponding to the simulations with squirmer radii of  $a_0 = 4.2$  in Fig. 4.7. The order parameter time-evolution for this case shows a completely different behaviour to that for  $a_0 = 8$  and  $a_0 = 6.3$ . As we can see in Fig. 4.7, in this case the system is unable to reach the globally synchronised state. The curves show large fluctuations in  $P_s$ . Additionally, both  $P_s$  and  $P_m$  oscillate around values of roughly 0.3 and 0.2 respectively.

Fig. 4.13 shows the pair-correlation function  $g(r)$  of the system at the beginning and end of the simulations. The system remains homogeneous throughout the simulations showing liquid-like structure. Interestingly, in the steady state, we observe what seems to be a travelling band with local polarisation (see panels in Fig. 4.13). As we move along the direction of the band propagation, we note a continuous change in the azimuthal orientation of the circular swimmers. The squirmers found inside the band have approximately the opposite azimuthal orientation  $\mathbf{s}$  of those found outside it. Extending along the plane perpendicular to the band's propagation direction, the squirmers show a high degree of alignment in their  $\mathbf{s}$  vectors. This is marked by the colour of the squirmers in Fig. 4.13. We colour the particles based on the projection of their  $\mathbf{s}$  vector in the directions of the band propagation using a red/blue colour-scheme. On the other hand, the squirmers show absolutely no alignment between their polar axes  $\mathbf{m}$ . The squirmer  $\mathbf{m}$  unit vectors point in all directions. Moreover, the motion of the system presents oscillations in the plane perpendicular to the travelling band as well, making the dynamics more complex.

When the simulation is visualised, we notice that the two regions composed of

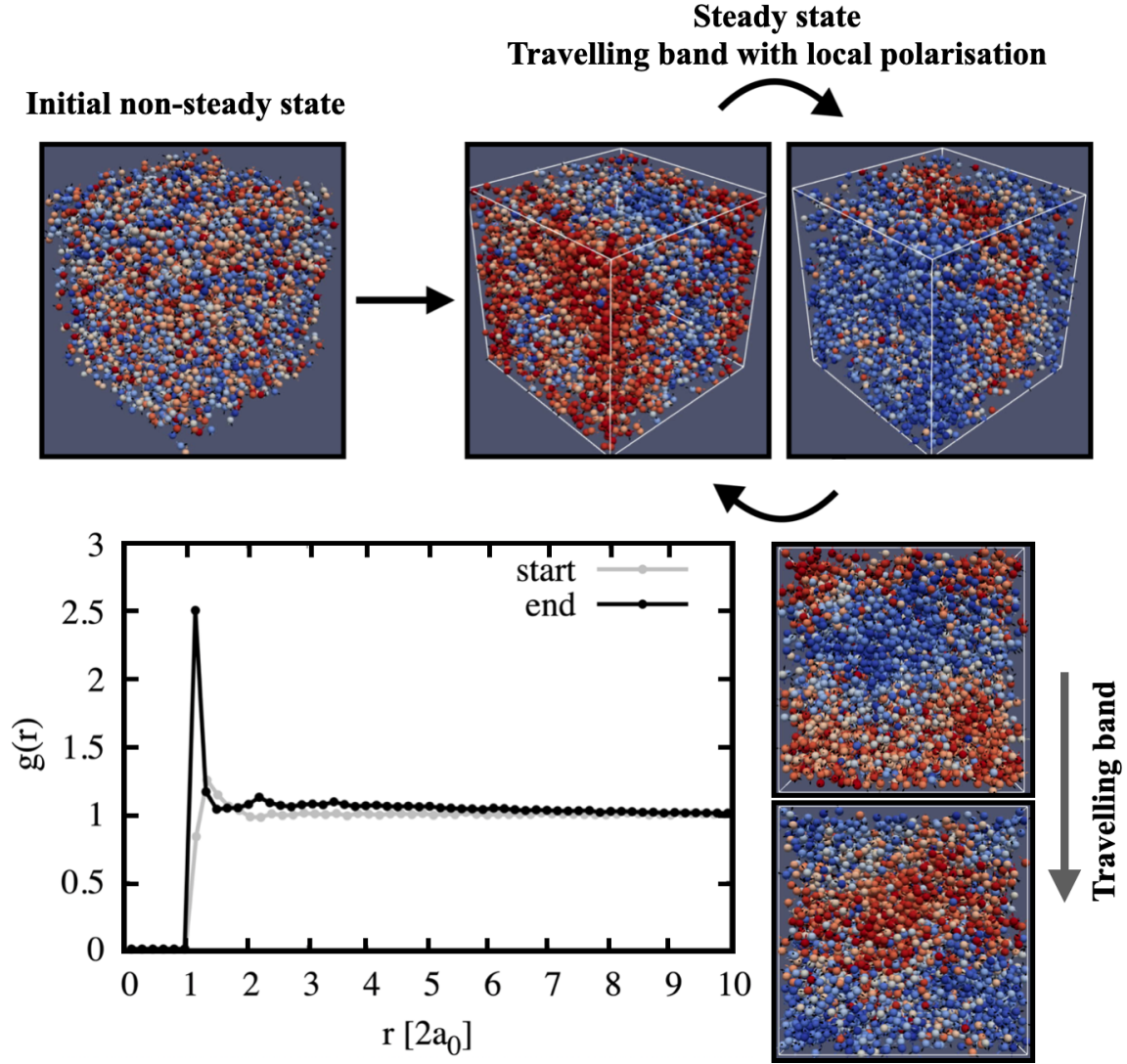


**Figure 4.13. Traveling bands with local polarisation in circle microswimmer suspensions.** Analysis of the simulations of circular swimmers with  $a_0 = 4.2$  in Fig. 4.7 initialised in an isotropic configuration. The radial distribution function is shown for the start and end (steady state) of the simulation. The panels show snapshots of the system at the beginning, and at in the steady state where travelling bands of local polarisation appear. The particles are coloured according to their  $\mathbf{s}$  projection in the direction of the travelling band using a red/blue colour scheme.

the squirmers inside the travelling band and those outside it, rotate in opposite directions to each other. This may account for the large fluctuations observed in the time evolution of  $P_s$ , in a similar way to what we discussed regarding the racemic mixtures studied in section 3.2 of chapter 3. Therefore, if we were to plot the azimuthal order parameter  $P_s$  of each region, we would expect a significantly higher amount of order than the one shown for the whole suspension in Fig. 4.7.

In Fig. 4.14 we show the results of the particle velocity analysis similar to that of Fig. 4.10. Due to the size of the data, corresponding to  $N = 4766$ , in this case we only calculate  $\langle u \rangle$  and  $\sigma_u$  at 5 different points of the first  $380T_0$  of the simulation. (These points correspond to the only saved particle velocity

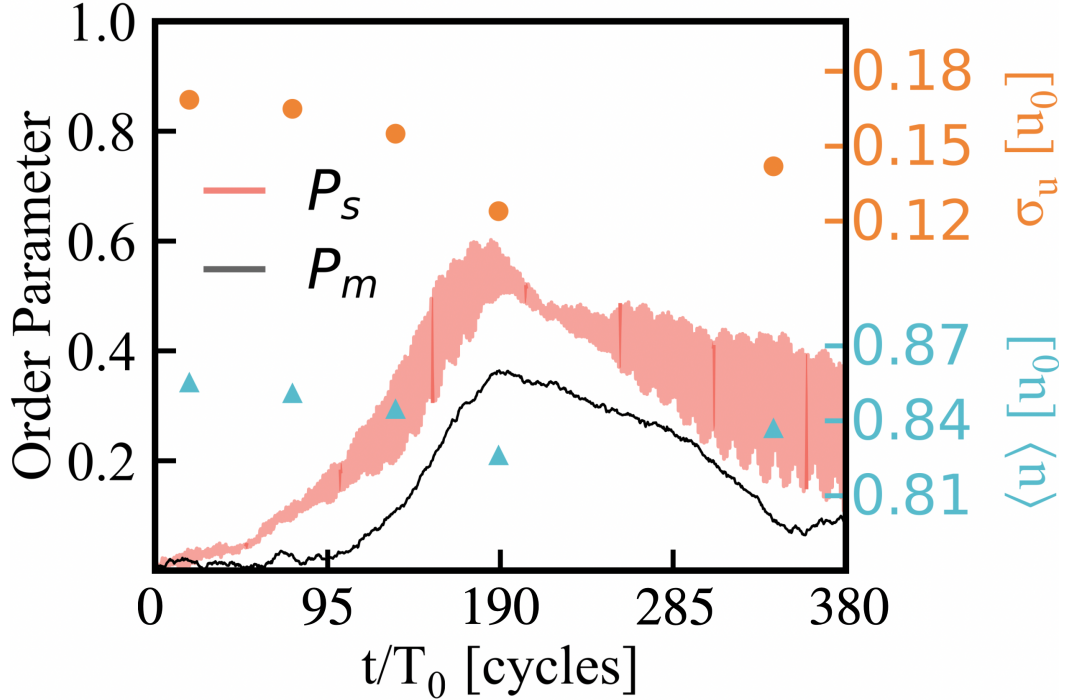


**Figure 4.14. Squirmer velocity analysis for travelling band with local polar order.** Time-evolution of the first  $380T_0$  of the azimuthal  $P_s$  (red) and polar  $P_m$  (black) order parameters of the simulation in Fig. 4.7 with  $a_0 = 4.2$  starting in an isotropic initial configuration. The average particle velocity  $\langle u \rangle$  and velocity fluctuations  $\sigma_u$  at five different points in time are represented by cyan triangles and orange circles respectively.

files we have for the whole simulation).

When compared to the results in Fig. 4.10 for  $a_0 = 8$  and  $N = 689$ , we observe a couple important differences: First, the velocity fluctuations for this case ( $a_0 = 4.2$  and  $N = 4766$ ) do not appear to show a growth before the dip in the order parameter values. In fact, despite the lack of points in the plot, we observe the opposite effect. The five points remain at values in the region of  $\sigma_u \approx 0.12 \dots 0.18$ , and show a similar standard deviation to that of  $\langle u \rangle$ . Both  $\langle u \rangle$  and  $\sigma_u$  evolve in a similar manner, unlike the results in Fig. 4.10. Second, we notice a significantly greater gap between  $P_s$  and  $P_m$ . With the average values having a difference of  $\sim 0.2$ . This is due to the lack of polar order throughout the whole space. While the squirmers show local order of their  $\mathbf{s}$  vectors, their  $\mathbf{m}$  vectors appear to be uncorrelated.

## 4.6 Summary of the observations

The short, exploratory analysis carried in section 4.2 implies that the onset of the post-synchronisation phase separation and its dynamics depend directly on the single particle Reynolds number  $\text{Re}_0$ . Throughout the whole chapter, we have kept the packing fraction constant at  $\phi \approx 0.11$  while other parameters were

varied. In brief, regarding the post-synchronisation phase separation dynamics, we currently have:

- Comparing the orange panels in Fig. 4.2 and 4.3, we notice a decrease in the order parameter fluctuations for smaller  $\text{Re}_0$ . This reflects the direct dependence on  $\text{Re}_0$ .
- Comparing the panels in Fig. 4.3 to each other suggests a dependence of the post-synchronisation phase-separated dynamics on the particle size  $a_0$  and/or the extensivity of the system  $L$  since now  $\text{Re} = \text{const}$  across all three panels.
- Our hypothesis of a collective Reynolds number  $\text{Re}_{\text{coll}} \sim \rho v_{\text{coll}}(L/2)/\mu$ , suggests a dependence on  $L$ .
- In Fig. 4.7 the box length  $L$  is the same while we vary  $a_0$  and  $N$ . Here, we notice much larger post-synchronisation fluctuations for the simulations with smaller particles  $a_0 = 6.3$  and smaller  $\text{Re}_0$  (compared to the case with  $a_0 = 8$ ) despite  $L = \text{const}$ . This implies a dependence of the post-synchronisation phase-separated dynamics on  $a_0$  and/or  $N$  as well (how coarse the cluster is).
- For  $a_0 = 4.2$  in Fig. 4.7, we do not observe phase separation, but instead, a phase propagating wave as the system appears to be divided into two oppositely rotating regions that present no order in the polar direction  $P_m$  (see Fig. 4.13).

We take note that as we change  $a_0$ , the free-particle radius of trajectory  $r_t$ , angular velocity  $\omega_0$ , and therefore rotational Reynolds number  $\text{Re}_\Omega$  change as well. With the limited information we have til now, we refrain from drawing conclusions regarding a dependency on  $r_t$  since there is no clear trend in the response of the system as we change  $r_t$ . In Fig. 4.3  $r_t = \text{const}$  and according to Fig. 4.2 a bigger  $r_t$  would imply larger fluctuations. Whereas in Fig. 4.7 the larger fluctuations are observed for a smaller value of  $r_t$ . As for  $\text{Re}_\Omega$ , throughout this work  $\text{Re}_\Omega \sim 0.01$  whereas  $\text{Re} \sim 0.1$ . Therefore, for the sake of simplicity, we do not take into account the effect of  $\text{Re}_\Omega$  for now.

Finally, in our case study of the post-synchronisation phase separation for the system with  $a_0 = 8$  and  $N = 689$ , we come across strong evidence supporting our hypothesis of the emergence of collective flows; and that the hydrodynamic near-field interactions *can* induce torques on the particles.



## Conclusion

Using hydrodynamic simulations I have investigated suspensions of microswimmers with chiral trajectories at the limit of zero thermal noise.

The results presented in chapters 2 and 3 suggest the emergence of hydrodynamic synchronisation as a naturally occurring collective phenomenon for microswimmers. The predictions should be relevant to a wide variety of experimental systems; such as helically swimming bacteria [42] and sperm [43], or chiral Quincke rollers [113] and spherical ciliates [100], where rotational motion occurs naturally. The synchronisation state diagram in chapter 3 shows how synchronisation can span up to low chiralities, being observed for  $\lambda \approx 0.03 \dots 0.22$  and  $\phi \approx 2.5 \dots 20\%$ , and correspond to biologically relevant values of the parameters. For example, the experimentally observed trajectories of biological swimmers such as *T. thermophila* with  $\lambda = r_t/p \approx 0.05$  in [42] and the 3-dimensional swimming of sperm with  $\lambda \approx 0.15$  in [43].

The observation of the intra-species synchronisation in the racemic mixture, provides a surprising example of two synchronised, interpenetrating, fluids. Further, it demonstrates that synchronisation can be robust as it is maintained in the presence of hydrodynamic fluctuations arising from the source-dipole  $1/r^3$  far-fields. This suggests, that it could be interesting to (re)analyse 3-dimensional correlations in the rotational degrees of freedom in systems exhibiting polar order, such as areas of uniform order in bacterial systems [1–9] or polar flocks in motile colloids [114].

My work shows that the near-field hydrodynamic interactions appear to play a key role in the ordering dynamics of the swimmers. With the random close packing argument for the onset of synchronisation proving to be an effective description for understanding the low- $\phi$  limit of the synchronisation region in the state diagram. The occurrence of the dynamic bottle-neck at the high- $\phi$  limit implies that the near-field hydrodynamic interactions are once again crucial in determining the steady state of the system. I am currently carrying out work in this direction by investigating the number of close contacts a particle experiences at a given time (k-nearest neighbour interactions), and the duration of the interacting and non-interacting time intervals.

With all this in mind, one can expect synchronisation to depend on the shape of the particles. While this work is limited to the study of spherical swimmers, microswimmers in general are not perfectly spherical and in many cases, present elongated shapes. One could expect asymmetrical particles to facilitate synchronisation in some cases, since the synchronised state effectively corresponds to the particles being aligned with high orientational order in the azimuthal and polar directions. This of course would depend on the precise shape of the particles and the orientation of the axes of symmetry relative to the translational and rotational motion. An important consequence of the particles not having

a spherical shape, is that the rotlet term, responsible for the rotational motion of the particle, will in general no longer have a null contribution to the overall flow field generated by the squirmer. Additionally, biological microswimmers do not have smooth surfaces, but rather use the flagella and cilia at their surface for self-propulsion. Taking this into account would increase the complexity of studying these systems, especially when considering the near-field interactions.

Finally, in chapter 4, I report the emergence of post-synchronisation collective phenomena such as phase separation and travelling bands with local polarisation. Despite the results being in a preliminary phase, the analysis so far alludes to the observed phenomena being directly linked to the finite, non-zero, particle Reynolds number ( $Re_0$  in chapter 4). It suggests that the microswimmer Reynolds number plays a critical role in determining the overall dynamics of the system and can give rise to the emergence of complex collective behaviour. The observations could be relevant for biological systems that have Reynolds numbers in the range studied here ( $Re \sim 0.1$ ), such as *Volvox carteri* [115] and plankton [116]. The dynamic behaviour observed in the simulations, could for example help shed light on understanding and predicting the dynamics of plankton blooms [117, 118] — a challenging ecological issue.

These observations, together with the results concerning the racemic mixture of helical swimmers and the various states existing across the synchronisation diagrams — from fully synchronised helical swimming to the partially ordered state displaying only polar alignment — show how the simplicity of Stokes flows can be harnessed to potentially tune the topological flow state of programmable active fluids.



# APPENDIX



.....

## A. Slip velocity profiles of neutral squirmers, shakers, pushers and pullers

Here we give the equations and a visual representation of the slip flow corresponding to the first few modes ( $n = 2$  and  $m = 2$ ) of the generalised squirmer model using Wolfram Mathematica [90]. Additionally, we show how these modes can be used to “construct” the 4 main types of squirmer: neutral squirmers, pushers, pullers and shakers. The colour scheme and size of the arrows in the surface of the squirmer reflect the intensity of the slip-flow. We normalise the magnitude of the velocity profiles by their maximum value in each case to have a full spectrum of colours (in the “rainbow” colour scheme) ranging from: 0 (blue) to 1 (red). The *local* axis coordinate tripod has exactly the same orientation throughout and is only shown for the first image.

Using Lamb’s general solution in spherical coordinates for purely tangential deformation ( $u$ ) on the surface of a spherical particle given in [83]; we have:

$$u_r|_{r=a} = 0 \tag{A.1}$$

$$u_\theta|_{r=a} = \sum_{n=1}^{\infty} \sum_{m=0}^n \left[ \frac{-2 \sin\theta P_n^{m'}}{na^{n+2}} (B_{mn} \cos m\phi + \tilde{B}_{mn} \sin m\phi) + \frac{m P_n^m}{a^{n+1} \sin\theta} (\tilde{C}_{mn} \cos m\phi - C_{mn} \sin m\phi) \right] \tag{A.2}$$

$$u_\phi|_{r=a} = \sum_{n=1}^{\infty} \sum_{m=0}^n \left[ \frac{\sin\theta P_n^{m'}}{a^{n+1}} (C_{mn} \cos m\phi + \tilde{C}_{mn} \sin m\phi) + \frac{2m P_n^m}{na^{n+2} \sin\theta} (\tilde{B}_{mn} \cos m\phi - B_{mn} \sin m\phi) \right] \tag{A.3}$$

where  $P_n^m = P_n^m(x)$ , with  $x = \cos\theta$ .

Just for the sake of completion, the overall flow field is given by:

$$\mathbf{v} = \mathbf{u} + \mathbf{u}_T + \mathbf{u}_R \tag{A.4}$$

where  $\mathbf{u} = u_r \mathbf{e}_r + u_\theta \mathbf{e}_\theta + u_\phi \mathbf{e}_\phi$  is the solution of the pumping problem and  $\mathbf{u}_T, \mathbf{u}_R$  are the flows due to the induced translation ( $\mathbf{U}$ ) and rotation ( $\mathbf{\Omega}$ ).

## A.1 $n = 1$

$\mathbf{n}=1, \mathbf{m}=0$

$$P_1^0 = x = \cos\theta, \quad P_1^{0'} = 1 \quad (\text{A.5})$$

$$u_\theta = -\frac{2 \sin\theta}{a^3} B_{01} \quad (\text{A.6})$$

$$u_\phi = \frac{\sin\theta}{a^2} C_{01} \quad (\text{A.7})$$

where equation (A.6) corresponds to a **source dipole (neutral squirmer)**, and equation (A.7) to a **rotlet** and does not contribute to the overall flow field  $\mathbf{v}$  because it cancels out with the flow field due to the induced rotation  $\mathbf{u}_\Omega$ .

By using the re-scaling:

$$B_{0n} = -\frac{a^{n+2}}{n+1} B_n \quad (\text{A.8})$$

equation (A.6) becomes:

$$u_\theta = \sin\theta B_1 \quad (\text{A.9})$$

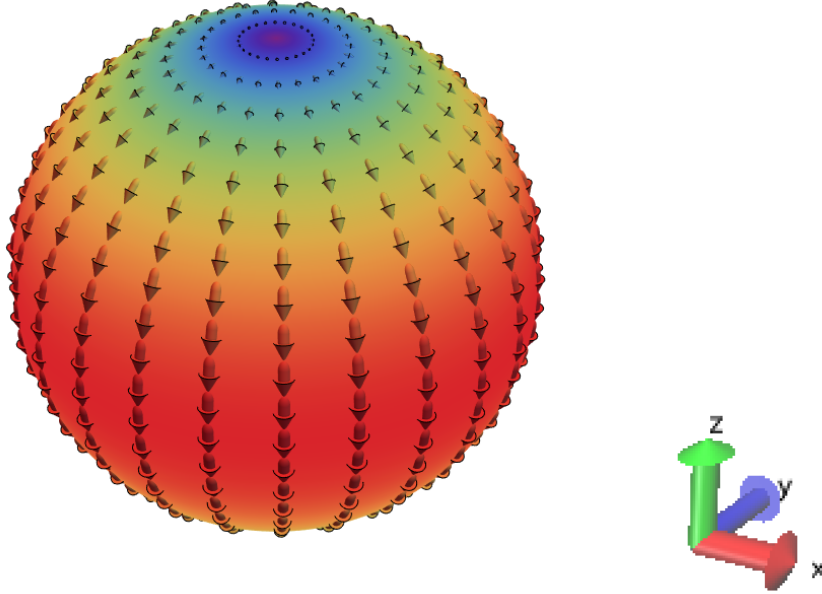


**Figure A.1. Classic neutral squirmer.**  $\mathbf{n}=1, \mathbf{m}=0$ . A source dipole (neutral squirmer) in the  $\mathbf{z}$ -direction.

$\mathbf{n}=1, \mathbf{m}=1$

$$P_1^1 = -\sqrt{1-x^2} = -\sin\theta, \quad P_1^{1'} = \frac{x}{\sqrt{1-x^2}} = \frac{\cos\theta}{\sin\theta} \quad (\text{A.10})$$

$$u_\theta = -\frac{2 \cos\theta}{a^3} (B_{11} \cos\phi + \tilde{B}_{11} \sin\phi) - \frac{1}{a^2} (\tilde{C}_{11} \cos\phi - C_{11} \sin\phi) \quad (\text{A.11})$$

$$u_\phi = \frac{\cos\theta}{a^2}(C_{11} \cos\phi + \tilde{C}_{11} \sin\phi) - \frac{2}{a^3}(\tilde{B}_{11} \cos\phi - B_{11} \sin\phi) \quad (\text{A.12})$$

Similarly to the  $\mathbf{n}=1$ ,  $\mathbf{m}=0$  case, the  $B_{11}/\tilde{B}_{11}$  and  $C_{11}/\tilde{C}_{11}$  modes in equations (A.11) and (A.12) correspond to **source dipoles** and **rotlets** respectively, in the  $x/y$  directions (with the rotlets not contributing to the overall flow field for the same reason explained above).

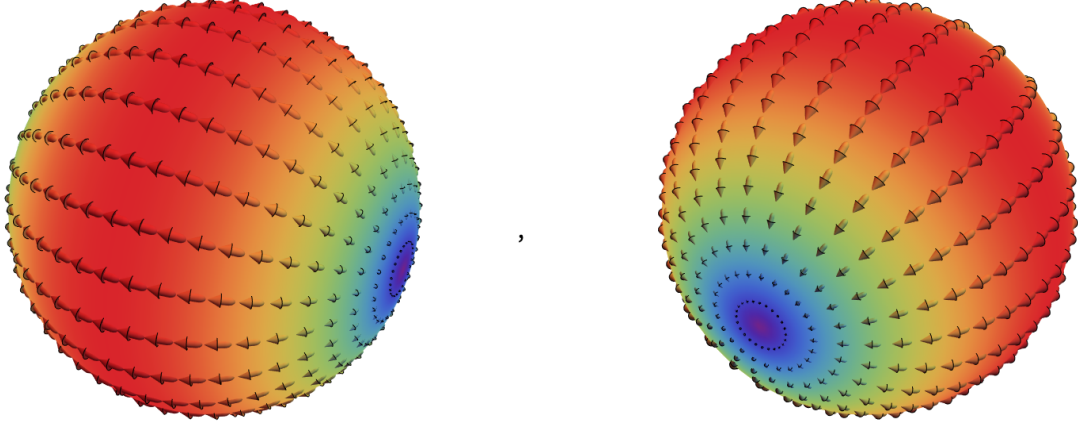


**Figure A.2. Neutral squirmers in x and y directions.**  $\mathbf{n}=1$ ,  $\mathbf{m}=1$ . Source dipoles (neutral squirmers) in the  $\mathbf{x}$  and  $\mathbf{y}$  directions. Left:  $B_{11}$  mode. Right:  $\tilde{B}_{11}$  mode.

## A.2 $n = 2$

$\mathbf{n}=2$ ,  $\mathbf{m}=0$

$$P_2^0 = x = \frac{(3x^2 - 1)}{2}, \quad P_2^{0'} = 3x = 3 \cos\theta \quad (\text{A.13})$$

$$u_\theta = -\frac{3 \sin\theta \cos\theta}{a^4} B_{02} = -\frac{3 \sin 2\theta}{2a^4} B_{02} \quad (\text{A.14})$$

$$u_\phi = \frac{3 \sin\theta \cos\theta}{a^3} C_{02} = \frac{3 \sin 2\theta}{2a^3} C_{02} \quad (\text{A.15})$$

Equation (A.15) corresponds to a **rotlet dipole** and is the leading-order mode in the azimuthal direction ( $\mathbf{e}_\phi$ ) contributing to the overall flow field  $\mathbf{v}$ .

By re-scaling (equation (A.8)), equation (A.14) becomes:

$$u_\theta = \frac{\sin 2\theta}{2} B_2 \quad (\text{A.16})$$

which corresponds to a **stresslet** in the  $\mathbf{z}$ -direction (a shaker),  $\mathbf{S}(\mathbf{e}_z, \mathbf{e}_z)$ , and allows us to define **pushers** and **pullers** ( $\beta = B_2/B_1$ ).

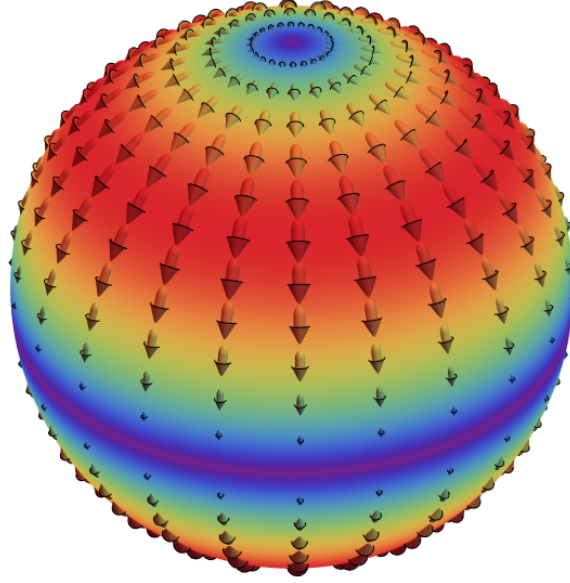


**Figure A.3. Classic shaker.**  $n=2, m=0$ . A stresslet ( $B_2$  mode) in the  $z$ -direction

$n=2, m=1$

$$P_2^1 = -3x\sqrt{1-x^2} = -3\cos\theta\sin\theta, \quad P_2^{1'} = -3\sqrt{1-x^2} + \frac{3x^2}{\sqrt{1-x^2}} = 3\left(\frac{\cos^2\theta}{\sin\theta} - \sin\theta\right) \quad (\text{A.17})$$

$$u_\theta = \frac{3(2\sin^2\theta - 1)}{a^4}(B_{12}\cos\phi + \tilde{B}_{12}\sin\phi) - \frac{3\cos\theta}{a^3}(\tilde{C}_{12}\cos\phi - C_{12}\sin\phi) \quad (\text{A.18})$$

$$u_\phi = \frac{3(2\sin^2\theta - 1)}{a^3}(C_{12}\cos\phi + \tilde{C}_{12}\sin\phi) - \frac{3\cos\theta}{a^4}(\tilde{B}_{12}\cos\phi - B_{12}\sin\phi) \quad (\text{A.19})$$

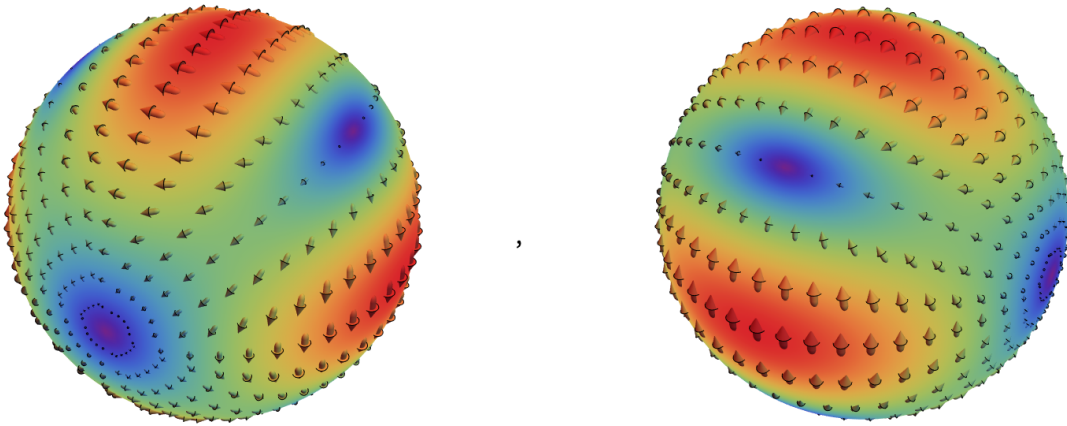


**Figure A.4. The  $B_{21}$  and  $\tilde{B}_{21}$  modes.**  $n=2, m=1$ . Left:  $B_{21}$  mode. Right:  $\tilde{B}_{21}$  mode.

$\mathbf{n}=2, \mathbf{m}=2$

$$P_2^2 = 3(1 - x^2) = 3 \sin^2 \theta, \quad P_2^{2'} = -6x = -6 \cos \theta \quad (\text{A.20})$$

$$\begin{aligned} u_\theta &= \frac{6 \cos \theta \sin \theta}{a^4} (B_{22} \cos 2\phi + \tilde{B}_{22} \sin 2\phi) + \frac{6 \sin \theta}{a^3} (\tilde{C}_{22} \cos 2\phi - C_{22} \sin 2\phi) \\ &= \frac{3 \sin 2\theta}{a^4} (B_{22} \cos 2\phi + \tilde{B}_{22} \sin 2\phi) + \frac{6 \sin \theta}{a^3} (\tilde{C}_{22} \cos 2\phi - C_{22} \sin 2\phi) \end{aligned} \quad (\text{A.21})$$

$$\begin{aligned} u_\phi &= -\frac{6 \cos \theta \sin \theta}{a^3} (C_{22} \cos 2\phi + \tilde{C}_{22} \sin 2\phi) + \frac{6 \sin \theta}{a^4} (\tilde{B}_{22} \cos 2\phi - B_{22} \sin 2\phi) \\ &= -\frac{3 \sin 2\theta}{a^3} (C_{22} \cos 2\phi + \tilde{C}_{22} \sin 2\phi) + \frac{6 \sin \theta}{a^4} (\tilde{B}_{22} \cos 2\phi - B_{22} \sin 2\phi) \end{aligned} \quad (\text{A.22})$$

Here, in equations (A.18), (A.19), (A.21), (A.22), the  $B_{m2}/\tilde{B}_{m2}$  and  $C_{m2}/\tilde{C}_{m2}$  terms with  $m = 1, 2$ ; correspond to **stresslets** and **rotlet dipoles** respectively, in different orientations.

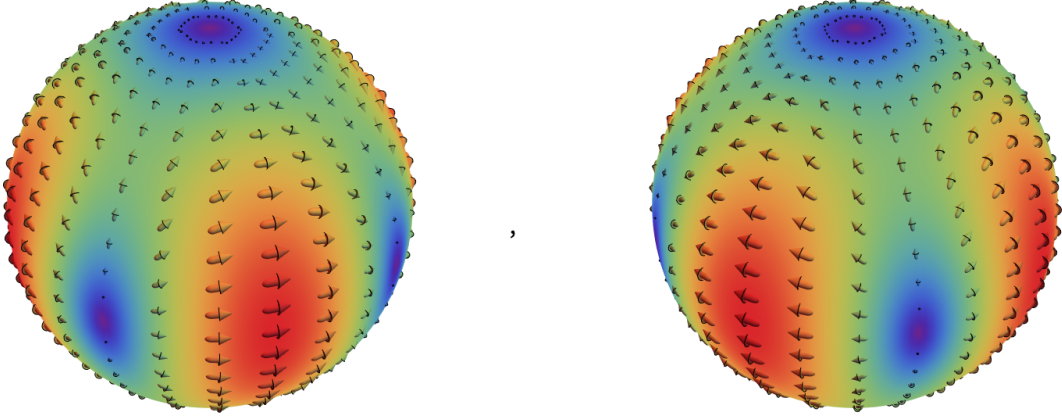


**Figure A.5. The  $B_{22}$  mode.**  $\mathbf{n}=2, \mathbf{m}=2$ . Left:  $B_{22}$  mode. Right:  $\tilde{B}_{22}$  mode.

### A.3 Forming Pullers and Pushers:

Similarly to (A.8), we introduce the following re-scaling:

$$B_{mn} = \frac{a^{n+2}}{n+1} B_{nm} \quad , \quad (m \neq 0) \quad (\text{A.23})$$

The stresslets in the  $\mathbf{x}$ ,  $\mathbf{y}$  directions can be obtained by combining modes  $B_2$  and  $B_{22}$  and choosing  $B_2 = B_{22}$ :

$$\mathbf{S}(\mathbf{e}_x, \mathbf{e}_x) = B_{22} \left[ -mode(B_2) - \frac{mode(B_{22})}{2} \right] \quad (\text{A.24})$$

$$\mathbf{S}(\mathbf{e}_x, \mathbf{e}_x)u_\theta = B_{22} \left[ -\frac{\sin 2\theta}{2} - \frac{\sin 2\theta \cos 2\phi}{2} \right] \quad (\text{A.25})$$

$$\mathbf{S}(\mathbf{e}_x, \mathbf{e}_x)u_\phi = B_{22} \sin \theta \sin 2\phi \quad (\text{A.26})$$

$$\mathbf{S}(\mathbf{e}_y, \mathbf{e}_y) = B_{22} \left[ -mode(B_2) + \frac{mode(B_{22})}{2} \right] \quad (\text{A.27})$$

$$\mathbf{S}(\mathbf{e}_y, \mathbf{e}_y)u_\theta = B_{22} \left[ -\frac{\sin 2\theta}{2} + \frac{\sin 2\theta \cos 2\phi}{2} \right] \quad (\text{A.28})$$

$$\mathbf{S}(\mathbf{e}_y, \mathbf{e}_y)u_\phi = -B_{22} \sin \theta \sin 2\phi \quad (\text{A.29})$$

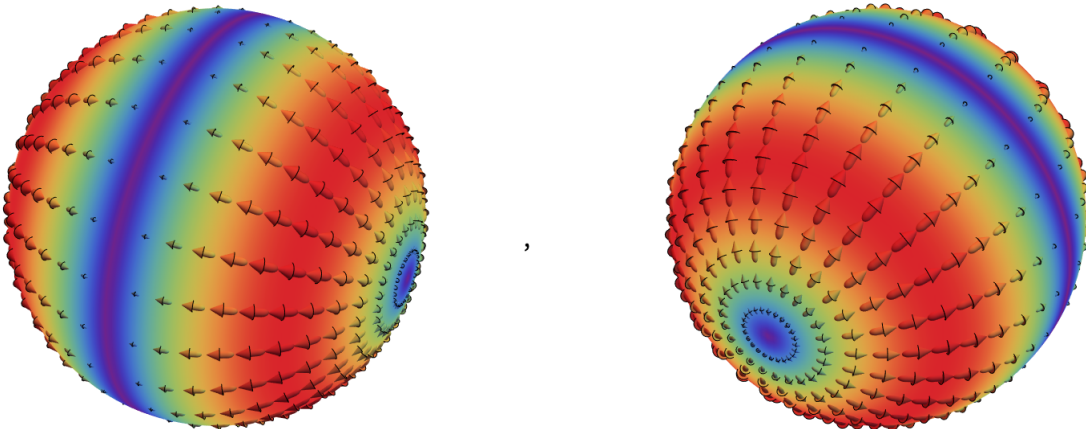


**Figure A.6. Shakers in the  $\mathbf{x}$  and  $\mathbf{y}$  directions.** Stresslets in the  $\mathbf{x}$  and  $\mathbf{y}$  directions. Left:  $\mathbf{S}(\mathbf{e}_x, \mathbf{e}_x)$ . Right:  $\mathbf{S}(\mathbf{e}_y, \mathbf{e}_y)$ .

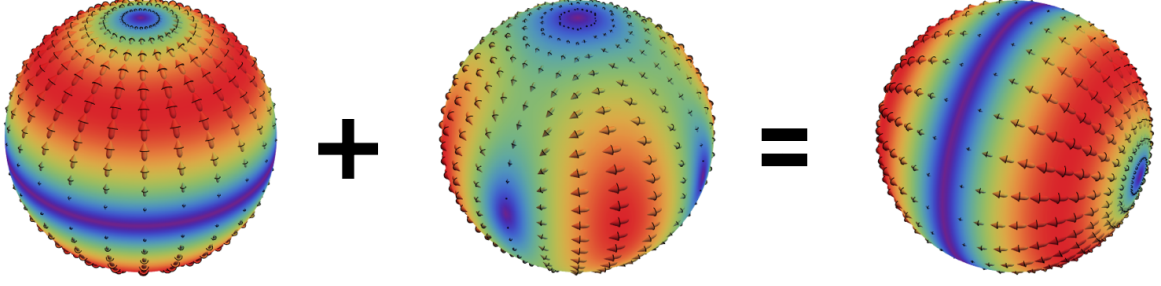


Figure A.7. Building a shaker (stresslet) in the x direction.

$$-mode(B_2) - \frac{mode(B_{22})}{2} = \mathbf{S}(\mathbf{e}_x, \mathbf{e}_x)$$

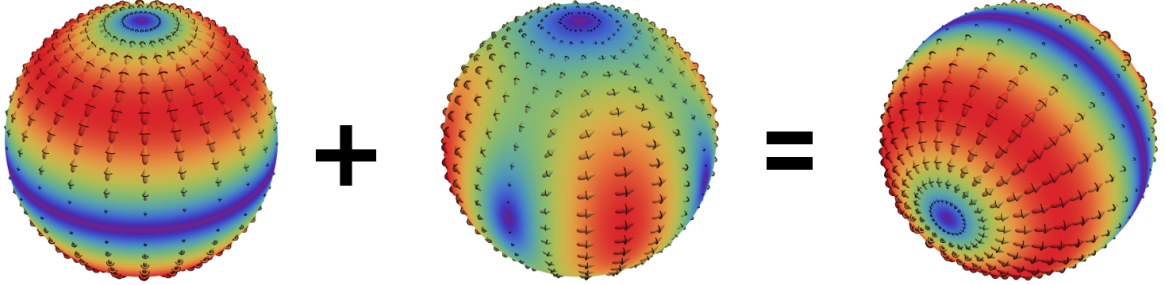


Figure A.8. Building a shaker (stresslet) in the x direction.

$$-mode(B_2) + \frac{mode(B_{22})}{2} = \mathbf{S}(\mathbf{e}_y, \mathbf{e}_y)$$

By combining the source dipoles (modes  $B_1$ ,  $B_{11}$  and  $\tilde{B}_{11}$ ) with their corresponding stresslets we can form pullers and pushers:

$$Puller_z = mode(B_1) + \mathbf{S}(\mathbf{e}_z, \mathbf{e}_z) = mode(B_1) + mode(B_2) \quad (\text{A.30})$$

$$Pusher_z = mode(B_1) - \mathbf{S}(\mathbf{e}_z, \mathbf{e}_z) = mode(B_1) - mode(B_2) \quad (\text{A.31})$$

$$Puller_z u_\theta = B_1 \sin\theta + B_2 \frac{\sin 2\theta}{2} \quad (\text{A.32})$$

$$Puller_z u_\phi = 0 \quad (\text{A.33})$$

$$Pusher_z u_\theta = B_1 \sin\theta - B_2 \frac{\sin 2\theta}{2} \quad (\text{A.34})$$

$$Pusher_z u_\phi = 0 \quad (\text{A.35})$$

$$Puller_x = mode(B_{11}) + \mathbf{S}(\mathbf{e}_x, \mathbf{e}_x) = mode(B_{11}) - mode(B_2) - \frac{mode(B_{22})}{2} \quad (\text{A.36})$$

$$Pusher_x = mode(B_{11}) - \mathbf{S}(\mathbf{e}_x, \mathbf{e}_x) = mode(B_{11}) + mode(B_2) + \frac{mode(B_{22})}{2} \quad (\text{A.37})$$

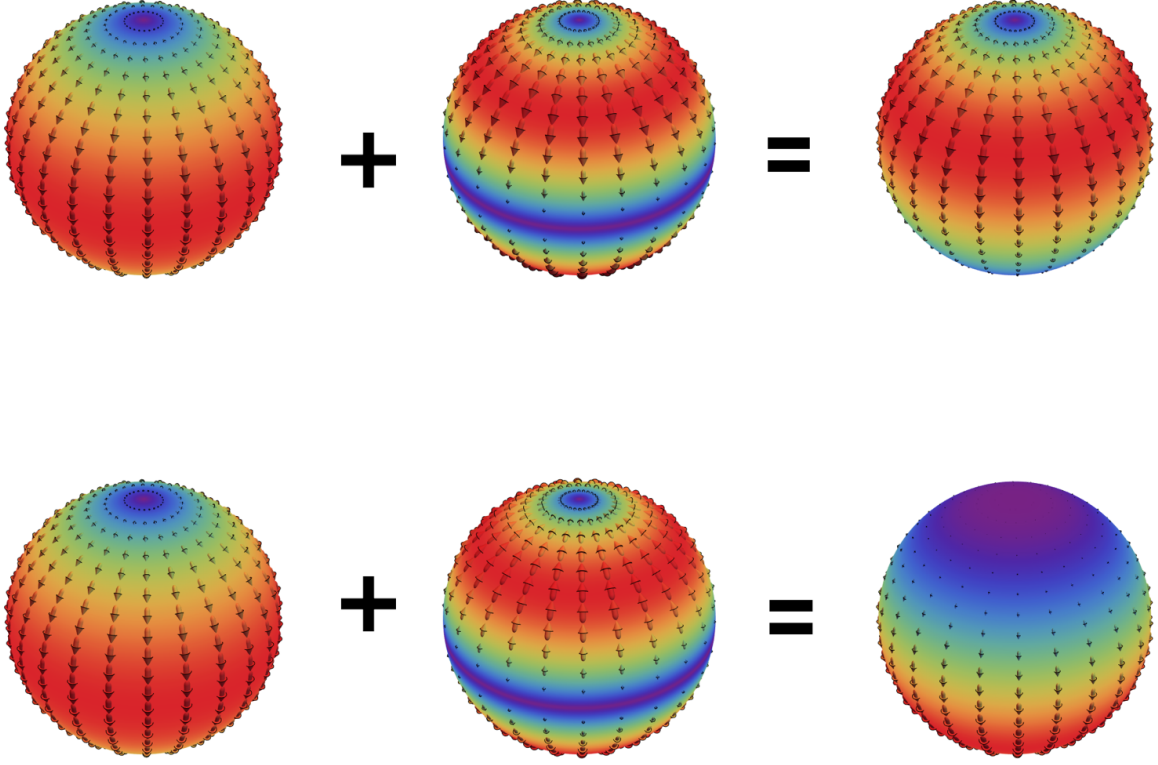


**Figure A.9. Building a classic puller and pusher.**

Top:  $mode(B_1) + mode(B_2) = Puller_z$ .

Bottom:  $mode(B_1) + [-mode(B_2)] = Pusher_z$ .

$$Puller_x u_\theta = -B_{11} \cos\theta \cos\phi - B_{22} \frac{\sin 2\theta}{2} - B_{22} \frac{\sin 2\theta \cos 2\phi}{2} \quad (A.38)$$

$$Puller_x u_\phi = B_{11} \sin\phi + B_{22} \sin\theta \sin 2\phi \quad (A.39)$$

$$Pusher_x u_\theta = -B_{11} \cos\theta \cos\phi + B_{22} \frac{\sin 2\theta}{2} + B_{22} \frac{\sin 2\theta \cos 2\phi}{2} \quad (A.40)$$

$$Pusher_x u_\phi = B_{11} \sin\phi - B_{22} \sin\theta \sin 2\phi \quad (A.41)$$

$$Puller_y = mode(\tilde{B}_{11}) + \mathbf{S}(\mathbf{e}_y, \mathbf{e}_y) = mode(\tilde{B}_{11}) - mode(B_2) + \frac{mode(B_{22})}{2} \quad (A.42)$$

$$Pusher_y = mode(\tilde{B}_{11}) - \mathbf{S}(\mathbf{e}_y, \mathbf{e}_y) = mode(\tilde{B}_{11}) + mode(B_2) - \frac{mode(B_{22})}{2} \quad (A.43)$$

$$Puller_y u_\theta = -\tilde{B}_{11} \cos\theta \sin\phi - B_{22} \frac{\sin 2\theta}{2} + B_{22} \frac{\sin 2\theta \cos 2\phi}{2} \quad (A.44)$$

$$Puller_y u_\phi = -\tilde{B}_{11} \cos\phi - B_{22} \sin\theta \sin 2\phi \quad (A.45)$$

$$Pusher_y u_\theta = -\tilde{B}_{11} \cos\theta \sin\phi + B_{22} \frac{\sin 2\theta}{2} - B_{22} \frac{\sin 2\theta \cos 2\phi}{2} \quad (A.46)$$

$$Pusher_y u_\phi = -\tilde{B}_{11} \cos\phi + B_{22} \sin\theta \sin 2\phi \quad (A.47)$$

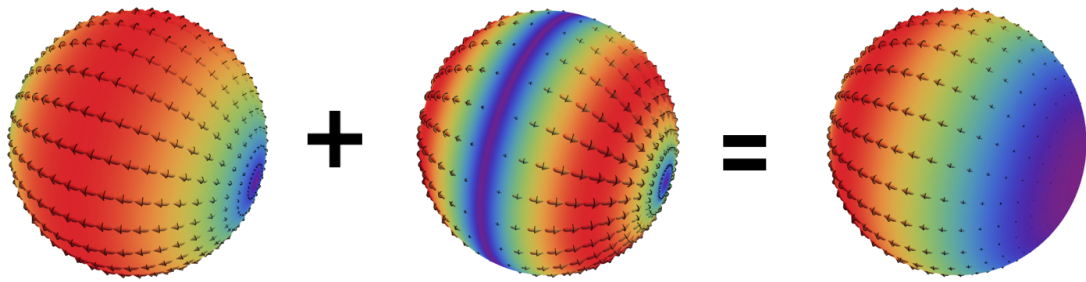
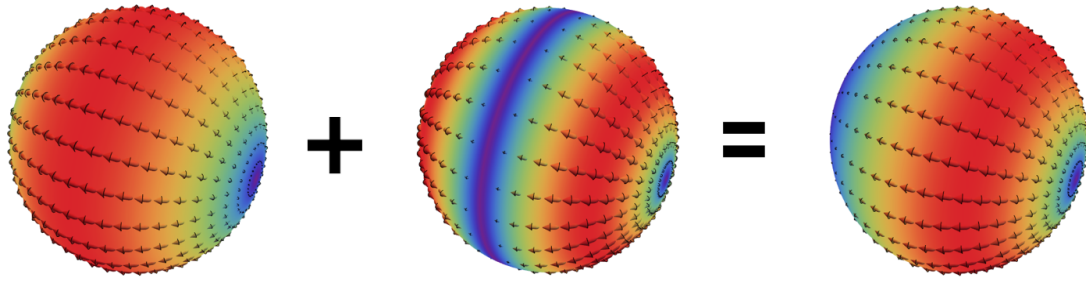


Figure A.10. Building a puller and pusher in the x direction.  
 Top:  $mode(B_{11}) + \mathbf{S}(\mathbf{e}_x, \mathbf{e}_x) = Puller_x$ . Bottom:  $mode(B_{11}) + [-\mathbf{S}(\mathbf{e}_x, \mathbf{e}_x)] = Pusher_x$ .

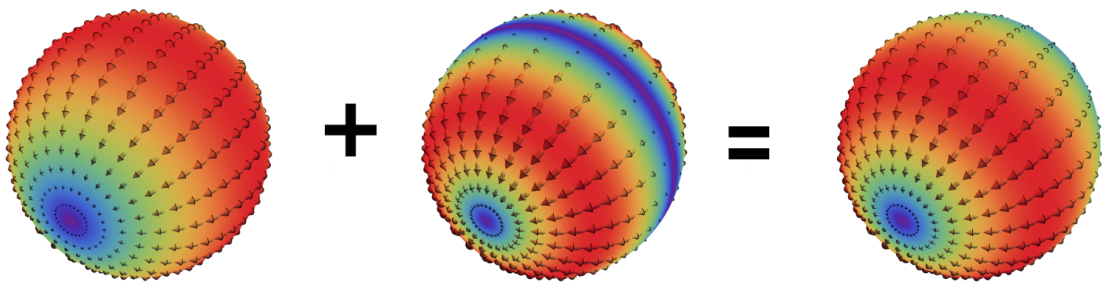
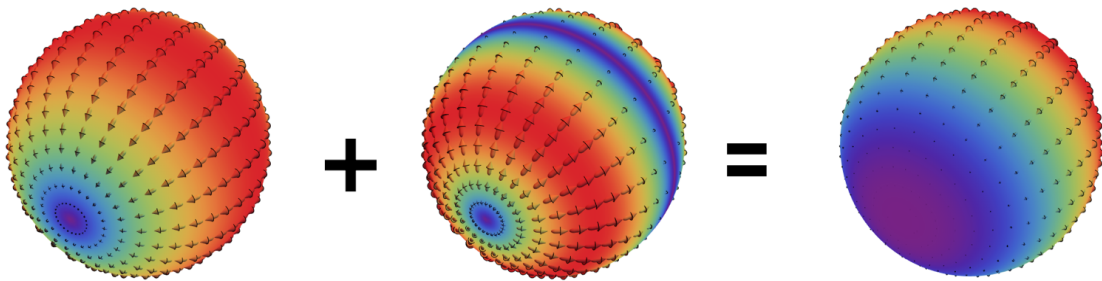


Figure A.11. Building a puller and pusher in the y direction.  
 Top:  $mode(\tilde{B}_{11}) + \mathbf{S}(\mathbf{e}_y, \mathbf{e}_y) = Puller_y$ . Bottom:  $mode(\tilde{B}_{11}) + [-\mathbf{S}(\mathbf{e}_y, \mathbf{e}_y)] = Pusher_y$ .



.....

## B. Translational and Angular Velocity of Self-Propelling Particles

Here we use the reciprocal theorem for Stokes flows [89] to calculate the resulting bulk swimming velocity  $\mathbf{U}$  and angular velocity  $\mathbf{\Omega}$  of a particle, due to a slip flow (disturbance motion)  $\mathbf{u}'$  at the surface, corresponding to different cases of slip flow that were initially of interest to us. For each case, we begin with the corresponding  $\mathbf{u}'$ .

$$\mathbf{U}(\mathbf{t}) = -\frac{1}{4\pi R^2} \int_S \mathbf{u}' dS \tag{B.1}$$

$$\mathbf{\Omega}(\mathbf{t}) = -\frac{3}{8\pi R^3} \int_S \mathbf{n} \times \mathbf{u}' dS \tag{B.2}$$

with  $\mathbf{n} = \hat{\mathbf{e}}_r$  normal to  $S$  and:

$$dS = R^2 \sin\theta d\theta d\phi \tag{B.3}$$

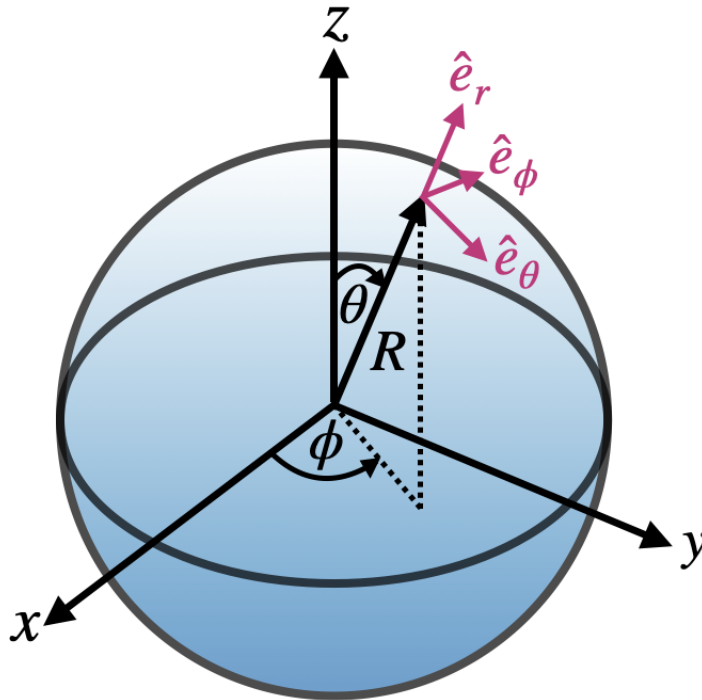


Figure B.1. Local spherical coordinate system for a squirmer of radius  $R$ .

## B.1 Classic squirmer model: $\mathbf{u}' = \sin\theta(b_1 + b_2 \cos\theta) \hat{\mathbf{e}}_\theta$

$$\mathbf{U} = -\frac{R^2}{4\pi R^2} \int_0^\pi \int_0^{2\pi} (b_1 \sin\theta + b_2 \sin\theta \cos\theta)(\cos\theta \cos\phi, \cos\theta \sin\phi, -\sin\theta) \sin\theta d\theta d\phi \quad (\text{B.4})$$

Treating each component separately:

$$U_x = -\frac{1}{4\pi} \int_0^\pi \int_0^{2\pi} (b_1 \sin^2\theta \cos\theta \cos\phi + b_2 \sin^2\theta \cos^2\theta \cos\phi) d\theta d\phi \quad (\text{B.5})$$

$$U_y = -\frac{1}{4\pi} \int_0^\pi \int_0^{2\pi} (b_1 \sin^2\theta \cos\theta \sin\phi + b_2 \sin^2\theta \cos^2\theta \sin\phi) d\theta d\phi \quad (\text{B.6})$$

$$U_z = -\frac{1}{4\pi} \int_0^\pi \int_0^{2\pi} (-b_1 \sin^3\theta - b_2 \sin^3\theta \cos\theta) d\theta d\phi \quad (\text{B.7})$$

When integrating for  $\phi$  from 0 to  $2\pi$ , equations (B.5) and (B.6) will give 0 since we have the functions  $\sin\phi$  and  $\cos\phi$ . Therefore:  $\mathbf{U} = U_z \hat{\mathbf{z}}$ .

where:

$$\int \sin^3\alpha d\alpha = \frac{1}{12}(\cos(3\alpha) - 9 \cos\alpha) + C \quad (\text{B.8})$$

$$\int \sin^3\alpha \cos\alpha d\alpha = \frac{\sin^4\alpha}{4} + C \quad (\text{B.9})$$

therefore:

$$\mathbf{U} = U_z \hat{\mathbf{z}} = -\frac{1}{4\pi} \left( 0, 0, -2\pi b_1 \left( \frac{1}{12}(\cos(3\theta) - 9 \cos\theta) \Big|_0^\pi \right) - 2\pi b_2 \left( \frac{\sin^4\theta}{4} \Big|_0^\pi \right) \right) \quad (\text{B.10})$$

$$\mathbf{U} = \left( 0, 0, \frac{2\pi b_1}{4\pi} \cdot \frac{4}{3} \right) = \left( 0, 0, \frac{2b_1}{3} \right) = \frac{2b_1}{3} \hat{\mathbf{z}} \quad (\text{B.11})$$

And for the angular velocity:

$$\boldsymbol{\Omega} = -\frac{3R^2}{8\pi R^3} \int_0^\pi \int_0^{2\pi} \|\hat{\mathbf{e}}_r\| \|\mathbf{u}'\| \sin\alpha \hat{\mathbf{e}}_\phi \sin\theta d\theta d\phi \quad (\text{B.12})$$

$$\boldsymbol{\Omega} = -\frac{3}{8\pi R} \int_0^\pi \int_0^{2\pi} \sin^2\theta (b_1 + b_2 \cos\theta) (-\sin\phi, \cos\phi, 0) d\theta d\phi \quad (\text{B.13})$$

Since the dependence on  $\phi$  in the non-zero components is of the type  $\sin\phi$  or  $\cos\phi$ , the angular velocity in these directions will be zero ( $\Omega_x = \Omega_y = 0$ ). Therefore, for the classic squirmer model we find:  $\boldsymbol{\Omega} = 0$ .

## B.2 $\mathbf{u}' = b_2 \cos\phi \hat{\mathbf{e}}_\phi$

$$\hat{\mathbf{e}}_\phi = -\sin\phi \hat{\mathbf{x}} + \cos\phi \hat{\mathbf{y}} = (-\sin\phi, \cos\phi, 0) \quad (\text{B.14})$$

$$\mathbf{U} = -\frac{R^2}{4\pi R^2} \int_0^\pi \int_0^{2\pi} b_2 \cos\phi (-\sin\phi, \cos\phi, 0) \sin\theta d\theta d\phi \quad (\text{B.15})$$

$$\mathbf{U} = -\frac{1}{4\pi} \int_0^\pi \int_0^{2\pi} (-b_2 \cos\phi \sin\phi \sin\theta, b_2 \cos^2\phi \sin\theta, 0) d\theta d\phi \quad (\text{B.16})$$

$$\mathbf{U} = -\frac{-b_2 \cos\theta \Big|_0^\pi}{4\pi} \int_0^{2\pi} (-\cos\phi \sin\phi, \cos^2\phi, 0) d\phi \quad (\text{B.17})$$

where:

$$\int \cos\alpha \sin\alpha d\alpha = -\frac{\cos^2\alpha}{2} + C \quad (\text{B.18})$$

$$\int \cos^2\alpha d\alpha = \frac{1}{2}(\alpha + \sin\alpha \cos\alpha) + C \quad (\text{B.19})$$

therefore:

$$\mathbf{U} = -\frac{2b_2}{4\pi} \left( -\frac{\cos^2\phi}{2} \Big|_0^{2\pi}, \frac{1}{2}(\phi + \sin\phi \cos\phi) \Big|_0^{2\pi}, 0 \right) = -\frac{b_2}{2\pi}(0, \pi, 0) \quad (\text{B.20})$$

$$\mathbf{U} = -\frac{b_2}{2} \hat{\mathbf{y}} \quad (\text{B.21})$$

## B.3 $\mathbf{u}' = \sin\theta b_2 \cos\phi \hat{\mathbf{e}}_\phi$

$$\mathbf{U} = -\frac{R^2}{4\pi R^2} \int_0^\pi \int_0^{2\pi} \sin\theta \cdot b_2 \cos\phi (-\sin\phi, \cos\phi, 0) \sin\theta d\theta d\phi \quad (\text{B.22})$$

$$\mathbf{U} = -\frac{1}{4\pi} \int_0^\pi \int_0^{2\pi} (-b_2 \cos\phi \sin\phi \sin^2\theta, b_2 \cos^2\phi \sin^2\theta, 0) d\theta d\phi \quad (\text{B.23})$$

where:

$$\int \sin^2\alpha d\alpha = \int (1 - \cos^2\alpha) d\alpha = \frac{1}{2}(\alpha - \sin\alpha \cos\alpha) + C \quad (\text{B.24})$$

therefore:

$$\mathbf{U} = -\frac{\frac{b_2}{2}(\theta - \sin\theta \cos\theta) \Big|_0^\pi}{4\pi} \int_0^{2\pi} (-\cos\phi \sin\phi, \cos^2\phi, 0) d\phi \quad (\text{B.25})$$

and using equations (B.18) and (B.19):

$$\mathbf{U} = -\frac{b_2\pi}{4\pi} \left( \frac{\cos^2\alpha}{2} \Big|_0^{2\pi}, \frac{1}{2}(\phi + \sin\phi \cos\phi) \Big|_0^{2\pi}, 0 \right) = -\frac{b_2}{8}(0, \pi, 0) \quad (\text{B.26})$$

$$\mathbf{U} = -\frac{b_2\pi}{8} \hat{\mathbf{y}} \approx -(0.39 \cdot b_2) \hat{\mathbf{y}} \quad (\text{B.27})$$



Therefore we have:

$$\mathbf{U} = -\frac{b_2}{8} \int_0^{2\pi} (-\sin\phi \cos(n\phi), \cos\phi \cos(n\phi), 0) d\phi \quad (\text{B.31})$$

Given the symmetry properties of the sine and cosine functions,  $\sin(x) \cos(nx)$ ,  $\cos(x) \cos(nx)$  and  $\sin(x) \sin(nx)$  will have a period  $P = \pi$  for odd values of  $n$  ( $n = 1, 3, 5, \dots$ ) and  $P = 2\pi$  for even values of  $n$  ( $n = 0, 2, 4, \dots$ ). With  $\cos^2(x) \geq 0$  and  $\sin^2(x) \geq 0$  (for  $n = 1$ ) corresponding to the only cases in which the area between the curve and the X-axis will be different from 0 for an interval of size  $L = mP$  ( $m = 1, 2, 3, \dots$ ).

Therefore  $\mathbf{U} \neq 0$  only for  $n = 1$ , which corresponds to the solution given previously in part **2**:

$$\mathbf{U} = -\frac{b_2\pi}{8} \hat{\mathbf{y}} \approx -(0.39 b_2) \hat{\mathbf{y}} \quad (\text{B.32})$$

As for the angular velocity:

$$\boldsymbol{\Omega} = -\frac{3R^2}{8\pi R^3} \int_0^\pi \int_0^{2\pi} \|\hat{\mathbf{e}}_r\| \|\mathbf{u}'\| \sin\alpha \hat{\mathbf{e}}_\theta \sin\theta d\theta d\phi \quad (\text{B.33})$$

where  $\alpha$  is the angle between  $\hat{\mathbf{e}}_r$  and  $\mathbf{u}'$  in the plane containing them and:

$$\hat{\mathbf{e}}_\theta = \cos\theta \cos\phi \hat{\mathbf{x}} + \cos\theta \sin\phi \hat{\mathbf{y}} - \sin\theta \hat{\mathbf{z}} = (\cos\theta \cos\phi, \cos\theta \sin\phi, -\sin\theta) \quad (\text{B.34})$$

$$\boldsymbol{\Omega} = -\frac{3}{8\pi R^3} \int_0^\pi \int_0^{2\pi} \sin^2\theta (b_1 + b_2 \cos(n\phi)) (\cos\theta \cos\phi, \cos\theta \sin\phi, -\sin\theta) d\theta d\phi \quad (\text{B.35})$$

Taking each component separately:

$$\Omega_x = -\frac{3}{8\pi R} \int_0^\pi \sin^2\theta \cos\theta d\theta \int_0^{2\pi} (b_1 + b_2 \cos(n\phi)) \cos\phi d\phi \quad (\text{B.36})$$

$$\Omega_y = -\frac{3}{8\pi R} \int_0^\pi \sin^2\theta \cos\theta d\theta \int_0^{2\pi} (b_1 + b_2 \cos(n\phi)) \sin\phi d\phi \quad (\text{B.37})$$

$$\Omega_z = \frac{3}{8\pi R} \int_0^\pi \sin^3\theta d\theta \int_0^{2\pi} (b_1 + b_2 \cos(n\phi)) d\phi \quad (\text{B.38})$$

where:

$$\int \sin^2\alpha \cos\alpha d\alpha = \frac{\sin^3\alpha}{3} + C \quad (\text{B.39})$$

$$\int \sin^3\alpha d\alpha = \frac{1}{12}(\cos(3\alpha) - 9\cos\alpha) + C \quad (\text{B.40})$$

From equation (B.39) we see that the  $\mathbf{x}$  and  $\mathbf{y}$  components of  $\boldsymbol{\Omega}$  will be equal to 0 and thus  $\boldsymbol{\Omega} = \Omega_z \hat{\mathbf{z}}$ :

$$\boldsymbol{\Omega} = \frac{3}{8\pi R} \left( 0, 0, \left( \frac{1}{12}(\cos(3\phi) - 9\cos\phi) \Big|_0^\pi \right) \left( 2\pi b_1 + b_2 \frac{\sin(n\phi)}{n} \Big|_0^{2\pi} \right) \right) \quad (\text{B.41})$$

$$\boldsymbol{\Omega} = \frac{3}{8\pi R} \left( 0, 0, \frac{4}{3} \cdot 2\pi b_1 \right) = \frac{b_1}{R} \hat{\mathbf{z}} \quad (\text{B.42})$$



.....

## C. Publication



### Hydrodynamic Synchronization of Chiral Microswimmers

Sotiris Samatas, Juho S. Lintuvuori

► **To cite this version:**

Sotiris Samatas, Juho S. Lintuvuori. Hydrodynamic Synchronization of Chiral Microswimmers. Physical Review Letters, 2023, 130 (2), pp.024001. 10.1103/PhysRevLett.130.024001 . hal-03945205

**HAL Id: hal-03945205**

**<https://hal.science/hal-03945205>**

Submitted on 18 Jan 2023

**HAL** is a multi-disciplinary open access archive for the deposit and dissemination of scientific research documents, whether they are published or not. The documents may come from teaching and research institutions in France or abroad, or from public or private research centers.

L'archive ouverte pluridisciplinaire **HAL**, est destinée au dépôt et à la diffusion de documents scientifiques de niveau recherche, publiés ou non, émanant des établissements d'enseignement et de recherche français ou étrangers, des laboratoires publics ou privés.

# Hydrodynamic synchronisation of chiral microswimmers

Sotiris Samatas and Juho Lintuvuori

*Univ. Bordeaux, CNRS, LOMA, UMR 5798, F-33400 Talence, France*

(Dated: January 18, 2023)

We study synchronization in bulk suspensions of spherical microswimmers with chiral trajectories using large scale numerics. The model is generic. It corresponds to the lowest order solution of a general model for self-propulsion at low Reynolds numbers, consisting of a nonaxisymmetric rotating source dipole. We show that both purely circular and helical swimmers can spontaneously synchronize their rotation. The synchronized state corresponds to velocity alignment with high orientational order in both the polar and azimuthal directions. Finally, we consider a racemic mixture of helical swimmers where intraspecies synchronization is observed while the system remains as a spatially uniform fluid. Our results demonstrate hydrodynamic synchronization as a natural collective phenomenon for microswimmers with chiral trajectories.

*Introduction.*— Microswimmers are a subset of active matter systems and correspond to microscopic elements self-propelling within a fluid environment. Natural microswimmers consist of biological microorganisms [1–3] and their collective dynamics has gained a lot of interest of late [4–12]. This has inspired research on synthetic microswimmers, typically based on phoretic Janus particles [13–15]. The interest for developing artificial swimmers has been fuelled by the various promising possibilities for applications such as micro-cargo transportation[16–19], targeted drug delivery[19–22], artificial insemination[19, 23] and microsurgery[19, 20, 24–26].

Most theoretical studies of microswimmer suspensions have concentrated on particles that swim in straight lines, with simulations predicting the spontaneous formation of collective swimming along a common direction — uniform polar order [27–33]. However, microorganisms typically have intrinsic chirality and tend to swim along helical paths [34–44]. Similarly, any asymmetry due to imperfections in the shape of the colloids or in their catalytic coating would also lead to chiral motion for artificial swimmers [13, 45–48].

Continuum descriptions based on the long-range hydrodynamics produced by flow singularities [49–52] have been extensively used in the past, with some works including chiral flows [53–55]. However, these models fail to capture near-field hydrodynamic effects, which are believed to be crucial for the formation of polar order [29, 30].

Most of the current theoretical work of active particles moving along chiral paths relies on dry microscopic descriptions such as active Brownian particle (ABP) models [56–65]. These effectively account for excluded volume effects, but neglect hydrodynamic interactions. Simulations of rotational dry models have predicted large-scale synchronisation, when a Kuramoto-type alignment term is included [57, 66]. Very recently, work on the hydrodynamics of chiral swimmers has started to emerge, but has so far been limited to single and two particle systems [67–72].

Explicitly incorporating chirality in hydrodynamic models used to study microswimmer suspensions could have an important effect regarding the emergence of collective states, such as large-scale collective oscillations[73, 74], polar order [27–33] or hydrodynamic synchronisation [75–81]. While synchronisation arising from active flows has been predicted for linear trimers [75] and for rotors on a 2-dimensional lattice [79], the ability of microswimmers to spontaneously synchronise (or not) in freely moving bulk suspensions, remains an open question.

Here, we show that swimmers with chiral trajectories can synchronise their rotation in a fully three-dimensional suspension. We consider finite sized swimmers, with a surface slip-flow arising from the general solution for self-propulsion at low Reynolds numbers [82], corresponding to a rotating source dipole flow inclined at an angle  $\psi$  with respect to the particle polar direction. A synchronised state, corresponds to the alignment of these dipoles. We study three distinct cases: circular swimmers, helical swimmers, and a racemic mixture of left-handed and right-handed helical swimmers. In all cases, the spontaneous formation of synchronised states is observed.

*Model for rotational squirmers.*— To model the microswimmers, we consider spherical particles of radius  $a$ , and extend the standard squirmer model [83, 84] to include rotational slip-flows. Based on Lamb’s general solution, the tangential slip-flow at the particle surface, is given in spherical coordinates by an infinite series of modes for the polar and azimuthal components  $\mathbf{e}_\theta$  and  $\mathbf{e}_\varphi$ [82]. The lowest order modes correspond to self-propulsion (source dipoles and rotlets), while the higher order terms correspond to fluid mixing. We choose [82, 85]

$$\begin{aligned} u_\theta|_{r=a} &= B_1 \sin\theta + \tilde{B}_{11} \cos\theta \sin\varphi \\ u_\varphi|_{r=a} &= C_1 \sin\theta + \tilde{B}_{11} \cos\varphi. \end{aligned} \quad (1)$$

The  $B_1$  mode corresponds to the source dipole in the standard squirmer model (top right panel in Fig. 1a).

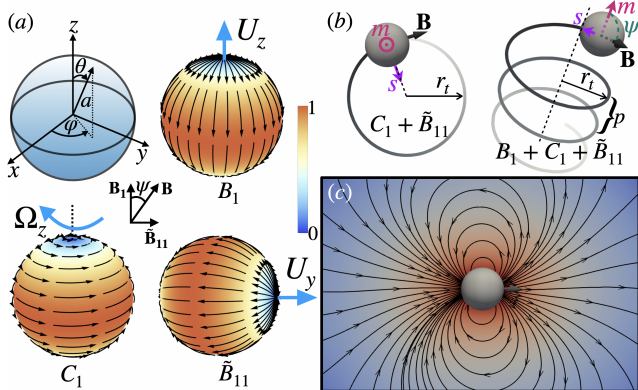


FIG. 1. Model for rotational squirmers. (a) The surface slip-flows corresponding to the different modes:  $B_1$ ,  $C_1$  and  $\tilde{B}_{11}$  in the particle frame. The magnitude of the normalised surface velocity (slip flow) for each mode is represented by a colour-code and the streamlines are coloured black. (b) The particle trajectories in the lab frame, corresponding to circular (left) and helical (right) swimming. The unit vectors  $\mathbf{m}$  and  $\mathbf{s}$  correspond to the particle polar and azimuthal axes respectively and  $\psi$  is the inclination angle with respect to  $\mathbf{m}$ . (c) Swimmer flow field obtained from the simulations, corresponding to a source dipole  $\mathbf{B}$  (neutral squirmer). The magnitude of the fluid velocity is coloured using a logarithmic scale and overlaid by black streamlines.

$C_1$  leads to a rotation of the particle around its polar axis  $z$  (or  $\mathbf{m}$ ) with an angular velocity  $\omega_0 = C_1/a$  (bottom left panel in Fig. 1a).  $\tilde{B}_{11}$  corresponds to a source dipole along  $\mathbf{y}$  (bottom right panel in Fig. 1a). The total swimmer flow field corresponds to a single source dipole  $\mathbf{B}$  with magnitude  $B = \sqrt{\tilde{B}_{11}^2 + B_1^2}$ , which rotates around the polar axis ( $\mathbf{m}$ ) at an inclination  $\psi = |\tan^{-1}(\tilde{B}_{11}/B_1)|$  (Fig. 1). An isolated particle has a swimming speed  $v_0 = \frac{2}{3}B$ . When  $\psi = 90^\circ$  ( $B_1 = 0$ ) the swimmers have circular trajectories in a plane perpendicular to  $\mathbf{m}$  (left in Fig. 1b). The radius of the trajectory is given by  $r_t = 2\tilde{B}_{11}a/(3C_1)$  and the period by  $T_0 = 2\pi/\omega_0 = 2\pi a/C_1$ . For  $\psi \neq 90^\circ$  and  $\psi \neq 0^\circ$  the trajectories become helical with pitch length  $p = 4\pi B_1 a/(3C_1)$  (right panel in Fig. 1b). To characterise the helical swimming, we define the ratio  $\lambda \equiv r_t/p = \tilde{B}_{11}/(2\pi B_1)$  [85].

To study the collective dynamics of suspensions of  $N$  swimmers, we use the lattice Boltzmann method [85]. The typical particle Reynolds number is  $\text{Re} \sim 0.01$  with simulation times  $\sim 100$ s. (see supplementary material [85] for details of simulations and mapping to SI units). An orientationally ordered state, corresponds to the alignment of the source dipoles  $\mathbf{B}$ . The amount of alignment can be measured by considering a velocity order parameter  $P_v(t) = \frac{|\sum_i^N \hat{v}_i|}{N}$ , where  $\hat{v}_i = \mathbf{v}_i/v_i$ . To further quantify the ordering, we measure the alignment along the azimuthal  $\mathbf{s}$  and polar  $\mathbf{m}$  directions, by calcu-

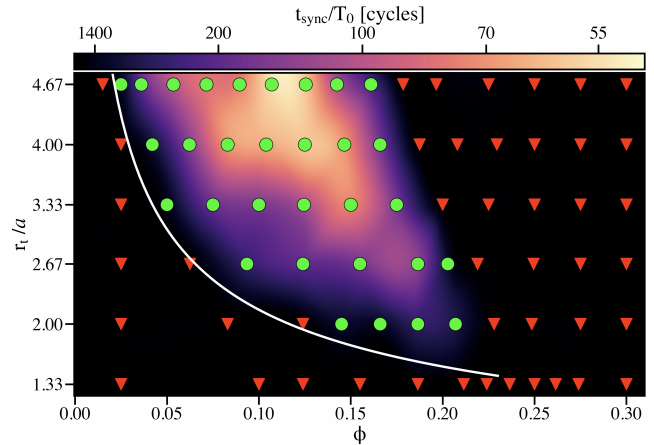


FIG. 2. Synchronisation diagram for circular swimmers ( $\psi = 90^\circ$ ) as a function of the volume fraction  $\phi$  and particle trajectory radius  $r_t$ . Green circles indicate global synchronisation, and the red triangles mark isotropic states. The synchronisation region is coloured according to a waiting time  $t_{\text{sync}}/T_0$  corresponding to the total time elapsed from the start of the simulation until synchronisation is reached. The white curve corresponds to  $\phi = \phi'_c \frac{4/3\pi a^3}{2\pi r_t^2 a}$  with  $\phi'_c = 70\%$ . (see text and supplementary material [85] for details).

lating  $P_{s|m}(t) = \frac{|\sum_i^N \mathbf{s}_i \cdot \mathbf{m}_i|}{N}$ .  $P_{v|s|m} = 1$  corresponds to complete order, and 0 to an isotropic state.

*Synchronisation of circular swimmers.*— Starting from isotropic initial conditions, we find that circular swimmers spontaneously synchronise their rotation when  $\phi \approx 3 \dots 23\%$  and  $r_t \approx 2 \dots 5a$  (Fig. 2). The synchronisation corresponds to the spontaneous alignment of the particle velocities, with the growth of both azimuthal and polar order, where typically  $P_s \approx P_m \approx P_v \gtrsim 0.85$  at long times (Fig. 3a). The phase locking is apparent from the distribution of the lag angle  $\alpha = \alpha_{1,2}^s$  calculated from all the particle pairs, considering the  $\mathbf{s}$  vectors of two different rotors in the plane perpendicular to the global polar director,  $\mathbf{P}_M \sim \sum_i^N \mathbf{m}_i$ . The distribution of  $\alpha$  changes from uniform at  $t \approx 0$  to a normal distribution with a peak at  $\alpha \approx 0$  in the globally synchronised state (Fig. 3d). In this state, the particle trajectories are circular and aligned perpendicularly to  $\mathbf{P}_M$  (right in Fig. 3e). The particle positions remain isotropic with the pair-correlation functions  $g(r)$ ,  $g(r_\perp)$  and  $g(r_\parallel)$  showing liquid-like structure (Fig. 3b).

The likelihood of the synchronisation depends on the volume fraction  $\phi$  and the trajectory radius  $r_t$  (Fig. 2). At low  $\phi$  the system remains in an isotropic state with the circular trajectories randomly oriented and distributed. When  $\phi$  is increased, the trajectories become jagged in the isotropic state (left in Fig. 3e). At long times the trajectories align (right in Fig. 3e). The distribution of rotational frequencies  $\omega$  has a peak at  $\omega_0$  and the width likely arises from the hydrodynamic fluctuations (Fig. 3c). In-

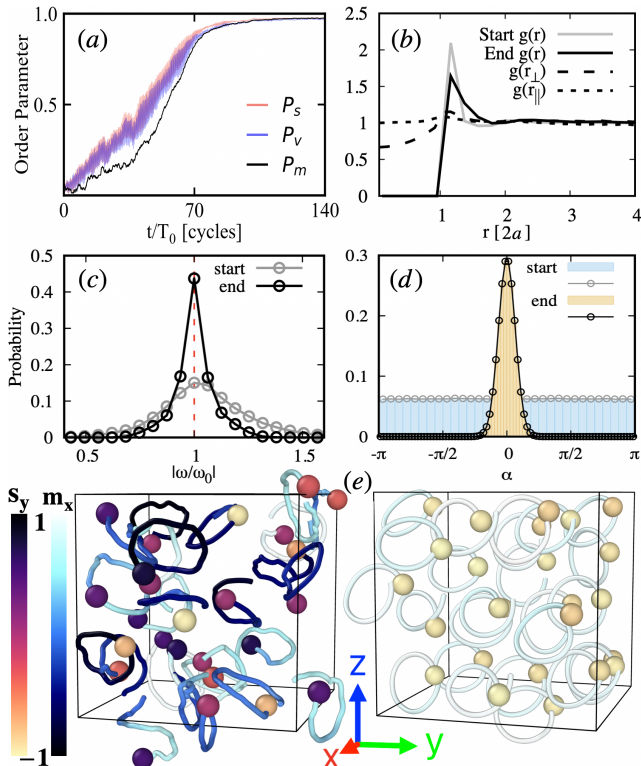


FIG. 3. (a) Circular swimmers: Example of a typical time evolution of the azimuthal  $P_s$  (red), velocity  $P_v$  (blue) and polar  $P_m$  (black) order parameters. (b) Radial distribution function  $g(r)$  of the system at the beginning (gray) and at the end (black) of the simulation. The  $g(r_\perp)$  ( $g(r_\parallel)$ ) are calculated perpendicular (parallel) to the polar director  $\mathbf{P}_M$ . Probability distribution of the (c) angular velocities  $\omega$  and (d) phase lag angle  $\alpha$  between all particle pairs, at the start and end of the simulation. (e) Snapshots of 25 selected particles at the beginning (left) and end (right) of the simulation. The particles are coloured according to the  $y$ -component of their  $\mathbf{s}$  vector. The trajectories are shown over one period and coloured according to the  $x$ -component of the swimmer's  $\mathbf{m}$  vector. (The data corresponds to  $\phi \approx 0.15$  and  $r_t \approx 3.33a$ ).

terestingly, the particle dynamics is reminiscent of the active-absorbing state transition predicted for dry circular swimmers in 2-dimensions (2D) [62] — the diffusive dynamics in the isotropic state becomes sub-diffusive when the spontaneous synchronisation occurs [85]. However, in the 2D dry system, where the particles interact exclusively via steric collisions, only local synchronisation was observed [62]. This suggests that hydrodynamic interactions are crucial for the large scale synchronisation observed here.

Previous studies of linear squirmers predict that the alignment of source dipoles corresponding to the formation of uniaxial polar order is dominated by near-field hydrodynamic interactions [29, 30]. When  $r_t \sim a$ , an isolated swimmer sweeps an area  $\sim r_t^2$  during one period  $T_0$ , and can be thought to occupy an effective volume

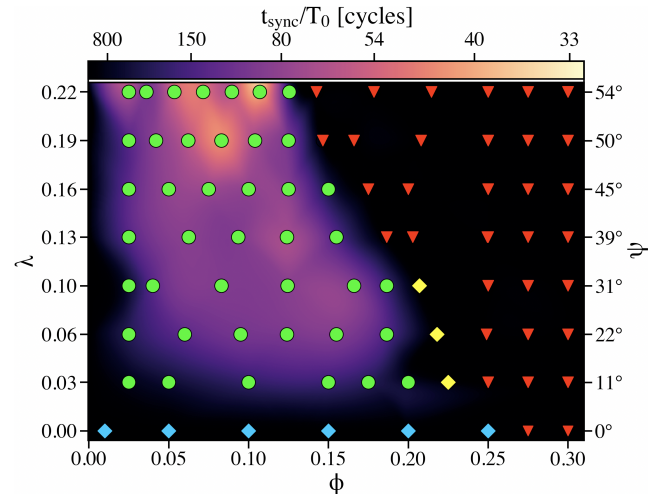


FIG. 4. State diagram for helical swimmers as a function of  $\phi$  and  $\lambda = r_t/p$ . The green circles correspond to global synchronisation, and red triangles to isotropic states. The blue diamonds mark polar order for classic linear neutral squirmers and yellow diamonds correspond to finite polar order in the absence of synchronisation for chiral swimmers. (data corresponds to  $p \approx 21a$ ).

$2\pi r_t^2 a$ . The lower- $\phi$  limit for the synchronisation region, closely corresponds to the random close packing of discotic cylinders with volume  $2\pi r_t^2 a$  [85] (white line in Fig. 2). Above this line, the effective volumes overlap in the isotropic state, and the swimmers have a high probability of interacting via near-field hydrodynamics.

To study the ordering dynamics, we measure the total time  $t_{sync}$  from the beginning of the simulation until synchronisation is reached. The fastest formation is observed in the middle of the synchronised region (Fig. 2). For a given  $r_t$ , if  $\phi$  is too large no synchronisation is observed. This implies the existence of a dynamic bottleneck where the particles have multiple collisions during their full-rotation time  $T_0$ , hindering the growth of global alignment. For simulations towards the high- $\phi$  end of the synchronisation region,  $t_{sync}$  is increased (Fig. 2), and the order parameters fluctuate close to zero before the growth of the order begins.

*Helical swimmers.* — The helical swimmer trajectories are characterised by the ratio between the radius of curvature of the trajectory and the pitch length  $\lambda = r_t/p$  (Fig. 1b). The particle motion is 3-dimensional, leading to an increase of the probability of near-field interactions. Hence, synchronisation is observed at lower  $\phi$  than in the case of pure rotors (Fig. 2 and 4). Similarly to circular swimmers, a high degree of order is observed in the synchronised state (Fig. 5a and b), and the particles swim along a common direction, with their helical trajectories aligned (Fig. 5c). Interestingly, when the ratio  $\bar{B}_{11}/B_1$  is decreased, the ordering dynamics is observed to change from a smooth growth to a two-step process where the ve-

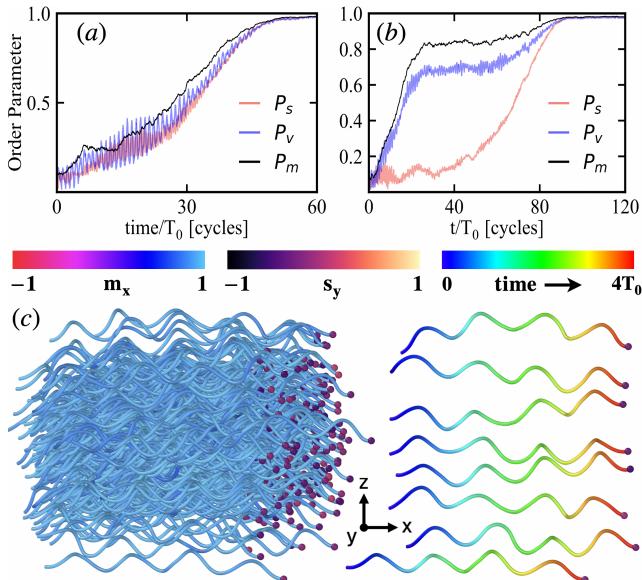


FIG. 5. Helical swimmers: Time-evolution of the order parameters  $P_s$  (red),  $P_v$  (blue) and  $P_m$  (black) for (a)  $\phi \approx 0.083$ ,  $\lambda \approx 0.19$  and (b)  $\phi \approx 0.125$ ,  $\lambda \approx 0.1$ . (c) Snapshots of the system in the synchronised state. The unwrapped trajectories of all the  $N = 286$  helical swimmers coloured according to  $m_x$  (left). 8 selected microswimmers with their trajectories coloured as a function of time (right). The particles are coloured according to  $s_y$ . (The snapshots in (c) correspond to  $\phi \approx 0.15$ ,  $\lambda \approx 0.16$ ).

locity alignment initially corresponds only to alignment in the polar direction (see *e.g.* Fig. 5a and b, for  $\lambda \approx 0.19$  and  $\lambda \approx 0.1$ , respectively). Both the rotational frequency and the phase locking show comparable behaviour to the circular swimmers [85].

When  $\lambda = 0$ , the swimmers correspond to achiral neutral squirmers and the formation of pure polar order ( $P_m > 0$ ;  $P_s \sim 0$ ) is observed (blue diamonds in Fig 4) in agreement with [27–33]. Remarkably, we also find cases with  $\lambda > 0$  with stable polar order in the absence of azimuthal ordering ( $P_m > 0$ ;  $P_s \approx 0$ ) (yellow diamonds in Fig. 4).

The synchronisation spans to low chiralities, and is observed for  $\lambda \approx 0.03 \dots 0.22$  and  $\phi \approx 2.5 \dots 20\%$  (Fig. 4). The  $\lambda$  range corresponds to experimentally observed trajectories of biological swimmers such as  $\lambda = r_t/p \approx 0.05$  for *T. thermophila* [39] and  $\lambda \approx 0.15$  for the 3-dimensional swimming of sperm [40]. We note that the transition between synchronised chiral states and the linear polar state ( $\lambda = 0$ ) is predicted to occur between  $\lambda \lesssim 0.03$  and  $\lambda = 0$  (Fig. 4). This suggests that synchronisation may well be observable at lower chiralities than  $\lambda \approx 0.03$  considered in Fig. 4.

*Racemic mixture.*— Finally, to study the effect of frustration, we construct a racemic mixture composed of right-handed and left-handed helical swimmers by choos-

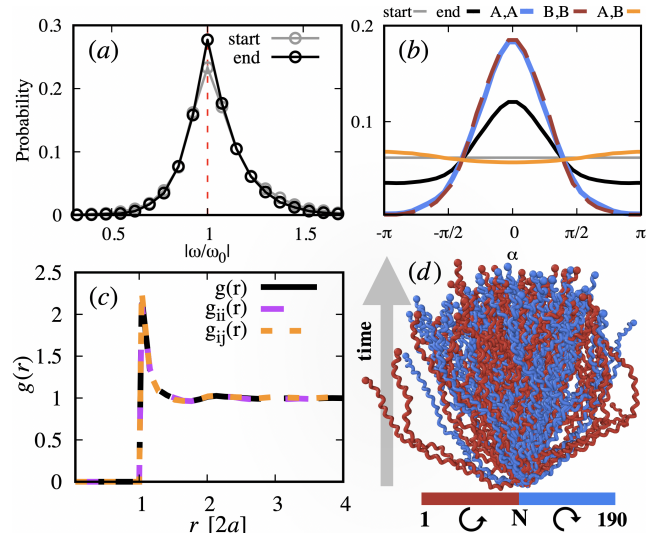


FIG. 6. Racemic mixture: Distributions of the (a) spinning frequency  $\omega$  and (b) the phase-angle difference  $\alpha$  calculated for all swimmer pairs (black), for clockwise (blue) and counter-clockwise (red) rotating populations, as well as for the cross population (orange). (c) Total (black), homochiral (violet) and heterochiral (orange) radial distribution functions. (d) Snapshot of the unwrapped trajectories at the steady state after  $20T_0$ . (The data corresponds to  $\phi \approx 0.1$  and  $\lambda \approx 0.16$ ).

ing  $C_1 = \pm 0.001$  (Fig. 6). We start from a fully mixed isotropic state. At the steady state, the particles, on average, swim along a common direction (Fig. 6d) and the rotational frequency  $\omega$  is observed to peak at  $\omega_0$  (Fig. 6a). The intra-species  $\alpha$  shows strong phase-locking (blue and red curves in Fig. 6b), whereas for the cross-species no significant peak is observed (orange curve Fig. 6b), due to the oppositely spinning populations. However, the distribution shows a slight preference for  $\alpha = \pm\pi$ , which corresponds to a parallel orientation of the in-plane projections of the source dipoles [85]. Within the time-scale of the simulations, we observe no spatial separation of the swimmers — the fluid-like pair-correlation function calculated within species and cross-species matches with the  $g(r)$  of the whole system (Fig. 6c).

*Conclusions.*— Using hydrodynamic simulations we have investigated suspensions of microswimmers with chiral trajectories at the limit of zero thermal noise. The results suggest the emergence of hydrodynamic synchronisation as a naturally occurring collective phenomenon for microswimmers. The predictions should be relevant to a wide variety of experimental systems; such as helically swimming bacteria [39] and sperm [40], or chiral Quincke rollers [86] and spherical ciliates [87], where rotational motion occurs naturally. The observation of the intra-species synchronisation in the racemic mixture, provides a surprising example of two synchronised, interpenetrating, fluids. Further, it demonstrates that the synchronisation is maintained in the presence of hydro-

dynamic fluctuations arising from the source-dipole  $1/r^3$  far-fields. This suggests, that it could be interesting to (re)analyse 3-dimensional correlations in the rotational degrees of freedom in systems exhibiting polar order, such as areas of uniform order in bacterial systems [4–12] or polar flocks in motile colloids [88].

*Acknowledgments.* Discussions with Zaiyi Shen and Alois Würger are gratefully acknowledged. SS acknowledges University of Bordeaux, and the A. G. Leventis Foundation for funding, as well as cluster CURTA at MCIA for computational time. JSL acknowledges the French National Research Agency (ANR) through Contract No. ANR-19-CE06-0012-01 and la region Nouvelle Aquitaine project GASPP for funding.

- 
- [1] D. L. Koch and G. Subramanian, Collective hydrodynamics of swimming microorganisms: living fluids, *Annual Review of Fluid Mechanics* **43**, 637 (2011).
  - [2] E. Lauga, Bacterial hydrodynamics, *Annual Review of Fluid Mechanics* **48**, 105 (2016).
  - [3] E. Lauga, *The fluid dynamics of cell motility*, Vol. 62 (Cambridge University Press, 2020).
  - [4] C. Dombrowski, L. Cisneros, S. Chatkaew, R. E. Goldstein, and J. O. Kessler, Self-concentration and large-scale coherence in bacterial dynamics, *Physical review letters* **93**, 098103 (2004).
  - [5] A. Sokolov, I. S. Aranson, J. O. Kessler, and R. E. Goldstein, Concentration dependence of the collective dynamics of swimming bacteria, *Physical review letters* **98**, 158102 (2007).
  - [6] C. W. Wolgemuth, Collective swimming and the dynamics of bacterial turbulence, *Biophysical journal* **95**, 1564 (2008).
  - [7] L. H. Cisneros, R. Cortez, C. Dombrowski, R. E. Goldstein, and J. O. Kessler, Fluid dynamics of self-propelled microorganisms, from individuals to concentrated populations, in *Animal Locomotion* (Springer, 2010) pp. 99–115.
  - [8] H.-P. Zhang, A. Be'er, E.-L. Florin, and H. L. Swinney, Collective motion and density fluctuations in bacterial colonies, *Proceedings of the National Academy of Sciences* **107**, 13626 (2010).
  - [9] A. Sokolov and I. S. Aranson, Physical properties of collective motion in suspensions of bacteria, *Physical review letters* **109**, 248109 (2012).
  - [10] H. H. Wensink, J. Dunkel, S. Heidenreich, K. Drescher, R. E. Goldstein, H. Löwen, and J. M. Yeomans, Mesoscale turbulence in living fluids, *Proceedings of the national academy of sciences* **109**, 14308 (2012).
  - [11] J. Dunkel, S. Heidenreich, K. Drescher, H. H. Wensink, M. Bär, and R. E. Goldstein, Fluid dynamics of bacterial turbulence, *Physical review letters* **110**, 228102 (2013).
  - [12] Y. Peng, Z. Liu, and X. Cheng, Imaging the emergence of bacterial turbulence: Phase diagram and transition kinetics, *Science Advances* **7**, eabd1240 (2021).
  - [13] S. J. Ebbens and D. A. Gregory, Catalytic janus colloids: controlling trajectories of chemical microswimmers, *Accounts of chemical research* **51**, 1931 (2018).
  - [14] I. Theurkauff, C. Cottin-Bizonne, J. Palacci, C. Ybert, and L. Bocquet, Dynamic clustering in active colloidal suspensions with chemical signaling, *Physical Review Letters* **108**, 268303 (2012).
  - [15] F. Ginot, I. Theurkauff, F. Detcheverry, C. Ybert, and C. Cottin-Bizonne, Aggregation-fragmentation and individual dynamics of active clusters, *Nature communications* **9**, 1 (2018).
  - [16] L. Baraban, M. Tasinkevych, M. N. Popescu, S. Sanchez, S. Dietrich, and O. Schmidt, Transport of cargo by catalytic janus micro-motors, *Soft Matter* **8**, 48 (2012).
  - [17] A. M. Boymelgreen, T. Balli, T. Miloh, and G. Yossifon, Active colloids as mobile microelectrodes for unified label-free selective cargo transport, *Nature communications* **9**, 1 (2018).
  - [18] P. Mena-Giraldo and J. Orozco, Polymeric micro/nanocarriers and motors for cargo transport and phototriggered delivery, *Polymers* **13**, 3920 (2021).
  - [19] A.-I. Bunea and R. Taboryski, Recent advances in microswimmers for biomedical applications, *Micromachines* **11**, 1048 (2020).
  - [20] S. K. Srivastava, M. Medina-Sánchez, B. Koch, and O. G. Schmidt, Medibots: dual-action biogenic microdagger for single-cell surgery and drug release, *Advanced Materials* **28**, 832 (2016).
  - [21] A. V. Singh, M. H. D. Ansari, C. B. Dayan, J. Giltinan, S. Wang, Y. Yu, V. Kishore, P. Laux, A. Luch, and M. Sitti, Multifunctional magnetic hairbot for untethered osteogenesis, ultrasound contrast imaging and drug delivery, *Biomaterials* **219**, 119394 (2019).
  - [22] T. Bhuyan, A. K. Singh, D. Dutta, A. Unal, S. S. Ghosh, and D. Bandyopadhyay, Magnetic field guided chemotaxis of imushbots for targeted anticancer therapeutics, *ACS Biomaterials Science & Engineering* **3**, 1627 (2017).
  - [23] M. Medina-Sánchez, L. Schwarz, A. K. Meyer, F. Hebenstreit, and O. G. Schmidt, Cellular cargo delivery: Toward assisted fertilization by sperm-carrying micromotors, *Nano letters* **16**, 555 (2016).
  - [24] B. J. Nelson, I. K. Kaliakatsos, and J. J. Abbott, Microbots for minimally invasive medicine, *Annual review of biomedical engineering* **12**, 55 (2010).
  - [25] A.-I. Bunea and J. Glückstad, Strategies for optical trapping in biological samples: Aiming at microrobotic surgeons, *Laser & Photonics Reviews* **13**, 1800227 (2019).
  - [26] P. A. York, R. Peña, D. Kent, and R. J. Wood, Microrobotic laser steering for minimally invasive surgery, *Science Robotics* **6**, eabd5476 (2021).
  - [27] A. A. Evans, T. Ishikawa, T. Yamaguchi, and E. Lauga, Orientational order in concentrated suspensions of spherical microswimmers, *Physics of Fluids* **23**, 111702 (2011).
  - [28] F. Alarcón and I. Pagonabarraga, Spontaneous aggregation and global polar ordering in squirmer suspensions, *Journal of Molecular Liquids* **185**, 56 (2013).
  - [29] N. Yoshinaga and T. B. Liverpool, Hydrodynamic interactions in dense active suspensions: From polar order to dynamical clusters, *Physical Review E* **96**, 020603(R) (2017).
  - [30] N. Yoshinaga and T. B. Liverpool, From hydrodynamic lubrication to many-body interactions in dense suspensions of active swimmers, *The European Physical Journal E* **41**, 1 (2018).

- [31] B. Delmotte, E. E. Keaveny, F. Plouraboué, and E. Climent, Large-scale simulation of steady and time-dependent active suspensions with the force-coupling method, *Journal of Computational Physics* **302**, 524 (2015).
- [32] M. Theers, E. Westphal, K. Qi, R. G. Winkler, and G. Gompper, Clustering of microswimmers: interplay of shape and hydrodynamics, *Soft matter* **14**, 8590 (2018).
- [33] N. Oyama, J. J. Molina, and R. Yamamoto, Do hydrodynamically assisted binary collisions lead to orientational ordering of microswimmers?, *The European Physical Journal E* **40**, 1 (2017).
- [34] D. Bray, *Cell movements: from molecules to motility* (Garland Science, 2000).
- [35] H. S. Jennings, On the significance of the spiral swimming of organisms, *The American Naturalist* **35**, 369 (1901).
- [36] G. Jékely, J. Colombelli, H. Hausen, K. Guy, E. Stelzer, F. Nédélec, and D. Arendt, Mechanism of phototaxis in marine zooplankton, *Nature* **456**, 395 (2008).
- [37] T. Fenchel and N. Blackburn, Motile chemosensory behaviour of phagotrophic protists: mechanisms for and efficiency in congregating at food patches, *Protist* **150**, 325 (1999).
- [38] M. McHenry and J. Strother, The kinematics of phototaxis in larvae of the ascidian aplidium constellatum, *Marine Biology* **142**, 173 (2003).
- [39] A. Marumo, M. Yamagishi, and J. Yajima, Three-dimensional tracking of the ciliate tetrahymena reveals the mechanism of ciliary stroke-driven helical swimming, *Communications biology* **4**, 1 (2021).
- [40] G. Corkidi, B. Taboada, C. Wood, A. Guerrero, and A. Darszon, Tracking sperm in three-dimensions, *Biochemical and biophysical research communications* **373**, 125 (2008).
- [41] J. F. Jikeli, L. Alvarez, B. M. Friedrich, L. G. Wilson, R. Pascal, R. Colin, M. Pichlo, A. Rennhack, C. Brenker, and U. B. Kaupp, Sperm navigation along helical paths in 3d chemoattractant landscapes, *Nature communications* **6**, 1 (2015).
- [42] R. Thar and T. Fenchel, True chemotaxis in oxygen gradients of the sulfur-oxidizing bacterium thiovulum majus, *Applied and environmental microbiology* **67**, 3299 (2001).
- [43] T.-W. Su, I. Choi, J. Feng, K. Huang, E. McLeod, and A. Ozcan, Sperm trajectories form chiral ribbons, *Scientific reports* **3**, 1 (2013).
- [44] D. R. Brumley, M. Polin, T. J. Pedley, and R. E. Goldstein, Hydrodynamic synchronization and metachronal waves on the surface of the colonial alga volvox carteri, *Physical review letters* **109**, 268102 (2012).
- [45] D. Vilela, M. M. Stanton, J. Parmar, and S. Sánchez, Microbots decorated with silver nanoparticles kill bacteria in aqueous media, *ACS applied materials & interfaces* **9**, 22093 (2017).
- [46] F. Lancia, T. Yamamoto, A. Ryabchun, T. Yamaguchi, M. Sano, and N. Katsonis, Reorientation behavior in the helical motility of light-responsive spiral droplets, *Nature communications* **10**, 1 (2019).
- [47] A. Brown and W. Poon, Ionic effects in self-propelled pt-coated janus swimmers, *Soft matter* **10**, 4016 (2014).
- [48] A. I. Campbell, R. Wittkowski, B. Ten Hagen, H. Löwen, and S. J. Ebbens, Helical paths, gravitaxis, and separation phenomena for mass-anisotropic self-propelling colloids: Experiment versus theory, *The Journal of Chemical Physics* **147**, 084905 (2017).
- [49] J. Blake and A. Chwang, Fundamental singularities of viscous flow, *Journal of Engineering Mathematics* **8**, 23 (1974).
- [50] C. Pozrikidis, *Boundary integral and singularity methods for linearized viscous flow* (Cambridge university press, 1992).
- [51] O. S. Pak, E. Lauga, C. Duprat, and H. Stone, Theoretical models of low-Reynolds-number locomotion, *Fluid-Structure Interactions in Low-Reynolds-Number Flows*. (2015).
- [52] E. Lauga and T. R. Powers, The hydrodynamics of swimming microorganisms, *Reports on progress in physics* **72**, 096601 (2009).
- [53] S. Fürthauer, M. Stempel, S. W. Grill, and F. Jülicher, Active chiral fluids, *The European physical journal E* **35**, 1 (2012).
- [54] B. M. Friedrich and F. Jülicher, Steering chiral swimmers along noisy helical paths, *Physical review letters* **103**, 068102 (2009).
- [55] R. Singh and R. Adhikari, Generalized stokes laws for active colloids and their applications, *Journal of Physics Communications* **2**, 025025 (2018).
- [56] H. Löwen, Chirality in microswimmer motion: From circle swimmers to active turbulence, *The European Physical Journal Special Topics* **225**, 2319 (2016).
- [57] B. Liebchen and D. Levis, Collective behavior of chiral active matter: Pattern formation and enhanced flocking, *Physical review letters* **119**, 058002 (2017).
- [58] D. Levis and B. Liebchen, Simultaneous phase separation and pattern formation in chiral active mixtures, *Physical Review E* **100**, 012406 (2019).
- [59] G.-J. Liao and S. H. Klapp, Clustering and phase separation of circle swimmers dispersed in a monolayer, *Soft matter* **14**, 7873 (2018).
- [60] D. Levis and B. Liebchen, Micro-flock patterns and macro-clusters in chiral active brownian disks, *Journal of Physics: Condensed Matter* **30**, 084001 (2018).
- [61] J. Bickmann, S. Bröker, J. Jeggle, and R. Wittkowski, Analytical approach to chiral active systems: Suppressed phase separation of interacting brownian circle swimmers, *arXiv preprint arXiv:2010.05262* (2020).
- [62] Q.-L. Lei, M. P. Ciamarra, and R. Ni, Nonequilibrium strongly hyperuniform fluids of circle active particles with large local density fluctuations, *Science advances* **5**, eaau7423 (2019).
- [63] Z. Ma and R. Ni, Dynamical clustering interrupts motility-induced phase separation in chiral active brownian particles, *The Journal of Chemical Physics* **156**, 021102 (2022).
- [64] G.-J. Liao and S. H. Klapp, Emergent vortices and phase separation in systems of chiral active particles with dipolar interactions, *Soft Matter* **17**, 6833 (2021).
- [65] B. Liebchen and D. Levis, Chiral active matter, *Europhysics Letters* **139**, 67001 (2022).
- [66] D. Levis, I. Pagonabarraga, and B. Liebchen, Activity induced synchronization: Mutual flocking and chiral self-sorting, *Physical Review Research* **1**, 023026 (2019).
- [67] F. Fadda, J. J. Molina, and R. Yamamoto, Dynamics of a chiral swimmer sedimenting on a flat plate, *Physical Review E* **101**, 052608 (2020).
- [68] P. Burada, R. Maity, and F. Jülicher, Hydrodynamics of chiral squirmers, *Physical Review E* **105**, 024603 (2022).

- [69] R. Maity and P. Burada, Near and far-field hydrodynamic interaction of two chiral squirmers, arXiv preprint arXiv:2204.07512 (2022).
- [70] R. Maity and P. Burada, Unsteady chiral swimmer in presence of an external chemical gradient, arXiv preprint arXiv:2105.15001 (2021).
- [71] S. Rode, J. Elgeti, and G. Gompper, Multi-ciliated microswimmers—metachronal coordination and helical swimming, *The European Physical Journal E* **44**, 1 (2021).
- [72] M. Lisicki, S. Y. Reigh, and E. Lauga, Autophoretic motion in three dimensions, *Soft Matter* **14**, 3304 (2018).
- [73] C. Chen, S. Liu, X.-q. Shi, H. Chaté, and Y. Wu, Weak synchronization and large-scale collective oscillation in dense bacterial suspensions, *Nature* **542**, 210 (2017).
- [74] B. Zhang, B. Hilton, C. Short, A. Souslov, and A. Snezhko, Oscillatory chiral flows in confined active fluids with obstacles, *Physical Review Research* **2**, 043225 (2020).
- [75] V. B. Putz and J. M. Yeomans, Hydrodynamic synchronisation of model microswimmers, *Journal of Statistical Physics* **137**, 1001 (2009).
- [76] B. Qian, H. Jiang, D. A. Gagnon, K. S. Breuer, and T. R. Powers, Minimal model for synchronization induced by hydrodynamic interactions, *Physical Review E* **80**, 061919 (2009).
- [77] N. Uchida and R. Golestanian, Synchronization and collective dynamics in a carpet of microfluidic rotors, *Physical review letters* **104**, 178103 (2010).
- [78] J. Kotar, M. Leoni, B. Bassetti, M. C. Lagomarsino, and P. Cicuta, Hydrodynamic synchronization of colloidal oscillators, *Proceedings of the National Academy of Sciences* **107**, 7669 (2010).
- [79] R. Golestanian, J. M. Yeomans, and N. Uchida, Hydrodynamic synchronization at low reynolds number, *Soft Matter* **7**, 3074 (2011).
- [80] M. Theers and R. G. Winkler, Synchronization of rigid microrotors by time-dependent hydrodynamic interactions, *Physical Review E* **88**, 023012 (2013).
- [81] K. Han, G. Kokot, S. Das, R. G. Winkler, G. Gompper, and A. Snezhko, Reconfigurable structure and tunable transport in synchronized active spinner materials, *Science advances* **6**, eaaz8535 (2020).
- [82] O. S. Pak and E. Lauga, Generalized squirming motion of a sphere, *Journal of Engineering Mathematics* **88**, 1 (2014).
- [83] M. Lighthill, On the squirming motion of nearly spherical deformable bodies through liquids at very small reynolds numbers, *Communications on pure and applied mathematics* **5**, 109 (1952).
- [84] J. R. Blake, A spherical envelope approach to ciliary propulsion, *Journal of Fluid Mechanics* **46**, 199 (1971).
- [85] See Supplemental Material xxx for additional details for the surface slip-flow, computational details and mapping to SI units. It includes additional references references [89–104].
- [86] B. Zhang, A. Sokolov, and A. Snezhko, Reconfigurable emergent patterns in active chiral fluids, *Nature communications* **11**, 1 (2020).
- [87] K. Drescher, K. C. Leptos, I. Tuval, T. Ishikawa, T. J. Pedley, and R. E. Goldstein, Dancing volvox: hydrodynamic bound states of swimming algae, *Physical review letters* **102**, 168101 (2009).
- [88] A. Bricard, J.-B. Caussin, N. Desreumaux, O. Dauchot, and D. Bartolo, Emergence of macroscopic directed motion in populations of motile colloids, *Nature* **503**, 95 (2013).
- [89] J. S. Lintuvuori, A. T. Brown, K. Stratford, and D. Marenduzzo, Hydrodynamic oscillations and variable swimming speed in squirmers close to repulsive walls, *Soft Matter* **12**, 7959 (2016).
- [90] Z. Shen, A. Würger, and J. S. Lintuvuori, Hydrodynamic interaction of a self-propelling particle with a wall, *The European Physical Journal E* **41**, 39 (2018).
- [91] A. J. Ladd, Numerical simulations of particulate suspensions via a discretized boltzmann equation. part 1. theoretical foundation, *Journal of fluid mechanics* **271**, 285 (1994).
- [92] A. J. Ladd, Numerical simulations of particulate suspensions via a discretized boltzmann equation. part 2. numerical results, *Journal of fluid mechanics* **271**, 311 (1994).
- [93] N.-Q. Nguyen and A. Ladd, Lubrication corrections for lattice-boltzmann simulations of particle suspensions, *Physical Review E* **66**, 046708 (2002).
- [94] I. Llopis and I. Pagonabarraga, Hydrodynamic interactions in squirmer motion: Swimming with a neighbour and close to a wall, *Journal of Non-Newtonian Fluid Mechanics* **165**, 946 (2010).
- [95] I. Pagonabarraga and I. Llopis, The structure and rheology of sheared model swimmer suspensions, *Soft Matter* **9**, 7174 (2013).
- [96] A. Donev, I. Cisse, D. Sachs, E. A. Variano, F. H. Stillinger, R. Connelly, S. Torquato, and P. M. Chaikin, Improving the density of jammed disordered packings using ellipsoids, *Science* **303**, 990 (2004).
- [97] Z. Zhou, R. Zou, D. Pinson, and A. Yu, Discrete modelling of the packing of ellipsoidal particles, in *AIP Conference Proceedings*, Vol. 1542 (American Institute of Physics, 2013) pp. 357–360.
- [98] B. Martinez-Haya and A. Cuetos, Simulation study of discotic molecules in the vicinity of the isotropic–liquid crystal transition, *Molecular Simulation* **35**, 1077 (2009).
- [99] S. Li, J. Zhao, P. Lu, and Y. Xie, Maximum packing densities of basic 3d objects, *Chinese Science Bulletin* **55**, 114 (2010).
- [100] L. Liu, Y. Yuan, W. Deng, and S. Li, Evolutions of packing properties of perfect cylinders under densification and crystallization, *The Journal of chemical physics* **149**, 104503 (2018).
- [101] L. Liu, Z. Li, Y. Jiao, and S. Li, Maximally dense random packings of cubes and cuboids via a novel inverse packing method, *Soft matter* **13**, 748 (2017).
- [102] G. D. Scott and D. M. Kilgour, The density of random close packing of spheres, *Journal of Physics D: Applied Physics* **2**, 863 (1969).
- [103] J. G. Berryman, Random close packing of hard spheres and disks, *Physical Review A* **27**, 1053 (1983).
- [104] S. Torquato, T. M. Truskett, and P. G. Debenedetti, Is random close packing of spheres well defined?, *Physical review letters* **84**, 2064 (2000).







# Bibliography

- [1] Christopher Dombrowski et al. “Self-concentration and large-scale coherence in bacterial dynamics”. In: *Physical review letters* 93.9 (2004), p. 098103.
- [2] Andrey Sokolov et al. “Concentration dependence of the collective dynamics of swimming bacteria”. In: *Physical review letters* 98.15 (2007), p. 158102.
- [3] Charles W Wolgemuth. “Collective swimming and the dynamics of bacterial turbulence”. In: *Biophysical journal* 95.4 (2008), pp. 1564–1574.
- [4] Luis H Cisneros et al. “Fluid dynamics of self-propelled microorganisms, from individuals to concentrated populations”. In: *Animal Locomotion*. Springer, 2010, pp. 99–115.
- [5] He-Peng Zhang et al. “Collective motion and density fluctuations in bacterial colonies”. In: *Proceedings of the National Academy of Sciences* 107.31 (2010), pp. 13626–13630.
- [6] Andrey Sokolov and Igor S Aranson. “Physical properties of collective motion in suspensions of bacteria”. In: *Physical review letters* 109.24 (2012), p. 248109.
- [7] Henricus H Wensink et al. “Meso-scale turbulence in living fluids”. In: *Proceedings of the national academy of sciences* 109.36 (2012), pp. 14308–14313.
- [8] Jörn Dunkel et al. “Fluid dynamics of bacterial turbulence”. In: *Physical review letters* 110.22 (2013), p. 228102.
- [9] Yi Peng, Zhengyang Liu, and Xiang Cheng. “Imaging the emergence of bacterial turbulence: Phase diagram and transition kinetics”. In: *Science Advances* 7.17 (2021), eabd1240.
- [10] Stephen J Ebbens and David Alexander Gregory. “Catalytic Janus colloids: controlling trajectories of chemical microswimmers”. In: *Accounts of chemical research* 51.9 (2018), pp. 1931–1939.
- [11] Isaac Theurkauff et al. “Dynamic clustering in active colloidal suspensions with chemical signaling”. In: *Physical Review Letters* 108.26 (2012), p. 268303.
- [12] Félix Ginot et al. “Aggregation-fragmentation and individual dynamics of active clusters”. In: *Nature communications* 9.1 (2018), pp. 1–9.
- [13] L Baraban et al. “Transport of cargo by catalytic Janus micro-motors”. In: *Soft Matter* 8.1 (2012), pp. 48–52.
- [14] Alicia M Boymelgreen et al. “Active colloids as mobile microelectrodes for unified label-free selective cargo transport”. In: *Nature communications* 9.1 (2018), pp. 1–8.
- [15] Pedro Mena-Giraldo and Jahir Orozco. “Polymeric Micro/Nanocarriers and Motors for Cargo Transport and Phototriggered Delivery”. In: *Polymers* 13.22 (2021), p. 3920.
- [16] Ada-Ioana Bunea and Rafael Taboryski. “Recent advances in microswimmers for biomedical applications”. In: *Micromachines* 11.12 (2020), p. 1048.

- [17] Sarvesh Kumar Srivastava et al. “Medibots: dual-action biogenic microdaggers for single-cell surgery and drug release”. In: *Advanced Materials* 28.5 (2016), pp. 832–837.
- [18] Ajay Vikram Singh et al. “Multifunctional magnetic hairbot for untethered osteogenesis, ultrasound contrast imaging and drug delivery”. In: *Biomaterials* 219 (2019), p. 119394.
- [19] Tamanna Bhuyan et al. “Magnetic field guided chemotaxis of iMushbots for targeted anticancer therapeutics”. In: *ACS Biomaterials Science & Engineering* 3.8 (2017), pp. 1627–1640.
- [20] Mariana Medina-Sánchez et al. “Cellular cargo delivery: Toward assisted fertilization by sperm-carrying micromotors”. In: *Nano letters* 16.1 (2016), pp. 555–561.
- [21] Bradley J Nelson, Ioannis K Kaliakatsos, and Jake J Abbott. “Microrobots for minimally invasive medicine”. In: *Annual review of biomedical engineering* 12 (2010), pp. 55–85.
- [22] Ada-Ioana Bunea and Jesper Glückstad. “Strategies for optical trapping in biological samples: Aiming at microrobotic surgeons”. In: *Laser & Photonics Reviews* 13.4 (2019), p. 1800227.
- [23] Peter A York et al. “Microrobotic laser steering for minimally invasive surgery”. In: *Science Robotics* 6.50 (2021), eabd5476.
- [24] Mark A Shannon et al. “Science and technology for water purification in the coming decades”. In: *Nature* 452.7185 (2008), pp. 301–310.
- [25] Vilela Diana, Parmar Jemish, Sánchez Samuel, et al. “Microbots Decorated with Silver Nanoparticles Kill Bacteria in Aqueous Media”. In: (2017).
- [26] Eric Lauga. *The fluid dynamics of cell motility*. Vol. 62. Cambridge University Press, 2020.
- [27] Jeremy Pickett-Heaps. *Volvox carterii*. Youtube. 2014. URL: <https://www.youtube.com/watch?v=n7RggKhWD8g&t=3s>.
- [28] Gáspár Jékely et al. “Mechanism of phototaxis in marine zooplankton”. In: *Nature* 456.7220 (2008), pp. 395–399.
- [29] Ben Yellen. *Janus particle*. Duke University. 2009. URL: <https://www.nanowerk.com/news/newsid=12105.php>.
- [30] MM Stanton, C Trichet-Paredes, and Samuel Sanchez. “Applications of three-dimensional (3D) printing for microswimmers and bio-hybrid robotics”. In: *Lab on a Chip* 15.7 (2015), pp. 1634–1637.
- [31] Arthur A Evans et al. “Orientational order in concentrated suspensions of spherical microswimmers”. In: *Physics of Fluids* 23.11 (2011), p. 111702.
- [32] Francisco Alarcón and Ignacio Pagonabarraga. “Spontaneous aggregation and global polar ordering in squirmer suspensions”. In: *Journal of Molecular Liquids* 185 (2013), pp. 56–61.
- [33] Natsuhiko Yoshinaga and Tanniemola B Liverpool. “Hydrodynamic interactions in dense active suspensions: From polar order to dynamical clusters”. In: *Physical Review E* 96.2 (2017), 020603(R).

- [34] Natsuhiko Yoshinaga and Tanniemola B Liverpool. “From hydrodynamic lubrication to many-body interactions in dense suspensions of active swimmers”. In: *The European Physical Journal E* 41.6 (2018), pp. 1–22.
- [35] Blaise Delmotte et al. “Large-scale simulation of steady and time-dependent active suspensions with the force-coupling method”. In: *Journal of Computational Physics* 302 (2015), pp. 524–547.
- [36] Mario Theers et al. “Clustering of microswimmers: interplay of shape and hydrodynamics”. In: *Soft matter* 14.42 (2018), pp. 8590–8603.
- [37] Norihiro Oyama, John Jairo Molina, and Ryoichi Yamamoto. “Do hydrodynamically assisted binary collisions lead to orientational ordering of microswimmers?” In: *The European Physical Journal E* 40.11 (2017), pp. 1–8.
- [38] Dennis Bray. *Cell movements: from molecules to motility*. Garland Science, 2000.
- [39] Herbert Spencer Jennings. “On the significance of the spiral swimming of organisms”. In: *The American Naturalist* 35.413 (1901), pp. 369–378.
- [40] Tom Fenchel and Nicholas Blackburn. “Motile chemosensory behaviour of phagotrophic protists: mechanisms for and efficiency in congregating at food patches”. In: *Protist* 150.3 (1999), pp. 325–336.
- [41] M McHenry and J Strother. “The kinematics of phototaxis in larvae of the ascidian *Aplidium constellatum*”. In: *Marine Biology* 142.1 (2003), pp. 173–184.
- [42] Akisato Marumo, Masahiko Yamagishi, and Junichiro Yajima. “Three-dimensional tracking of the ciliate *Tetrahymena* reveals the mechanism of ciliary stroke-driven helical swimming”. In: *Communications biology* 4.1 (2021), pp. 1–6.
- [43] G Corkidi et al. “Tracking sperm in three-dimensions”. In: *Biochemical and biophysical research communications* 373.1 (2008), pp. 125–129.
- [44] Jan F Jikeli et al. “Sperm navigation along helical paths in 3D chemoattractant landscapes”. In: *Nature communications* 6.1 (2015), pp. 1–10.
- [45] Roland Thar and Tom Fenchel. “True chemotaxis in oxygen gradients of the sulfur-oxidizing bacterium *Thiovulum majus*”. In: *Applied and environmental microbiology* 67.7 (2001), pp. 3299–3303.
- [46] Ting-Wei Su et al. “Sperm trajectories form chiral ribbons”. In: *Scientific reports* 3.1 (2013), pp. 1–8.
- [47] Diana Vilela et al. “Microbots decorated with silver nanoparticles kill bacteria in aqueous media”. In: *ACS applied materials & interfaces* 9.27 (2017), pp. 22093–22100.
- [48] Federico Lancia et al. “Reorientation behavior in the helical motility of light-responsive spiral droplets”. In: *Nature communications* 10.1 (2019), pp. 1–8.
- [49] Andrew I Campbell et al. “Helical paths, gravitaxis, and separation phenomena for mass-anisotropic self-propelling colloids: Experiment versus theory”. In: *The Journal of Chemical Physics* 147.8 (2017), p. 084905.
- [50] JR Blake and AT Chwang. “Fundamental singularities of viscous flow”. In: *Journal of Engineering Mathematics* 8.1 (1974), pp. 23–29.

- [51] Constantine Pozrikidis. *Boundary integral and singularity methods for linearized viscous flow*. Cambridge university press, 1992.
- [52] On Shun Pak et al. Theoretical models of low-Reynolds-number locomotion, *Fluid-Structure Interactions in Low-Reynolds-Number Flows*. 2015.
- [53] Eric Lauga and Thomas R Powers. “The hydrodynamics of swimming microorganisms”. In: *Reports on progress in physics* 72.9 (2009), p. 096601.
- [54] S Fürthauer et al. “Active chiral fluids”. In: *The European physical journal E* 35.9 (2012), pp. 1–13.
- [55] Benjamin M Friedrich and Frank Jülicher. “Steering chiral swimmers along noisy helical paths”. In: *Physical review letters* 103.6 (2009), p. 068102.
- [56] Rajesh Singh and R Adhikari. “Generalized Stokes laws for active colloids and their applications”. In: *Journal of Physics Communications* 2.2 (2018), p. 025025.
- [57] Hartmut Löwen. “Chirality in microswimmer motion: From circle swimmers to active turbulence”. In: *The European Physical Journal Special Topics* 225.11 (2016), pp. 2319–2331.
- [58] Benno Liebchen and Demian Levis. “Collective behavior of chiral active matter: Pattern formation and enhanced flocking”. In: *Physical review letters* 119.5 (2017), p. 058002.
- [59] Demian Levis and Benno Liebchen. “Simultaneous phase separation and pattern formation in chiral active mixtures”. In: *Physical Review E* 100.1 (2019), p. 012406.
- [60] Guo-Jun Liao and Sabine HL Klapp. “Clustering and phase separation of circle swimmers dispersed in a monolayer”. In: *Soft matter* 14.38 (2018), pp. 7873–7882.
- [61] Demian Levis and Benno Liebchen. “Micro-flock patterns and macro-clusters in chiral active Brownian disks”. In: *Journal of Physics: Condensed Matter* 30.8 (2018), p. 084001.
- [62] Jens Bickmann et al. “Analytical approach to chiral active systems: Suppressed phase separation of interacting Brownian circle swimmers”. In: *arXiv preprint arXiv:2010.05262* (2020).
- [63] Qun-Li Lei, Massimo Pica Ciamarra, and Ran Ni. “Nonequilibrium strongly hyperuniform fluids of circle active particles with large local density fluctuations”. In: *Science advances* 5.1 (2019), eaau7423.
- [64] Zhan Ma and Ran Ni. “Dynamical clustering interrupts motility-induced phase separation in chiral active Brownian particles”. In: *The Journal of Chemical Physics* 156.2 (2022), p. 021102.
- [65] Guo-Jun Liao and Sabine HL Klapp. “Emergent vortices and phase separation in systems of chiral active particles with dipolar interactions”. In: *Soft Matter* 17.28 (2021), pp. 6833–6847.
- [66] Benno Liebchen and Demian Levis. “Chiral active matter”. In: *Europhysics Letters* 139.6 (2022), p. 67001.

- [67] Demian Levis, Ignacio Pagonabarraga, and Benno Liebchen. “Activity induced synchronization: Mutual flocking and chiral self-sorting”. In: *Physical Review Research* 1.2 (2019), p. 023026.
- [68] Federico Fadda, John Jairo Molina, and Ryoichi Yamamoto. “Dynamics of a chiral swimmer sedimenting on a flat plate”. In: *Physical Review E* 101.5 (2020), p. 052608.
- [69] PS Burada, R Maity, and Frank Jülicher. “Hydrodynamics of chiral squirmers”. In: *Physical Review E* 105.2 (2022), p. 024603.
- [70] Ruma Maity and PS Burada. “Near and far-field hydrodynamic interaction of two chiral squirmers”. In: *arXiv preprint arXiv:2204.07512* (2022).
- [71] Ruma Maity and PS Burada. “Unsteady chiral swimmer in presence of an external chemical gradient”. In: *arXiv preprint arXiv:2105.15001* (2021).
- [72] Sebastian Rode, Jens Elgeti, and Gerhard Gompper. “Multi-ciliated microswimmers—metachronal coordination and helical swimming”. In: *The European Physical Journal E* 44.6 (2021), pp. 1–14.
- [73] Maciej Lisicki, Shang Yik Reigh, and Eric Lauga. “Autophoretic motion in three dimensions”. In: *Soft Matter* 14.17 (2018), pp. 3304–3314.
- [74] Chong Chen et al. “Weak synchronization and large-scale collective oscillation in dense bacterial suspensions”. In: *Nature* 542.7640 (2017), pp. 210–214.
- [75] Bo Zhang et al. “Oscillatory chiral flows in confined active fluids with obstacles”. In: *Physical Review Research* 2.4 (2020), p. 043225.
- [76] Victor B Putz and Julia M Yeomans. “Hydrodynamic synchronisation of model microswimmers”. In: *Journal of Statistical Physics* 137.5 (2009), pp. 1001–1013.
- [77] Bian Qian et al. “Minimal model for synchronization induced by hydrodynamic interactions”. In: *Physical Review E* 80.6 (2009), p. 061919.
- [78] Nariya Uchida and Ramin Golestanian. “Synchronization and collective dynamics in a carpet of microfluidic rotors”. In: *Physical review letters* 104.17 (2010), p. 178103.
- [79] Jurij Kotar et al. “Hydrodynamic synchronization of colloidal oscillators”. In: *Proceedings of the National Academy of Sciences* 107.17 (2010), pp. 7669–7673.
- [80] Ramin Golestanian, Julia M Yeomans, and Nariya Uchida. “Hydrodynamic synchronization at low Reynolds number”. In: *Soft Matter* 7.7 (2011), pp. 3074–3082.
- [81] Mario Theers and Roland G Winkler. “Synchronization of rigid microrotors by time-dependent hydrodynamic interactions”. In: *Physical Review E* 88.2 (2013), p. 023012.
- [82] Koohee Han et al. “Reconfigurable structure and tunable transport in synchronized active spinner materials”. In: *Science advances* 6.12 (2020), eaaz8535.
- [83] On Shun Pak and Eric Lauga. “Generalized squirming motion of a sphere”. In: *Journal of Engineering Mathematics* 88.1 (2014), pp. 1–28.
- [84] MJ Lighthill. “On the squirming motion of nearly spherical deformable bodies through liquids at very small Reynolds numbers”. In: *Communications on pure and applied mathematics* 5.2 (1952), pp. 109–118.

- [85] John R Blake. “A spherical envelope approach to ciliary propulsion”. In: *Journal of Fluid Mechanics* 46.1 (1971), pp. 199–208.
- [86] Edward M Purcell. “Life at low Reynolds number”. In: *American journal of physics* 45.1 (1977), pp. 3–11.
- [87] Kenta Ishimoto and Michio Yamada. “A coordinate-based proof of the scallop theorem”. In: *SIAM Journal on Applied Mathematics* 72.5 (2012), pp. 1686–1694.
- [88] Eric Lauga. “Life around the scallop theorem”. In: *Soft Matter* 7.7 (2011), pp. 3060–3065.
- [89] Howard A Stone and Aravinthan DT Samuel. “Propulsion of microorganisms by surface distortions”. In: *Physical review letters* 77.19 (1996), p. 4102.
- [90] Wolfram Research Inc. *Mathematica, Version 13.3*. Champaign, IL, 2023. URL: <https://www.wolfram.com/mathematica>.
- [91] Horace Lamb. “Hydrodynamics, § 156”. In: *Aufl., Cambridge: Univ. Press* 1879–1932 427 (1932).
- [92] Michael Kuron et al. “A lattice Boltzmann model for squirmers”. In: *The Journal of chemical physics* 150.14 (2019).
- [93] Juho S. Lintuvuori et al. “Hydrodynamic oscillations and variable swimming speed in squirmers close to repulsive walls”. In: *Soft Matter* 12 (38 2016), pp. 7959–7968.
- [94] Zaiyi Shen, Alois Würger, and Juho S. Lintuvuori. “Hydrodynamic interaction of a self-propelling particle with a wall”. In: *The European Physical Journal E* 41 (39 2018), p. 39.
- [95] Anthony JC Ladd. “Numerical simulations of particulate suspensions via a discretized Boltzmann equation. Part 1. Theoretical foundation”. In: *Journal of fluid mechanics* 271 (1994), pp. 285–309.
- [96] Anthony JC Ladd. “Numerical simulations of particulate suspensions via a discretized Boltzmann equation. Part 2. Numerical results”. In: *Journal of fluid mechanics* 271 (1994), pp. 311–339.
- [97] N-Q Nguyen and AJC Ladd. “Lubrication corrections for lattice-Boltzmann simulations of particle suspensions”. In: *Physical Review E* 66.4 (2002), p. 046708.
- [98] I Llopis and I Pagonabarraga. “Hydrodynamic interactions in squirmer motion: Swimming with a neighbour and close to a wall”. In: *Journal of Non-Newtonian Fluid Mechanics* 165.17-18 (2010), pp. 946–952.
- [99] Ignacio Pagonabarraga and Isaac Llopis. “The structure and rheology of sheared model swimmer suspensions”. In: *Soft Matter* 9.29 (2013), pp. 7174–7184.
- [100] Knut Drescher et al. “Dancing volvox: hydrodynamic bound states of swimming algae”. In: *Physical review letters* 102.16 (2009), p. 168101.
- [101] Amy Henderson Squillacote et al. *The paraview guide*. Vol. 366. Kitware Clifton Park, NY, 2007.
- [102] Aleksandar Donev et al. “Improving the density of jammed disordered packings using ellipsoids”. In: *Science* 303.5660 (2004), pp. 990–993.

- [103] Zongyan Zhou et al. “Discrete modelling of the packing of ellipsoidal particles”. In: *AIP Conference Proceedings*. Vol. 1542. 1. American Institute of Physics, 2013, pp. 357–360.
- [104] Bruno Martinez-Haya and Alejandro Cuetos. “Simulation study of discotic molecules in the vicinity of the isotropic–liquid crystal transition”. In: *Molecular Simulation* 35.12-13 (2009), pp. 1077–1083.
- [105] ShuiXiang Li et al. “Maximum packing densities of basic 3D objects”. In: *Chinese Science Bulletin* 55.2 (2010), pp. 114–119.
- [106] Lufeng Liu et al. “Evolutions of packing properties of perfect cylinders under densification and crystallization”. In: *The Journal of chemical physics* 149.10 (2018), p. 104503.
- [107] Lufeng Liu et al. “Maximally dense random packings of cubes and cuboids via a novel inverse packing method”. In: *Soft matter* 13.4 (2017), pp. 748–757.
- [108] G David Scott and D Marc Kilgour. “The density of random close packing of spheres”. In: *Journal of Physics D: Applied Physics* 2.6 (1969), p. 863.
- [109] James G Berryman. “Random close packing of hard spheres and disks”. In: *Physical Review A* 27.2 (1983), p. 1053.
- [110] Salvatore Torquato, Thomas M Truskett, and Pablo G Debenedetti. “Is random close packing of spheres well defined?” In: *Physical review letters* 84.10 (2000), p. 2064.
- [111] Cosimo Livi et al. “Influence of numerical resolution on the dynamics of finite-size particles with the lattice Boltzmann method”. In: *Physical Review E* 103.1 (2021), p. 013303.
- [112] Akash Choudhary et al. “How inertial lift affects the dynamics of a microswimmer in Poiseuille flow”. In: *Communications Physics* 5.1 (2022), p. 14.
- [113] Bo Zhang, Andrey Sokolov, and Alexey Snezhko. “Reconfigurable emergent patterns in active chiral fluids”. In: *Nature communications* 11.1 (2020), pp. 1–9.
- [114] Antoine Bricard et al. “Emergence of macroscopic directed motion in populations of motile colloids”. In: *Nature* 503.7474 (2013), pp. 95–98.
- [115] Takuji Ishikawa et al. “Stability of dancing Volvox”. In: *Journal of Fluid Mechanics* 903 (2020), A11.
- [116] Colin S Reynolds. *The ecology of phytoplankton*. Cambridge University Press, 2006.
- [117] L Legendre. “Hydrodynamic control of marine phytoplankton production: the paradox of stability”. In: *Elsevier oceanography series*. Vol. 32. Elsevier, 1981, pp. 191–207.
- [118] Michael J Behrenfeld and Emmanuel S Boss. “Resurrecting the ecological underpinnings of ocean plankton blooms”. In: *Annual review of marine science* 6 (2014), pp. 167–194.